List of attached articles
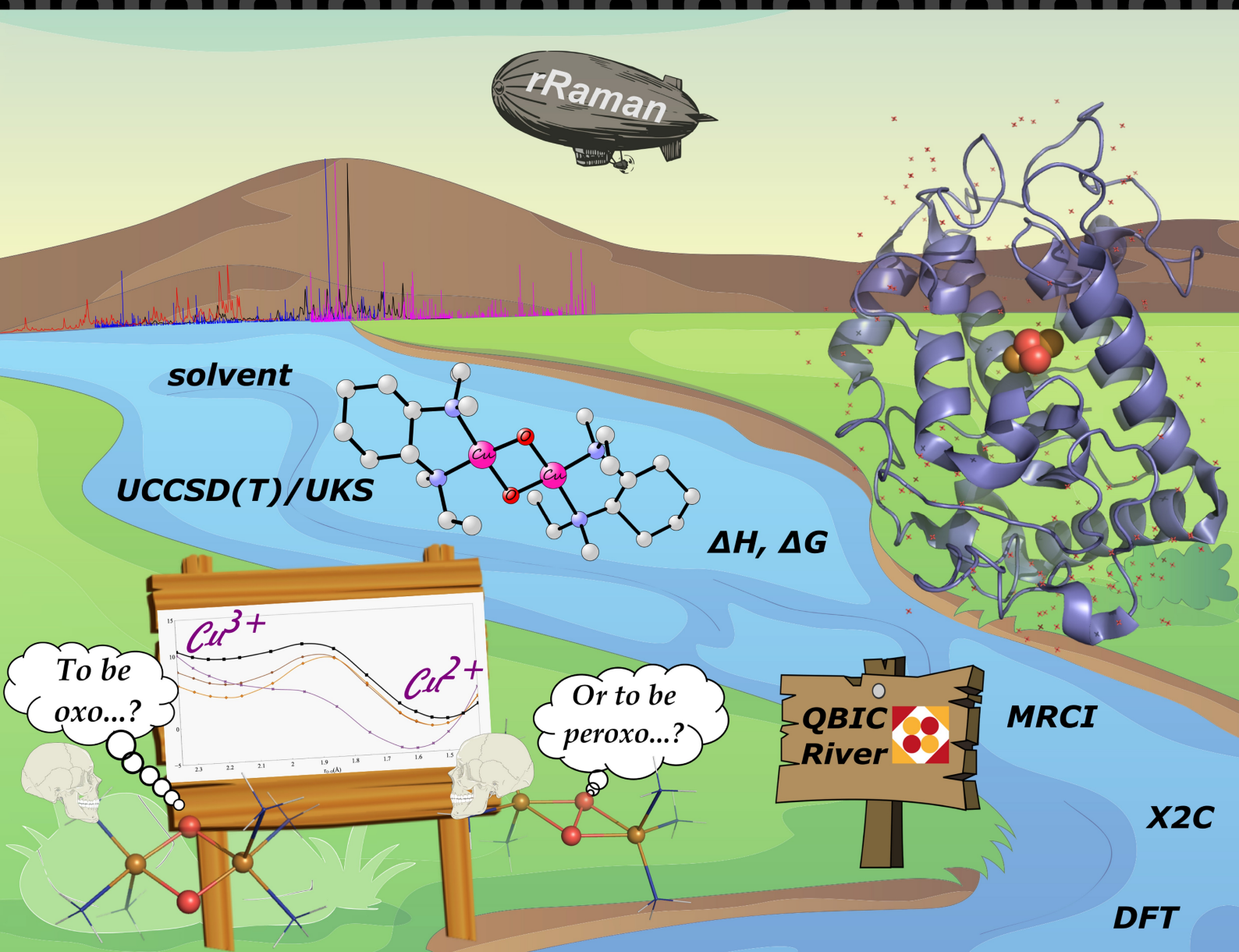
1. **Paper I**: Comprehensive Theoretical View of the [Cu$_2$O$_2$] Side-on-Peroxo-/Bis-μ-Oxo Equilibria
   Authors: **Agnieszka Stańczak**, Jakub Chalupský, Lubomír Rulíšek, Michal Straka
   Published in the ChemPhysChem
   Cover article

2. **Paper II**: Evidence for H-bonding interactions to the μ-η^2:η^2-peroxide of oxy-tyrosinase that activate its coupled binuclear copper site
   Authors: ‡Ioannis Kipouros, ‡**Agnieszka Stańczak**, Martin Culka, Erik Andris, Timothy R. Machonkin, Lubomír Rulíšek, Edward I. Solomon
   Published in the Chemical Communication

3. **Paper III**: Elucidation of the tyrosinase/O$_2$/monophenol ternary intermediate that dictates the monooxygenation mechanism in melanin biosynthesis
   Authors: Ioannis Kipouros, **Agnieszka Stańczak**, Jake W. Ginsbach, Prokopis C. Andrikopoulos, Lubomír Rulíšek, Edward I. Solomon
   Published in the Proceedings of the National Academy of Sciences of the United States of America

4. **Paper IV**: Experimental Evidence and Mechanistic Description of the Phenolic H-Transfer to the Cu$_2$O$_2$ Active Site of oxy-Tyrosinase
   Authors: ‡Ioannis Kipouros, ‡**Agnieszka Stańczak**, Eleanor M. Dunietz, Jake W. Ginsbach, Martin Srnec, Lubomír Rulíšek, Edward I. Solomon
   Published in the Journal of the American Chemical Society

   ‡ These authors contributed equally.

Paper I:
Comprehensive Theoretical View of the $[\mathrm{Cu_2O_2}]$
Side-on-Peroxo-/Bis-μ-Oxo Equilibria

ChemPhysChem

Cover Feature:
Agnieszka Stańczak, Jakub Chalupský, Lubomír Rulíšek, and Michal Straka
Comprehensive Theoretical View of the [Cu$_2$O$_2$] Side-on-Peroxo-/Bis-μ-Oxo Equilibria

Comprehensive Theoretical View of the [Cu₂O₂]
Side-on-Peroxo-/Bis-*μ*-Oxo Equilibria

Agnieszka Stańczak,[a, b] Jakub Chalupský,*[a] Lubomír Rulíšek,*[a] and Michal Straka*[a]

Coupled binuclear copper (CBC) sites are employed by many metalloenzymes to catalyze a broad set of biochemical transformations. Typically, the CBC catalytic sites are activated by the O_2 molecule to form various [Cu₂O₂] reactive species. This has also inspired synthesis and development of various biomimetic inorganic complexes featuring the CBC core. From theoretical perspective, the [Cu₂O₂] reactivity often hinges on the side-on-peroxo-dicopper(II) (**P**) vs. bis-*μ*-oxo-dicopper(III) (**O**) isomerism - an equilibrium that has become almost iconic in theoretical bioinorganic chemistry. Herein, we present a comprehensive calibration and evaluation of the performance of various composite computational protocols available in contemporary computational chemistry, involving coupled-cluster and multi-

reference (relativistic) wave function methods, popular density functionals and solvation models. Starting with the well-studied reference [Cu₂O₂(NH₃)₆]²⁺ system, we compared the performance of electronic structure methods and discussed the relativistic effects. This allowed us to select several 'calibrated' DFT functionals that can be conveniently employed to study ten experimentally well-characterized [Cu₂O₂] inorganic systems. We mostly predicted the lowest-energy structures (**P** vs. **O**) of the studied systems correctly. In addition, we present calibration of the used electronic structure methods for prediction of the spectroscopic features of the [Cu₂O₂] core, mostly provided by the resonance Raman (rR) spectroscopy.

Introduction

Dicopper enzymes catalyze a broad set of chemical reactions, mostly using O_2 as a cofactor.[1] The particular course of these reactions, i.e., the enzyme specificity, often hinges on fine-tuned structural details of the enzyme active site.[1–2] This can be exemplified by tyrosinase (Ty) and catechol oxidase, two enzymes with almost identical CBC active sites, each of them catalyzing different transformations.[1,3] While both enzymes can accept catechols and convert them to the quinones, only tyrosinase can catalyze monohydroxylation of phenols.[4–7] Still, a single mutation of a (seemingly less important) second-sphere residue of the catechol oxidase can lead to observing a small monohydroxylation activity of the enzyme.[8] To understand such (and many other) experimental observations and explore mechanistic details of the catalytic cycle of dicopper enzymes, computational chemistry is used as the complementary tool providing structure/energy correlations.[1,9–10] The direct comparison between calculated and experimental data on the CBC enzymes is not trivial, mostly because of a great number of unknown structural details, effect of the protein bulk, etc. Such

comparison is more straightforward on smaller, structurally well-characterized inorganic Cu₂O₂ complexes, quite often mimicking active sites of their enzymatic counterparts.[11–16] Over the last two decades, more than a dozen of such complexes have been synthesized and studied for their reactivity towards various di-copper enzyme's substrates and their analogues.[2,9,11–34]

Both experiments and computations have identified the side-on-peroxo-dicopper(II) (**P**) *vs.* bis-*μ*-oxo-dicopper(III) (**O**) equilibrium as one of the key issues that governs the (bio)inorganic Cu₂/O₂ reactivity. Notably, the structurally trivial **P**↔**O** equilibrium became one of the major challenges for quantum chemical methods, as it seems to encompass all problems that the wave function and DFT methods are facing: static and dynamical correlation, relativistic effects, and solvent effects. The accurate theoretical treatment is often too costly for multireference wave-function (WFT) methods, especially in case of enzymatic model systems of a realistic size. Because of that, multireference methods were used only for very small models, comprising the Cu₂O₂ core and few first-sphere coordinating atoms.[35–42] For bigger systems, be it synthetic complexes or enzyme active sites, calculations have been mostly limited to density functional theory (DFT) methods.[10,43–48]

In this work, we revisit the problem and utilize the broad set of Cu₂O₂ inorganic models,[9,13–15,28–29,31–34,47] synthesized and characterized up to date with well-defined structures, in particular those with clearly identified "ground state" (lowest-energy) geometry (**P/O**). This greatly extends previous studies carried out for limited sets of compounds and/or for only a limited set of properties.[35,37–39,41] We thus aim to present a comprehensive calibration work, concerning not only the energetics of the **P**↔**O** equilibrium, but also calculations of

[a] A. Stańczak, J. Chalupský, L. Rulíšek, M. Straka
Institute of Organic Chemistry and Biochemistry of the Czech Academy of Sciences, Flemingovo náměstí 2, 166 10, Praha 6, Czech Republic
E-mail: chalupsky@uochb.cas.cz
rulisek@uochb.cas.cz
straka@uochb.cas.cz

[b] A. Stańczak
Faculty of Science, Charles University, Albertov 2038/6, Prague 2, 128 43, Czech Republic

ChemPhysChem

Research Article
doi.org/10.1002/cphc.202200076

Chemistry
Europe
European Chemical
Societies Publishing

vibrational frequencies that can be compared with their experimental counterparts, obtained mostly by the resonance Raman technique.

Systems studied in this work are depicted in Figure 1. These include following ligands: hydrotris(3,5-diisopropyl-pyrazolyl)borate (**1**),[14–15] N,N'-diethyl-N,N'-dimethyl-cyclohexa-nediamine (**2**),[29] N,N,N',N'-tetraethylethylenediamine (**3**),[29] complex of N, N'-di-tert-butyl N,N'-1,2-ethanediamine with 2,4-di-tert-butylphenolate bound to copper (**4**),[9] N, N'-di-tert-butyl N,N'-dimethyl-1,2-ethanediamine (**5**),[31] N, N'-di-tert-butyl N,N'-1,2-ethanediamine (**6**),[31,47] N-[2-(4-methoxy-pyridin-2-yl)-ethyl]-N,N',N'-trimethyl-propane-1,3-diamine (**7**),[28] 1,4,7-triisopropyl-
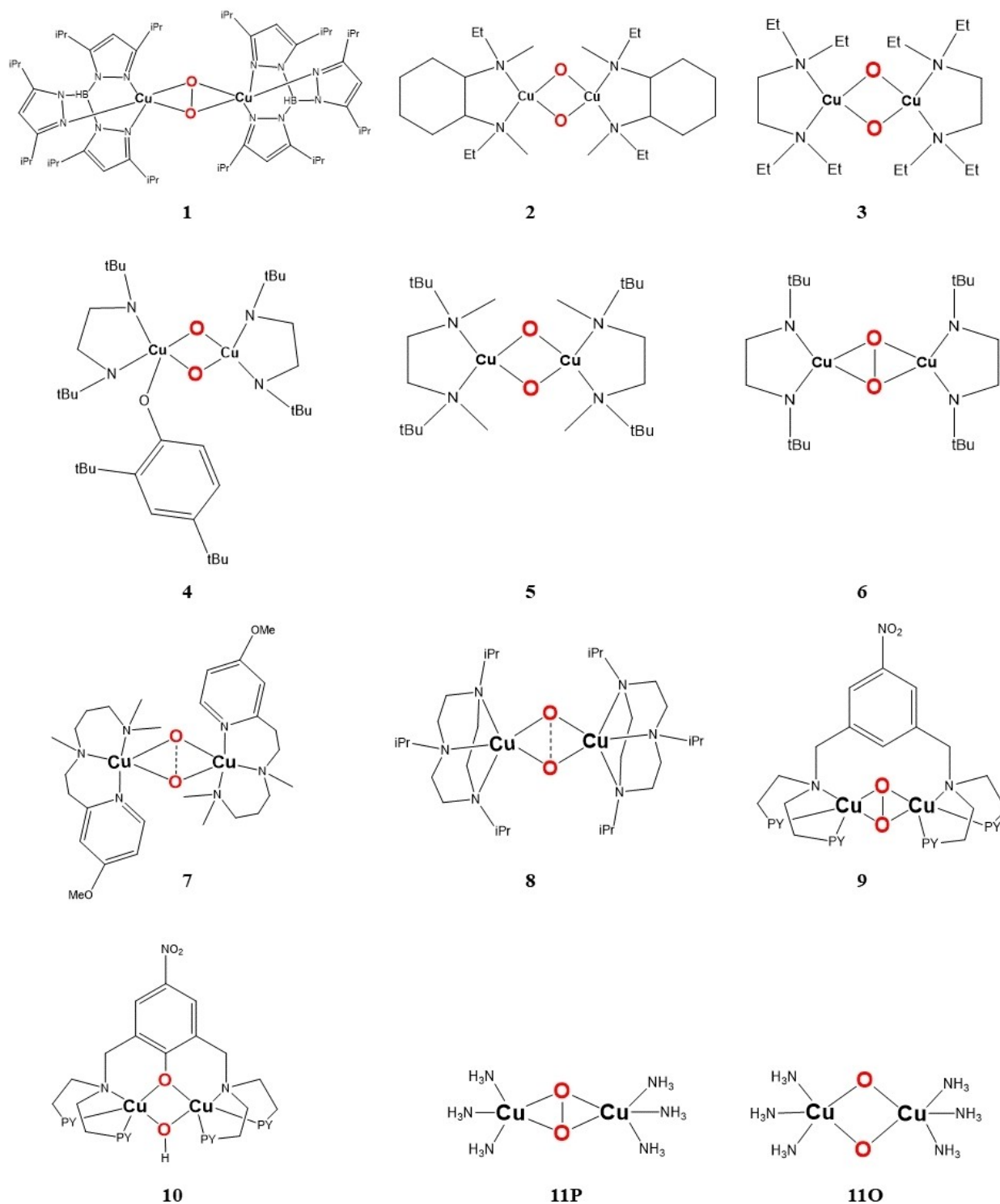

Figure 1. Biomimetic compounds **1–10** and model system **11** (both **P** and **O** forms of **11** are shown) studied in this work. Systems **1–10** are shown in their presumable lowest-energy (**P/O**) isomer form, except the solvent-dependent systems (**7** and **8**), for which both isomers may exist.

1,4,7-triazacyclononane **(8)**,[32] N,N′-((5-nitro-1,3-phenylene)bis(methylene))bis(2-(pyridin-2-yl)-N-(2-(pyridin-2-yl)ethyl)ethan-1-amine) **(9)**,[33–34] and its hydroxylated product **(10)**.[13,34]

For compounds **2,3,4** and **5**, the experimental equilibrium geometry should correspond to the bis-μ-oxo-(**O**) while **1**, **4**, and **9** adopt peroxo- (**P**) structural (and electronic) arrangement. Equilibrium geometries of systems **7** and **8** are solvent-dependent. System **10** is a hydroxylated product, and we use it only for calibration of frequencies and interatomic distances. We also include the model system **11** (Figure 1) that is the $[Cu_2O_2(NH_3)_6]^{2+}$ complex. It does not have an experimental counterpart but has been repeatedly studied previously by employing correlated multireference calculations (in addition to DFT). It represents the convenient starting point for calculations of larger systems. To provide computed data of the "reference quality" we attempt to include all physical and methodological details into calculations. In particular, we include scalar relativistic effects, solvent effects, ZPVE, enthalpic and entropic contributions, and we assure convergence of the basis sets while employing different DFT functionals. The answers to following questions are sought: (1) Are we able to (always) reproduce the experimental results in the case of the **P/O** equilibrium? (2) Are we able to obtain Cu_2O_2 vibrational modes in agreement with experimental values? (3) What is the role and magnitude of various physical contributions used to reproduce the experiment properly?

To achieve these goals, we first discuss various computational approaches employed in this work and link them to previous works of others. Next, we reinvestigate the previously studied model system **11** and present an exhaustive DFT and wave function treatment of its **P/O** equilibrium to correlate our work with previous $[Cu_2O_2]$ studies.[10,35–42,47–48] Finally, we focus on systems **1–10** where we investigate the role of the ligand environment of the $[Cu_2O_2]$ core, used DFT functional, and analyze effects of solvation. At the same time, we compare computed vibrational frequencies and equilibrium geometries with their experimental counterparts. In conclusion, we attempt to outline comprehensive computational guidelines for theoretical studies of the $[Cu_2O_2]$ systems, including di-copper metalloenzymes.[36]

Computational Methods

Molecular Structures

The initial coordinates of **1–10** were obtained from the literature.[9,13–15,28–29,31–34,47] All structures were then re-optimized employing density functional theory. Specifically, we used the TURBOMOLE 7.4 program[49] employing the one-component (scalar) relativistic X2C[50] approximation, the TPSS[51–54] density functional, x2c-TZVPall[55] basis set and the D3BJ dispersion correction,[56] wherever possible (*vide infra*). These calculations used implicit solvent that was modeled with conductor-like screening model (COSMO[57]) as implemented in TURBOMOLE 7.4. For each **O** isomer, the singlet state was considered whereas for the **P** isomers, both singlet and triplet electronic states were calculated. The singlet state was calculated using the broken-symmetry approach.[58–59] All

equilibrium structures were characterized as genuine minima with no imaginary frequencies. These initial structures were then re-optimized at requested computational levels (*vide infra*). The preparation of **11O** and **11P** structures and of the interconnecting reaction is described below (Section 3.1).

DFT Calculations and Choice of the Functionals

To evaluate the performance of various DFT functionals, the TPSS equilibrium geometries of **1–10** were further re-optimized using x2c-TZVPall[55] basis set, relativistic X2C[50] approximation and a given density functional. We have chosen the PBE,[51–53,60] BP86,[51,53,61–63] B97D,[64] TPSSh,[51–54,65] B3LYP,[51,53,61,63,66–67] M06,[68] CAM-B3LYP,[69] and LH14t-calPBE[70] functionals to represent the broad spectrum of DFT functionals with varying degree of exact exchange and other physical ingredients. The BP86, B97D, and PBE represent the pure GGA functionals, the TPSS a pure meta-GGA functional. The hybrid functionals are represented by TPSSh, B3LYP, and M06 with 10%, 20%, and 27% of the exact exchange admixture, range-separated hybrid functionals are represented by CAM-B3LYP, and local hybrid functional by the Lh14t-calPBE.

Unless mentioned otherwise, the structure optimizations were done using the polarized continuum model (COSMO) as implemented in Turbomole 7.4., with the same solvent as in the corresponding experiments. The experiments were done in CH_2Cl_2, THF, MeTHF, DMF, and acetone solvents with $\varepsilon_r = 8.93$, 7.43, 6.97, 37.22,[71] and 20.49 respectively.

Most DFT calculations were performed using the Grimme's dispersion correction (D3BJ).[56] Exceptions were CAM-B3LYP, M06, and Lh14t-calPBE functionals.

X2C-UCCSD(T)/UKS Calculations

Our initial canonical CCSD(T) calculations employing the unrestricted Hartree-Fock (UHF) wave functions provided results of inferior quality (*data not shown*). One of the reasons was a spin contamination of the UHF reference wave function that also led to large D_1 diagnostics. Inspired by similar studies[72–74] we carried out UCCSD(T) calculations using non-canonical TPSS Kohn-Sham orbitals as the reference wave function. Relativistic effects were incorporated via the X2C approximation. TURBOMOLE 7.4 code was used. In all CCSD(T) calculations, a small number of core orbitals were frozen (1s, 2s, 2p on Cu, and 1s on O, C, and N, i.e. 18 in total).

Relativistic Approximations and Basis Sets

Most of the DFT calculations were performed employing the one-component (scalar) relativistic X2C approximation. For these, the relativistic x2c-SVPall, x2c-TZVPall, x2c-TZVPPall, x2c-QZVPall[55] as implemented in the Turbomole 7.4. were used, whereas the comparative non-relativistic DFT calculations employed Ahlrichs' def2-SVP, def2-TZVP, def2-TZVPP, and def2-QZVP[75] basis sets. The importance of relativistic effects and basis set convergence were tested on two variants of model system **11**, see Figures S1–S2 and Tables S1–S2 in SI. The default basis set in single-reference DFT calculations was x2c-TZVPall using the X2C approximation, unless stated otherwise. On a model system, we ascertained the expected finding that spin-orbit coupling effects play negligible role in the **P/O** equilibrium.

Multireference Calculations

In addition to DFT calculations, the multiconfiguration pair-density functional (MC-PDFT)[76] calculations were done using various functionals.[77] The active space of the reference complete active space self-consistent field method (CASSCF)[78–79] comprised of the six in-plane orbitals, which are essential for the isomerization. These are two $3d$ Cu orbitals and four $2p$ O orbitals oriented toward Cu—O/O—O bonds, forming CASSCF(8,6) active space, see Figure S3 for details.

For systems **1**–**10** the single-point energies were calculated using the same CASSCF(8,6) active space and various MC-PDFT functionals. Multireference configuration interaction (MRCI)[80] energy was calculated for the smallest complex **11**. All multireference calculations employed ANO-RCC[81–83] basis sets (ANO-RCC-VDZP or -VTZP for H and ANO-RCC-VTZP for other atoms). Scalar relativistic effects were included via the DKH2 (2nd-order Douglas-Kroll-Hess) spin-less Hamiltonian.[84–86] MC-PDFT and MRCI calculations were performed with the Molcas 8.4[87] and Molpro 2015.1[88] programs, respectively.

Thermochemistry and Solvation

Thermochemical analysis was performed using Grimme's *thermo*[89] program which is essentially the rigid-rotor/harmonic oscillator (RRHO) approximation in which a free rotor (FR) model is applied for low-lying vibrational modes under 100 cm^{-1} with a smoothing function between the FR and RR regimes. This is sometimes denoted as quasi-RRHO or RRFRHO approximation. The experimental temperatures described in corresponding publications were used in calculations. Due to the lack of implementation of analytical frequencies, the hessians for the B97D, CAM-B3LYP, and LH14t-calPBE were calculated numerically; other functionals afforded analytical frequencies.

Solvation energies (ΔG_{solv}) were obtained using Klamt's conductor-like screening model for realistic solvation (COSMO-RS). The COSMO-RS calculations were carried out using *cosmotherm19*[90] software and the recommended protocol: BP86-D3(BJ)/def2-TZVPD single point calculations *in vacuo* and in ideal conductor ($e = \infty$) followed by the COSMO-RS calculations in the target solvent. The "BP_TZVPD_FINE_19.ctd" parametrization file, FINE cavities (\$cosmo_isorad keyword) were used. Final free energies of isomers in solvent were based on the following formula:

$$G_S = E_{el} + \Delta G_{solv} + E_{ZPVE} - RT\ln(q_{trans}q_{rot}q_{vib}) + pV \quad (1)$$

where G_S is the free energy in solvent, E_{el} is the electronic energy of the molecule *in vacuo*, calculated at the geometry optimized in CPCM (COSMO) implicit solvation model, the ΔG_{solv} is then the presumably more accurate COSMO-RS solvation energy. The E_{ZPVE} is the zero-point vibrational energy whereas $RT\ln(q_{trans}q_{rot}q_{vib})$ are the entropic terms obtained from the quasi-harmonic RRFRHO approximation.[89] Where needed, gas-phase enthalpy H_{gp} of the system is defined (trivially) as

$$H_{gp} = E_{el} + E_{ZPVE} \quad (2)$$

keeping in mind that $pV (= RT)$ is constant as there is no change in the number of particles in the studied equilibria.

Occasionally, we may employ the (free) energy of the molecule in solvent, denoted E_{CPCM}, which is the sum of electronic energy and COSMO solvation energy, standardly printed out by the quantum chemistry software.

Vibrational Analysis of Cu$_2$O$_2$ and C-O Modes

The vibrational analysis was performed with all atoms frozen, except for the Cu$_2$O$_2$ core (and C bound to oxygen Cu$_2$O$_2$ oxygen in **10**). The freezing was performed by zeroing all elements of the vibrational Hessian containing the frozen atoms prior to its diagonalization. The Cu$_2$O$_2$ vibrational modes were projected from the coupled normal modes.[91]

Results and Discussion

[Cu$_2$O$_2$(NH$_3$)$_6$]$^{2+}$ Model System (compound 11): Performance of Electronic Structure Methods

To connect this work with previous studies,[35–37,92–93] we first reinvestigated model system **11** (i.e., the [Cu$_2$O$_2$(NH$_3$)$_6$]$^{2+}$ complex; c.f. Figure 1). Despite its simplicity, the accurate quantum chemical description of the **11O**↔**11P** equilibrium seems to be quite challenging. This is due to necessity to include both static and dynamic correlation, and relativistic effects.[35,92,94] A rather small **P/O** energy difference and low conversion barrier between the two isomers make this problem even more complicated. It is, though, an ideal system for investigating various physical effects and computational subtleties. A model has been presented in the literature[35] along with an approximate 'reaction coordinate' connecting the **11O** and **11P** minima. Interpolated intermediate geometries are characterized by the ratio F (0–100%) where $F = 0$ corresponds to the **11O** and $F = 100$% corresponds to the **11P** minimum, respectively. The intermediate structures (20%, …, 80%) are simple linear interpolations in Cartesian coordinates. Selected results of previous studies on this model system, aligned with 'our model chemistries' that are used later in this work, are compiled and discussed in the SI, Figure S1 and Table S1. It must be noted, though, that a direct comparison with the former results is not straightforward. Different studies used slightly different basis sets and relativistic approximations, for example, ECPs[35,93] that was later shown to introduce additional errors.[36,38–39] In addition, the interpolated coordinate without further geometry optimization may lead to additional (small) errors.

Hence, we introduce a new reaction coordinate for the **11O**↔**11P** equilibrium. Instead of linear geometric interpolation between the **11O** and **11P** minima, the reaction coordinate is defined by the relaxed scan of the O—O distance (Figure 2, Table 1 and S2), computed at the X2C-TPSS/x2c-TZVPall level. The relaxed scan is done in steps of 0.05 Å around both minima (**11O** and **11P**) and the transition state, and 0.1 Å for the remaining parts of the coordinate (c.f. Figure 2). Selected and representative energy profiles computed at various levels of theory (incl. non-relativistic calculations) are depicted in Figures 2 and 3 whereas the full set of computed data (including variety of MC-PDFT functionals) are compiled in Tables 1 and S2. Moreover, in Figure S2, we illustrate the role of the relativistic effects and basis set convergence on the new reaction coordinate.

Before discussing the computed data depicted in Figure 2, we note that in contrast to our attempts to carry out the
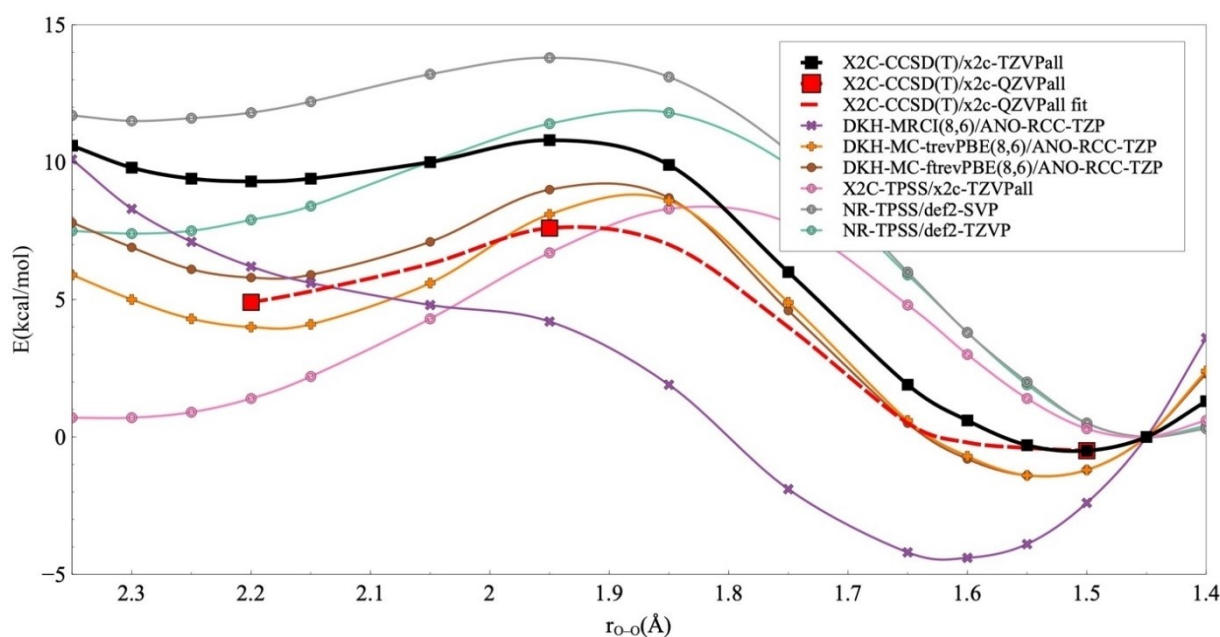
ChemPhysChem

Research Article
doi.org/10.1002/cphc.202200076

Chemistry
Europe
European Chemical
Societies Publishing

Figure 2. Comparison of selected computational levels for the simulated **11O↔11P** reaction coordinate (see also Table 1). Single-point calculations *in vacuo* at 0 K without ZPVE correction using X2C-TPSS/x2c-TZVPall coordinates with fixed r_{O-O} distance and optimized rest of the molecule. MR calculations used ANO-RSC-VTZP basis set on Cu, O, N and ANO-RSC-DZVP on H, see Methods.

Table 1. .Comparison of selected levels of theory[a] for the new **11O↔11P** isomerization coordinate obtained by scanning the r_{o-o} at the X2C-TPSS/x2c-TZVPall level. All values are in kcal.mol^{-1}.

r_{O-O}	2.35	2.3	2.25	2.2	2.15	2.05	1.95	1.85	1.75	1.65	1.6	1.55	1.5	1.45	1.4
X2C-CCSD(T)/TZ	10.6	9.8	9.4	9.3	9.4	10.0	10.8	9.9	6.0	1.9	0.6	−0.3	−0.5	0.0	1.3
X2C-CCSD(T)/QZ[b]			5.4				8.1						0.0		
X2C multireference															
CASSCF(8,6)	24.0	22.2	20.7	19.3	17.9	15.0	10.7	3.9	−3.2	−6.6	−6.5	−5.5	−3.1	0.0	4.3
MRCI	14.9	13.0	11.7	10.6	9.6	8.0	6.1	2.3	−2.3	−4.8	−4.9	−4.2	−2.5	0.0	3.7
MRCI+Q (fixed)	9.7	8.0	6.8	5.9	5.3	4.6	4.0	1.8	−1.9	−4.2	−4.4	−3.9	−2.4	0.0	3.5
MRCI+Q (relax)	10.1	8.3	7.1	6.2	5.6	4.8	4.2	1.9	−1.9	−4.2	−4.4	−3.9	−2.4	0.0	3.6
MC-tBLYP	2.6	1.6	1.0	0.8	1.0	2.6	5.3	6.1	2.7	−1.0	−2.0	−2.2	−1.6	0.0	2.7
MC-tPBE	3.2	2.2	1.5	1.3	1.5	3.3	6.3	7.5	4.4	0.7	−0.6	−1.3	−1.1	0.0	2.3
MC-tLSDA	−3.0	−4.2	−4.9	−5.0	−4.6	−2.1	2.4	5.7	4.9	2.3	0.9	−0.1	−0.5	0.0	1.6
MC-trevPBE	5.9	5.0	4.3	4.0	4.1	5.6	8.1	8.6	4.9	0.6	−0.7	−1.4	−1.2	0.0	2.4
MC-tOPBE	12.7	11.6	10.6	9.9	9.7	10.5	12.5	12.5	8.4	3.5	1.6	0.2	−0.4	0.0	1.6
MC-ftPBE	4.8	3.8	3.1	2.9	3.0	4.6	7.1	7.7	4.4	0.7	−0.6	−1.2	−1.1	0.0	2.2
MC-ftBLYP	4.0	3.1	2.4	2.2	2.4	3.9	6.2	6.5	2.9	−0.8	−1.8	−2.1	−1.5	0.0	2.6
MC-ftLSDA	−3.2	−4.4	−5.0	−5.1	−4.7	−2.0	2.6	6.1	5.5	2.8	1.4	0.2	−0.4	0.0	1.4
MC-ftrevPBE	7.8	6.9	6.1	5.8	5.9	7.1	9.0	8.7	4.6	0.5	−0.8	−1.4	−1.2	0.0	2.3
MC-ftOPBE	14.3	13.1	12.1	11.4	11.2	11.8	13.2	12.6	8.3	3.5	1.6	0.3	−0.4	0.0	1.5
X2C DFT															
PBE	3.5	3.5	3.8	4.3	5.1	7.1	9.3	10.6	9.7	6.2	4.1	2.2	0.7	0	0.2
BP86	4	4	4.2	4.7	5.5	7.5	9.6	10.8	9.7	6.1	4	2.1	0.6	0	0.2
B97D	11.6	11.5	11.5	11.7	12.2	13.4	14.6	14.6	12.1	7.5	5	2.8	0.9	0	−0.1
TPSS	0.7	0.7	0.9	1.4	2.2	4.3	6.7	8.3	7.8	4.8	3	1.4	0.3	0	0.6
TPSSH	2.7	2.6	2.7	3.3	4.1	6.4	9	10.9	10.3	6.8	4.6	2.5	0.8	0	0
B3LYP	7.2	7.1	7.3	7.8	8.6	11	13.5	15	13.6	9	6.2	3.7	1.4	0	−0.6
M06	8.8	8.5	8.8	9.3	10.2	12.9	15.8	17.9	16.7	11.8	8.6	5.4	2.2	0	−1.4
LH14t-calPBE	7.9	7.8	7.9	8.4	9.2	11.6	14.2	15.9	14.6	9.9	7	4.2	1.6	0	−0.8
CAM-B3LYP	6.8	6.5	6.6	7.1	7.9	10.5	13.7	16.2	15.8	11.4	8.3	5.1	2.1	0	−1.3
PBE0	7.7	7.5	7.7	8.2	9.1	11.6	14.5	16.5	15.6	10.9	7.8	4.8	1.9	0	−1.1
WB97XD	7.3	7	7.1	7.6	8.5	11	14.3	16.8	16.3	11.8	8.6	5.4	2.2	0	−1.4

[a] X2C relativity and x2c-TZVall basis set are used in single reference calculations, unless mentioned otherwise. ANO-RCC-TZP on Cu, N, O and ANO-RCC-DZP on H was used, together with DKH approximation, in multireference calculations, see Methods. [b] x2c-QZVPall on Cu, N, O and x2c-TZVPall on H was used.
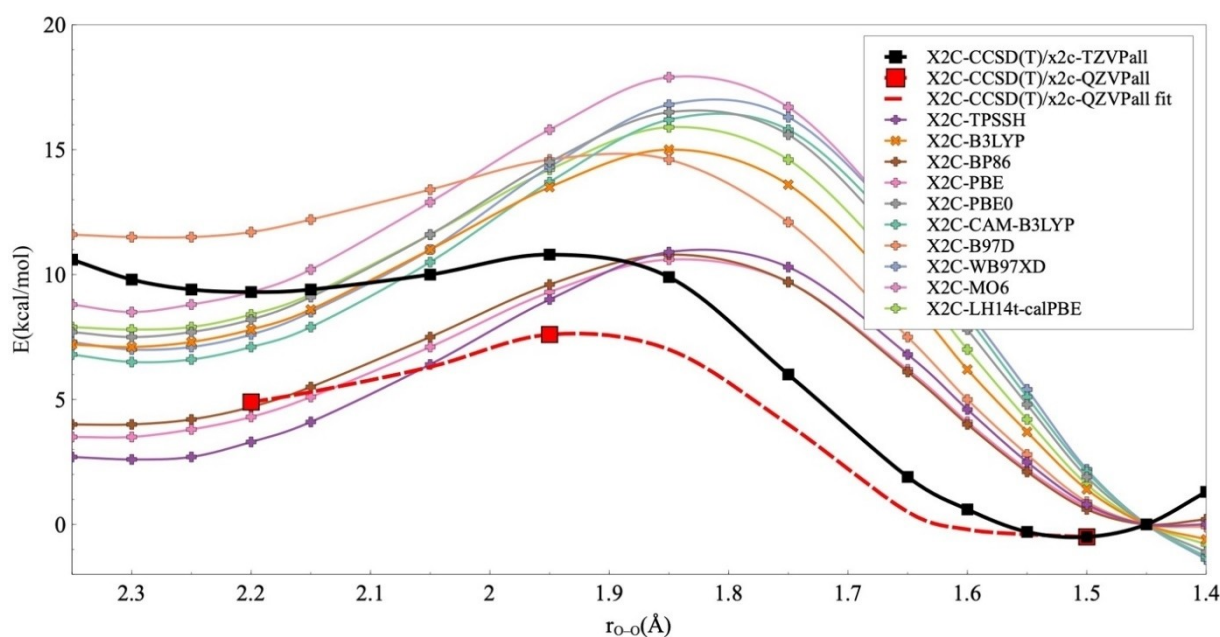
ChemPhysChem

Research Article
doi.org/10.1002/cphc.202200076

Chemistry
Europe
European Chemical
Societies Publishing

Figure 3. Comparison of various DFT functionals for the for the new **11O↔11P** isomerization coordinate obtained by scanning the $r_{o\text{-}o}$ at the X2C-TPSS/x2c-TZVPall level. Single-molecule *in vacuo* at 0 K without ZPVE correction. X2C relativity with x2c-TZVPall basis set used unless otherwise mentioned.

standard UCCSD(T)/UHF calculations which provided rather unsatisfactory results due to high spin contamination of the initial UHF wave function (*data not shown*), the UCCSD(T)/UKS seemed to provide quite consistent data. To our surprise, the D_1 characteristic for the 'broken symmetry' low-spin $M_S = 0$ Kohn-Sham determinant of the **11P** structure is 'only' 0.08. The same value was obtained for the **11O** which was rather expected (the complete list of D_1 diagnostics are summarized in Tables S3–S4). This suggests that the UCCSD(T)/UKS data can be considered as an interesting alternative to MR-WFT methods. This is quite in line with similar observations made for the heme systems by Radon and Pierloot.[95–98] Because of the acceptable CC characteristics and a good agreement with previous CR-CCSD(T)$_L$ calculations of Cramer *et al*[35] (Figure S1), we tend to consider the presented X2C-UCCSD(T)/UKS/x2c-QZVPall(TZVP on H) calculations as the most solid benchmark for the Cu_2O_2 equilibrium up to date. In particular, we conclude that the energy difference between the **11O** and **11P** isomers is $\Delta E_{UCCSD(T)//UKS} = 5$–6 kcal.mol^{-1}, in favor of the **11P** and the transition is accompanied by the 'activation energy' of approximately 8 kcal.mol^{-1}. The $\Delta E_{UCCSD(T)//UKS}$ gives **11P** minimum around 1.5 Å, by 1.3 kcal.mol^{-1} lower in energy than the typical geometry with the $r_{o\text{-}o} = 1.4$ Å of the experimental peroxo- systems shown in Figure 1.

Concerning the presented multireference wave function theory calculations, it has previously been shown that a large CAS active space is needed to properly describe the studied systems and probably the best previous results have been obtained using CASPT2(24,28), c.f. Figure S1. From our computed data, it seems that the MRCI calculations employing (8,6) active space (Figure 2; for corresponding orbitals, see Figure S3) highlight the problem of too small active space. We can see

that MRCI(8-in-6) calculations overestimate the **P/O** energy difference and do not predict any barrier between the **P** and **O** minima. This result is similar to the previous MRCI calculations using the 'original model/coordinate' of the **11O/11P** equilibrium. Therein, the barrier from the oxo- side was found be almost negligible, for details, see Figure S1 and Ref.[93] Unfortunately, MR-CI calculations with larger active spaces are still beyond the practical limits of contemporary quantum chemistry.

What is encouraging, though, is that some of the MC-PDFT calculations, summarized in Table 1, notably the MC-trevPBE and MC-ftrevPBE (Figure 2) show rather good agreement with the benchmark UCCSD(T)/UKS calculations. Overall, the MC-PDFT gives generally satisfactory results, except for the LDA functionals that predict the **O** isomer to be more stable than the **P** one (Table 1). In Figure 2, we also wanted to illustrate the role of the scalar relativistic effects, discussed previously, and the role of the basis-set size, both in the X2C and non-relativistic calculations. This is quite important, since the NR-TPSS/def2-TZVP is often used in studies of Cu_2O_2 systems. We may conclude that NR-TPSS/def2-TZVP performs quite well on the model system **11** owing to the error cancellation. In fact, more rigorous, relativistic X2C-TPSS/x2c-TZVPall calculations seem to perform worse, yielding too low **P/O** energy difference. On the other hand, smaller basis set (NR-TPSS/def2-SVP level) leads to too high stability of the **P**. For a detailed comparison of various basis sets at NR and relativistic X2C level on the new reaction coordinate for the **11O↔11P** equilibrium, see Figure S2.

In Figure 3, we summarize in the graphical form the bottom part of the Table 1 and compare the UCCSD(T)/UKS results with the variety of DFT functionals. It can be seen that the overall

ChemPhysChem

Research Article
doi.org/10.1002/cphc.202200076

**Chemistry
Europe**
European Chemical
Societies Publishing

performance of DFT methods is rather satisfactory, and none of the computed DFT results should be considered as unacceptably wrong. In general, they tend to overestimate the activation energy (typically by 5–10 kcal.mol^{-1} with respect to the UCCSD(T)/QZ benchmark), whereas *ca* half of them correctly predicts the thermodynamics of the **P/O** equilibrium (6–8 kcal.mol^{-1}). Rather surprising, perhaps fortuitous, seems to be the performance of the PBE and BP86 functionals which slightly overstabilize the **O** structure, but provide quite accurate barriers along the reaction coordinate.

Synthetic Complexes

After the in-depth analysis of the performance of quantum chemical methods for the CBC model system (presented in the Section 3.1), we aimed to compare computed and experimental data for synthetically available complexes. The typical size of these systems is around 100 atoms and therefore, high-level *ab initio* approaches are not feasible. We thus mostly focused on the performance of various DFT functionals, compared single- vs. multireference DFT approaches and studied solvent effects. We focused less on benchmarking of various basis sets which has been carried out on model system **11** (c.f. Figure S2 and Table S2). We thus decided to use scalar relativistic X2C approximation with x2c-TZVPall basis set as a default for the single-reference DFT whereas MC-PDFT calculations then employed converged (see Table 1) ANO-RCC-TZP/DZP(H) basis set and scalar-relativistic DKH2 approximations as a default. We have also included a very cheap and practical non-relativistic NR-TPSS/def2-SVP method for comparison, keeping in mind it has not performed optimally for the **11** ($\Delta E \approx 12$ kcal.mol^{-1} between the **11O** and **11P** endpoints). A fairly good performance of this method has been, however, mentioned in previous studies.[37]

The computed (X2C-TPSS/x2c-TZVPall//CPCM) equilibrium structures of **1–10** are shown in Figure 4, together with selected experimental parameters: interatomic distances and vibrational frequencies.

Equilibrium Geometries

A relatively scarce experimental data exists concerning the equilibrium distances of the studied [Cu$_2$O$_2$] complexes. They are available for systems **1**, **2**, **4**, and **10**. The experimental and calculated values are compared in Table 2 together with the RMSD (root-mean-square deviation) and MSD (mean signed deviation). Note that the negative MSD values indicate that the experimental bond length is shorter and *vice versa*. The other structural parameters, r_{Cu-O} and r_{Cu-N} distances are provided in Tables S5–S6.

As can be seen in Table 2, the best results are obtained using pure DFT functionals that give RMSD consistently near 0.1 Å, while larger deviations are observed for hybrid functionals and B97D. Note, that geometric parameters of **1**, **2**, and **4** are relatively insensitive to the level of theory, all within 0.1 Å (Tables 2, Tables S5-S6) while results for **10** show rather large variations. Interestingly, a very nice 'structural' agreement between the theory and experiment is also obtained at the NR-TPSS/def2-SVP and NR-TPSS/def2-TZVP levels of theory which are often used in computational investigations of the Cu$_2$O$_2$ systems.

The results in Table 2 suggest, that the equilibrium geometries are not as sensitive to relativistic effects as are the isomerization energies (discussed below). Concerning the usage of empirical-dispersion correction which is nowadays almost standard in the practical applications of the density functional theory, comparison has been made for the NR-TPSS(D3BJ)/def2-SVP level of theory, with and without the dispersion correction. As can be seen in the bottom of Table 2, the dispersion-correction influences mostly Cu–Cu distances (somewhat expectedly, D3 correction lowers the Cu–Cu distance, bringing the computed values somewhat closer to the experimental values). Thus, we recommend its usage. We note that except for the NR-TPSS functional, the RMSD is generally better for the r_{Cu-Cu} distance than that for the r_{O-O} distances (see the discussion above). Finally, the r_{Cu-O} and r_{Cu-N} distances provided in Tables S5–S6 are much less sensitive to the computational levels, all data within ca 0.1 Å for systems **1**, **2**, and **4**. For **10**,

Table 2. Theoretical results[a] for the r_{O-O} and r_{Cu-Cu} of **1**, **2**, **4**, and **10** with corresponding RMSD and MSD[b] values.

System	1	2	4	10	RMSD	MSD	1	2	4	10	RMSD	MSD
			r_{O-O}						r_{Cu-Cu}			
X2C-PBE/x2c-TZVPall	1.46	2.38	2.35	2.66	0.12	−0.07	3.53	2.72	2.79	3.29	0.10	−0.04
X2C-BP86/x2c-TZVPall	1.47	2.39	2.35	2.67	0.12	−0.08	3.50	2.72	2.72	3.24	0.09	<0
X2C-B97D/x2c-TZVPall	1.45	2.38	2.34	3.08	0.32	−0.17	3.54	2.74	2.78	3.18	0.05	−0.01
X2C-TPSS/x2c-TZVPall	1.48	2.39	2.35	2.61	0.10	−0.06	3.49	2.70	2.70	3.25	0.10	0.01
X2C-TPSSh/x2c-TZVPall	1.46	2.37	2.33	2.98	0.18	−0.08	3.30	2.69	2.68	2.95	0.16	0.14
X2C-B3LYP/x2c-TZVPall	1.46	2.36	2.33	3.09	0.33	−0.17	3.28	2.70	2.71	3.05	0.15	0.11
X2C-M06/x2c-TZVPall	1.42	2.34	2.31	3.05	0.31	−0.14	3.36	2.69	2.68	3.08	0.12	0.09
X2C-LH14t-calPBE/x2c-TZVPall	–[c]	2.34	2.32	3.01	0.34	−0.17	–[c]	2.71	2.75	3.04	0.04	0.04
X2C-CAM-B3LYP/x2c-TZVPall	1.46	2.32	2.30	2.90	0.24	−0.10	3.54	2.69	2.72	3.10	0.04	0.03
NR-TPSS/def2-TZVP	1.47	2.40	2.35	2.38	0.05	−0.01	3.51	2.72	2.74	3.18	0.06	0.01
NR-TPSS/def2-SVP	1.47	2.41	2.36	2.37	0.05	−0.01	3.53	2.74	2.78	3.21	0.07	−0.02
NR-TPSS/def2-SVP[d]	1.46	2.40	2.36	2.37	0.05	<0	3.63	2.76	2.85	3.25	0.10	−0.08
Experiment	*1.41*	*2.34*	*2.38*	*2.43*	*–*	*–*	*3.56*	*2.74*	*2.79*	*3.08*	*–*	*–*

[a] All calculations were done employing the CPCM (COSMO) solvation. [b] The negative MSD values indicate that the experimental bond length is shorter and vice versa. [c] Results for **1** could not be obtained in reasonable time. [d] Without dispersion correction.
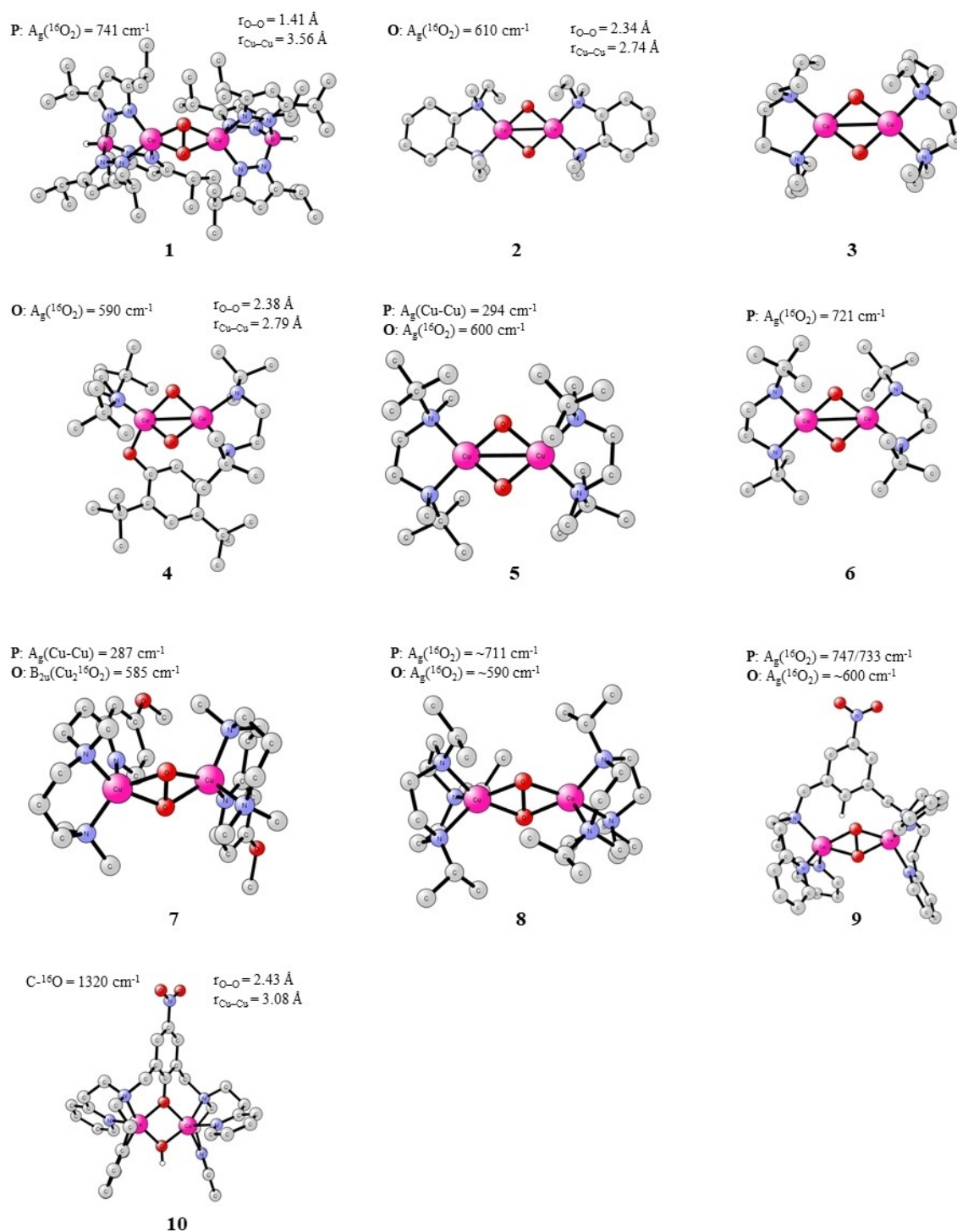
ChemPhysChem

Research Article
doi.org/10.1002/cphc.202200076

**Chemistry
Europe**
European Chemical
Societies Publishing

Figure 4. The X2C-TPSS/x2c-TZVPall/CPCM equilibrium geometries of studied systems **1**-**10**. The distances and vibrational modes values shown summarize the known experimental data. Computed data are compiled in Tables 2, S5, and S6.

larger errors are observed. Apparently, system **10** is problematic and may deserve more investigations in the future.

Thermodynamics

In the following, we will investigate the detailed thermodynamics of the **O**↔**P** equilibrium for **1**–**9**, defined as $X(\mathbf{O})$ - $X(\mathbf{P})$ where X stands for electronic energy (E), enthalpy (H) or Gibbs free energy (G), *in vacuo* or in solvent. The latter is mostly used

ChemPhysChem

Research Article
doi.org/10.1002/cphc.202200076

Chemistry Europe
European Chemical
Societies Publishing

Table 3. Comparison of different density functionals for the **O↔P** isomerization energy of systems **1–9**. Calculated at X2C-DFT/x2c-TZVPall/CPCM level with ZPVE and COSMO-RS correction for solvent included. Temperature was set up according to the experimental conditions. All values are in kcal.mol^{-1}.

System	1	2	3	4	5	6	7[a]	8[a]	9	Score
X2C-PBE/x2c-TZVPall	−1.8	−26.4	−20.9	−10.6	−8.5	−6.2	−5.1/−6.8/−6.4	−3.1/−4.1/−3.8	3.7	0.67
X2C-BP86/x2c-TZVPall	−5.3	−[b]	−23.4	−7.4	−10.3	−8.4	−7.3/−8.9/−8.5	−5.5/−6.6/−6.4	3.7	0.67
X2C-B97D/x2c-TZVPall	−2.0	−25.3	−20.6	−4.7	−7.5	−4.6	−0.5/−2.2/−1.8	−0.3/−1.2/−1.0	7.9	0.67
X2C-TPSS/x2c-TZVPall	−4.3	−33.1	−24.1	−10.6	−11.6	−8.6	−8.7/−10.5/−10.1	−6.2/−7.3/−7.1	−0.2	0.56
X2C-TPSSh/x2c-TZVPall	2.5	−28	−22.6	−1.8	−9.1	−6.0	−0.8/−2.4/−2.1	−0.8/−1.9/−1.7	4.9	0.78
X2C-B3LYP/x2c-TZVPall	12.4	−24.0	−18.4	10.0	1.4	−1.2	9.4/8.4/8.5	8.9/7.9/8.1	14.6	0.56
X2C-M06/x2c-TZVPall	10.3	−13.3	−7.8	13.6	5.0	7.9	15.4/14.4/14.5	13.5/12.4/12.8	20.6	0.67
X2C-LH14t-calPBE/x2c-TZVPall	–	−22.9	−16.9	−6.2	−1.1	0.7	8.6/8.8/8.8	12.0/11.2/11.4	11.6	0.88[c]
X2C-CAM-B3LYP/x2c-TZVPall[d]	23.7	−9.2	−23.7	7.1	12.2	12.8	20.1/19.7/19.7	23.7/22.6/23.0	21.5	0.67
DKH-MC-ftrevPBE/ANO-RCC-TZP & DZP(H)[e]	15.4	−9.0	−0.6	14.4	14.5	11.1	12.0/10.2/10.6	20.6/19.4/19.7	2.4	0.67
NR-TPSS/def2-SVP	4.6	−20.4	−15.1	−1.7	−4.1	−1.0	−0.1/−1.7/−1.3	1.6/0.4/0.6	9.3	0.81
Experiment	*P*	*O*	*O*	*O*	*O*	*P*	*P/O/O*	*P/O/P*	*P*	–

[a] Solvent-dependent systems in the order of CH_2Cl_2, THF, and acetone. [b] The ^{1}**P** isomer could not be located, all minimizations led to ^{1}**O**. [c] Results for **1** could not be obtained in a reasonable time; hence scoring was calculated over eight systems for LH14t-calPBE functional. [d] ZPVE correction for systems **1** and **3** were taken from B97D/x2c-TZVPall/CPCM results. [e] With MC-PDFT level of theory (MC-ftrevPBE//ANO-RCC-VDZP for H and ANO-RCC-VTZP for other atoms) we calculated single-point gas phase energy for both isomers **O** and **P** based on geometries from X2C-TPSS/x2c-TZVPall/CPCM; COSMO_RS and ZPVE correction were taken from X2C-TPSS/x2c-TZVPall/CPCM results.

when comparing calculated and experimental data in liquid phase. The negative values indicate the greater stability of the **O** (and *vice versa*). Since for most of the experimental systems, the only information available is which isomer is observed (i.e. which of the **O/P** is more stable under experimental conditions) we introduce a simple 'binary' *scoring function*. This very simple function increases its value by 1 when the corresponding method correctly predicts the more stable isomer, and 0, if not. Therefore, the score *m/n* means that *m* out of the total number of *n* systems were correctly predicted by the given method (in Table 3, this is then expressed as the numerical ratio *m/n*). In addition, there are few systems, where the experimental thermodynamic values are available; these are discussed separately in more details. Moreover, for systems **7** and **8**, experimental values for different solvents are available (and thus, an average over the solvents was then added to our scoring function).

The results of thermochemical calculations are summarized in Table 3. It can be seen that by employing X2C relativistic approach, the TZ-quality basis set, and the COSMO-RS solvation method, the general agreement (quantified by the scoring function) is rather satisfactory, considering the complexity of the problem and various subtleties of electronic structure methods mentioned in the previous section. Typically, 60–70% of the **P/O** equilibria are correctly predicted. TPSSh and LH14t-calPBE are slightly outperforming other functionals with 80–90% success rate of the prediction. Moreover, the two wrongly predicted values of isomerization energy are close to zero (< 3 kcal.mol^{-1} for TPSSh and also < 1 kcal.mol^{-1} for B97D). Somewhat surprisingly, the MC-PDFT/ftrev-PBE, method that performed well for model **11** (Figure 2) does not provide any improvement over the single-reference DFT for experimental systems. Even more surprisingly, we note that a very simple and cheap non-relativistic NR-TPSS/def2-SVP level gives 0.81 score which is the second best of all methods used. This is apparently due to the cancellation of errors, where small basis set cancels the effects of relativity (cf. Figure S2). Finally, as can be seen

from the data presented in Table 3, we observed that pure (GGA or meta-GGA) functionals favor the **O** isomer whereas exact exchange admixture favors the **P** isomer. This is especially true for M06 with 27% of HF exchange. The same trend is seen concerning the range-separated CAM-B3LYP.

An important question is how different levels of inclusion of solvent effects and thermodynamics affect the calculated results. The data in Table 4 reveal that for most of the systems, it is not vital to include all physical corrections (mostly
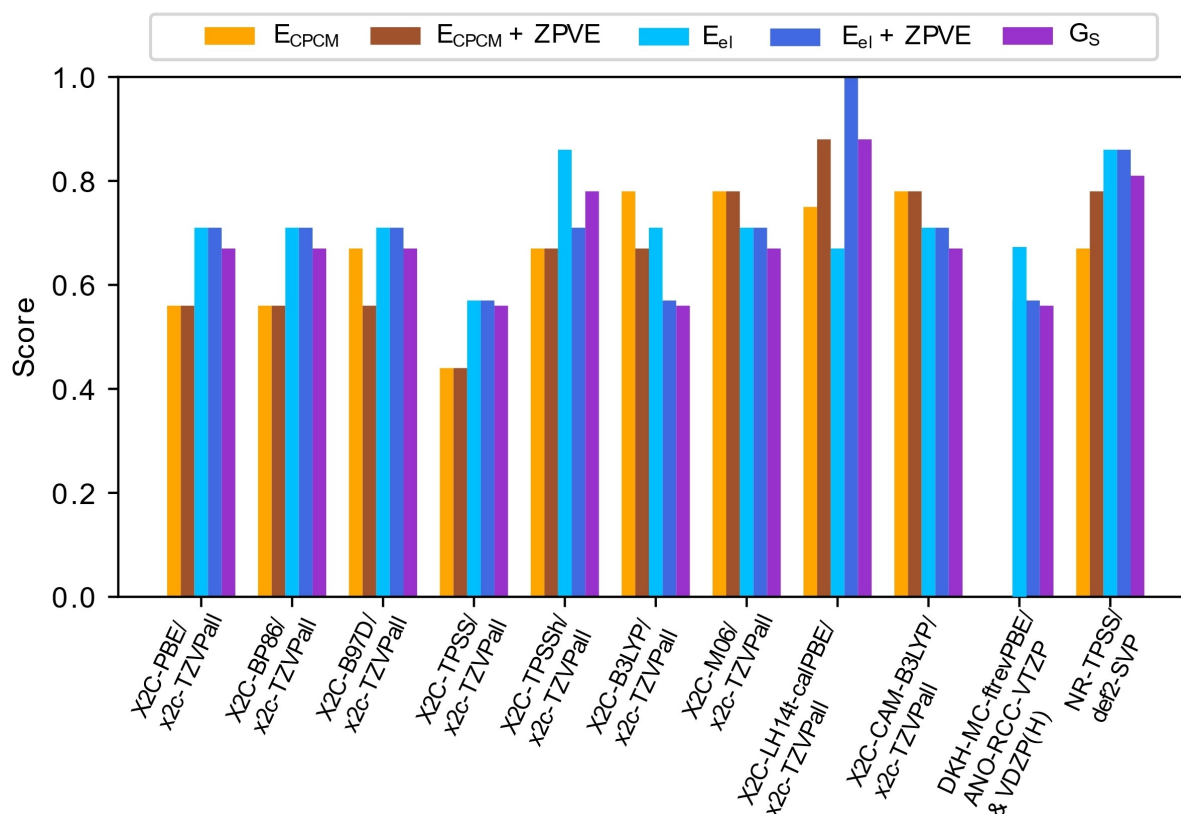
Table 4. Analysis of different energy terms contributing to the **O↔P** isomerization (free) energy in systems **1–9**. All values are computed employing the CPCM equilibrium geometries at the corresponding X2C-functional/x2c-TZVPall level of theory. All energy values are in Tables S7–S10.

Functional	$E_{el;}$[a]	E_{CPCM}	E_{el} $+E_{ZPVE}$[a]	E_{CPCM} $+E_{ZPVE}$	G_s[b]
X2C-PBE/x2c-TZVPall	0.71	0.56	0.71	0.56	0.67
X2C-BP86/x2c-TZVPall	0.71	0.56	0.71	0.56	0.67
X2C-B97D/x2c-TZVPall	0.71	0.67	0.71	0.56	0.67
X2C-TPSS/x2c-TZVPall	0.57	0.44	0.57	0.44	0.56
X2C-TPSSh/x2c-TZVPall	0.86	0.67	0.71	0.67	0.78
X2C-B3LYP/x2c-TZVPall	0.71	0.78	0.57	0.67	0.56
X2C-M06/x2c-TZVPall	0.71	0.78	0.71	0.78	0.67
X2C-LH14t-calPBE/x2c-TZVPall	0.67[c]	0.75[c]	1.00[c]	0.88[c]	0.88[c]
X2C-CAM-B3LYP/x2c-TZVPall	0.71	0.78	0.71	0.78	0.67
DKH-MC-ftrevPBE/ANO-RCC-TZP & DZP(H)[d]	0.67	–[e]	0.57	–[e]	0.56
NR-TPSS/def2-SVP	0.86	0.67	0.86	0.78	0.81

[a] Solvent-dependent systems are not included in scoring of E_{el} and $E_{el}+E_{ZPVE}$ level of theory. [b] Numerical values given in Table 3. [c] Results for **1** could not be obtained in a reasonable time for LH14t-calPBE functional; hence scoring was calculated over six or eight systems for LH14t-calPBE functional [d] MC-PDFT level of theory (MC-PDFT//ftrevPBE//ANO-RCC-DZP for H and ANO-RCC-TZP for other atoms) we calculated upon TPSS/x2c-TZVPall/CPCM geometry. [e] We could not obtain result at MC-PDFT level of theory with CPCM included.

ChemPhysChem

Research Article
doi.org/10.1002/cphc.202200076

Chemistry Europe
European Chemical
Societies Publishing

solvation) to correctly predict the 'sign' of the **P/O** equilibrium. The computed electronic energy as such and choice of the DFT functional seem to be the most important parameters. For clarity, the results of Table 4 are visualized in Figure 5. It clearly illustrates, that due to the cancellation of various effects, the gas-phase electronic energy is rather close to G_s which should be the quantity to be compared with the liquid-phase experiments.

Regarding the solvation effects, we also compared the CPCM and COSMO-RS solvation models on systems **7** and **8** (c.f.,

Table S11). The latter performs slightly better which seems to matter when the **O/P** equilibrium is close to thermoneutral.

For few systems, the quantitative thermochemical data (*H* values) were available from experiments. The comparison of the experimental and computed data is shown in Table 5. For system **2**, all tested functionals correctly predicted the more stable **O** isomer. However, except for the M06, the isomerization energy is overestimated by 6–19 kcal.mol^{-1}. For the remaining systems, the differences between computed and experimental values of ΔH are smaller – typically 1–9 kcal.mol^{-1} for GGA functionals and larger for hybrid and local-hybrid functionals,

Figure 5. Analysis of different energy terms contributing to the O↔P isomerization (free) energy in systems **1–9**. All values are computed employing the CPCM equilibrium geometries obtained at the corresponding X2C-functional/x2c-TZVPall level of theory. All energy values are in Tables S7–S10.

Table 5. Comparison of the calculated and experimental ΔH(P/O) values. All calculations were done the CPCM (COSMO) solvation. All values in kcal.mol^{-1}.

System Solvent	**2** CH$_2$Cl$_2$	**6** CH$_2$Cl$_2$	**7**[a] THF	**8** THF	RMSD	MSD[b]
X2C-PBE/x2c-TZVPall	−24.6	−5.8	−4.9	−2.0	7.3	5.8
X2C-BP86/x2c-TZVPall	−26.8	−7.9	−7.3	−4.9	9.2	8.3
X2C-B97D/x2c-TZVPall	−21.9	−3.5	−0.5	1.2	5.4	2.7
X2C-TPSS/x2c-TZVPall	−31.2	−8.7	−8.7	−5.5	11.5	10.1
X2C-TPSSh/x2c-TZVPall	−26.3	−6.0	−1.3	−0.2	7.8	5.0
X2C-B3LYP/x2c-TZVPall	−21.9	−1.3	9.1	9.7	8.8	−2.4
X2C-M06/x2c-TZVPall	−11.0	8.5	14.7	14.5	11.8	−10.2
X2C-LH14t-calPBE/x2c-TZVPall	−19.6	1.6	10.0	13.6	9.8	−4.9
X2C-CAM-B3LYP/x2c-TZVPall	−5.8	14.7	21.1	24.8	18.7	−17.2
NR-TPSS/def2-SVP	−19.1	−0.3	<0	1.9	3.9	0.9
Experiment	*−11.8*	*−0.6*	*−3.8 to −0.6*	*−0.9*		

[a] For RMSD and MSD calculations for system **7** we use value of −0.6 kcal.mol^{-1}. [b] The negative MSD values indicate that the experimental enthalpy value is smaller and *vice versa*.

except for TPSSh. These methods strongly and erroneously overstabilize the **P** isomer (by 10–25 kcal.mol^{-1}). In line with the above observation, we notice that the best agreement between theory and experiment is obtained by using NR-TPSS/def2-SVP, due to the cancellation of errors. This is not very encouraging observation from the theoretical point of view, but may somehow justify usage of very cheap and simple approach(es) in studying the reactivity of larger-size CBC systems.
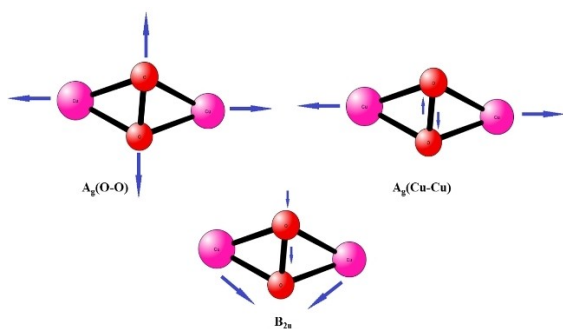
The analysis of the fortuitous error cancellation is available in Table S12.

Finally, a very important qualitative observation relevant for the CBC chemistry that can inferred from Table 2 is that, both experimentally and theoretically, the **O** (bis-μ-oxo) isomer is favored when there are two coordinating ligands on each of the two Cu whereas the peroxo (**P**) isomer is preferred in case of three coordinating ligands on Cu ions. Similar observation was previously made by Cramer and coworkers.[35]

Vibrational Frequencies

For most of the experimentally characterized systems (**1–10**), selected Cu_2O_2 core distances and vibrational modes were reported in the literature. Here, we focus on three most important Cu_2O_2 stretching modes: Cu—Cu (A$_g$), O—O (A$_g$), and Cu_2O_2 (B$_{2u}$). They are illustrated in Figure 6. Available experimental data are collected in Table 6.

Experimental and calculated vibrational modes for **O** and **P** isomers of studied systems as well as for the C—O stretch of the hydroxylated product (**H**) (**10**) are compared in Tables 7. RMSD values are given in Table 8.

Figure 6. O—O (A$_g$), Cu—Cu (A$_g$), and Cu_2O_2 (B$_{2u}$) vibrational modes examined in this study.

Table 6. Summary of experimentally known vibrational frequencies of the Cu_2O_2 core. All values in cm^{-1}.

System	Peroxo A$_g$ $\nu(^{16}O_2)$	Δ ($^{18}O_2$)[a]	A$_g$ ν(Cu—Cu)	Oxo A$_g$ $\nu(^{16}O_2)$	Δ ($^{18}O_2$)[a]	B$_{2u}$ $\nu(Cu_2{}^{16}O_2)$	Δ ($^{18}O_2$)^a	Hydroxo ν(C-^{16}O)
1[b]	741 (698)	22						
2				610	23			
4[b]				590 (585)	20			
5			294	600	−24			
6	721	40						
7			287			585	561	
8	∼711-715			∼589–595				
9	747/733	40/38		∼600				
10								1320

[a] $\Delta(^{18}O_2)$ shift is the vibration $^{16}O_2$–$^{18}O_2$. [b] Values in parenthesis: **1**: 698 cm^{-1} refers to ^{16}O–^{18}O substitution; **4**: 585 cm^{-1} refers to **4** with $^{16}O_2$/^{18}OPhtBu$_2$.

Table 7. Comparison between experimental and theoretical vibrational frequencies. All calculations were done employing the X2C relativistic approximation, x2c-TZVPall basis set and the CPCM (COSMO) solvation model, unless mentioned otherwise. All values in cm^{-1}.

Isomer	Vibration	Sys.	PBE	BP86	B97D	TPSS	TPSSh	B3-LYP	M06	LH14t-calPBE	CAM-B3LYP	NR-TPSS	Exp
O	$\nu(^{16}O_2)$	**2**	619	624	612	635	653	650	654	659	681	614	610
	$\nu(^{18}O_2)$	**2**	590	595	583	606	622	619	623	628	649	586	587
	$\nu(^{16}O_2)$	**4**	599	604	587	620	639	633	649	639	669	592	590
	$\nu(^{18}O_2)$	**4**	570	576	560	592	610	604	618	609	638	565	570
	$\nu(^{16}O_2)$	**5**	611	617	605	627	645	643	647	649	673	607	600
	$\nu(^{18}O_2)$	**5**	581	587	576	597	614	612	616	618	640	579	624
	$\nu(Cu_2{}^{16}O_2)$	**7**	560	563	556	601	623	599	599	608	635	548	585
	$\nu(Cu_2{}^{18}O_2)$	**7**	535	538	531	574	596	572	573	581	607	524	561
	$\nu(^{16}O_2)$	**8**	588	595	588	607	625	624	629	631	658	597	592
	$\nu(^{16}O_2)$	**9**	582	587	583	599	621	622	638	625	654	584	600
P	$\nu(^{16}O_2)$	**1**	843	830	853	811	870	872	937	–	–	839	741
	$\nu(^{18}O_2)$	**1**	796	783	804	766	821	823	884	–	–	792	719
	ν(Cu-Cu)	**5**	289	286	306	285	306	340	331	314	334	302	294
	$\nu(^{16}O_2)$	**6**	754	729	788	716	797	853	882	908	868	766	721
	$\nu(^{18}O_2)$	**6**	712	689	744	678	753	806	832	857	819	723	681
	ν(Cu-Cu)	**7**	270	273	277	274	300	291	301	301	318	286	287
	$\nu(^{16}O_2)$	**8**	818	799	832	786	818	832	891	892	885	806	713
	$\nu(^{16}O_2)$	**9**	929	918	942	892	904	902	969	959	952	944	747
	$\nu(^{18}O_2)$	**9**	876	865	889	841	852	851	913	904	897	891	707
H	$\nu(C-^{16}O)$	**10**	1417	1409	1454	1399	1443	1500	1546	–	1527	1385	1320

ChemPhysChem

Research Article
doi.org/10.1002/cphc.202200076

Chemistry
Europe
European Chemical
Societies Publishing

Table 8. RMSD and MSD values for vibrational modes (theory vs. experiment).

	O		P		both	
	RMSD	MSD	RMSD	MSD	RMSD	MSD
X2C-PBE/x2c-TZVPall	19.4	8.5	100.6	−75.1	70.7	−31.1
X2C-BP86/x2c-TZVPall	18.2	3.1	90.7	−62.5	63.8	−28.0
X2C-B97D/x2c-TZVPall	21.3	13.8	112.4	−91.5	78.9	−36.1
X2C-TPSS/x2c-TZVPall	21.2	−13.9	75.7	−48.7	54.3	−30.4
X2C-TPSSh/x2c-TZVPall	36.6	−32.8	102.6	−89.9	75.4	−59.9
X2C-B3LYP/x2c-TZVPall	30.8	−25.9	116.5	−106.6	83.2	−64.1
X2C-M06/x2c-TZVPall	38.0	−32.7	163.0	−147.7	115.5	−87.2
X2C-LH14t-calPBE/x2c-TZVPall[a]	36.9	−32.9	161.6	−140.8	107.5	−77.3
X2C-CAM-B3LYP/x2c-TZVPall[a]	60.9	−58.4	146.8	−131.8	105.1	−88.6
NR-TPSS/def2-SVP	22.7	12.3	105.4	−82.0	74.4	−32.4

[a] RMSD was calculated only for all **O** and **P** isomer except system

Non-hybrid functionals in Table 7 perform somewhat better than hybrids. For the **P** isomer, all DFT functionals overestimate the ν(O–O) stretch (by ~100 cm^{-1}, with the exception of **6** for which the agreement is better). On the contrary, the ν(Cu–Cu) stretch is predicted quite satisfactorily. Pure functionals (PBE, PB86 and TPSS) perform better. Overestimated O–O stretches seem to be in accordance with the observed underestimating of the O–O bond length in the model systems (too strong O–O bond). This trend of overestimation of the O–O stretching frequency in side-on peroxo Cu(II)$_2$ species has been reported previously.[10] The best agreement (the smallest deviation from experimental value) is observed for the meta-GGA TPSS functional.

To quantify the performance of various functionals, we have calculated RMSD and MSD values for modes available experimentally. They are shown in Table 8. This has been done separately for the **O** and **P** isomers, and also for both of them. We can clearly see that better agreement is indeed achieved for the **O** isomer. Pure functionals give RMSD around ~20 cm^{-1}, whereas hybrid functional have an error of ~30–40 cm^{-1}. For the **P**, the discrepancies are much higher (RMSD values range between 75 cm^{-1} and 163 cm^{-1} for TPSS and M06, respectively). Considering vibrational modes for both isomers (overall performance), the lowest deviation from experimental values were obtained using TPSS functional. We also compared calculated C–O vibrational mode for the system **10**, which is a hydroxylated product. We obtained values in range 1385–1546 cm^{-1}. Again, hybrid functionals overestimate the experimental values. The best agreement with experiment was obtained with the NR-TPSS and TPSS with relativity and in bigger basis set, the difference between the two computed values is only 14 cm^{-1}.

It can be mentioned that calculated vibrational frequencies are almost the same in the gas phase and in solvent (PCM). In case of NR-TPSS/def2-SVP, we calculated frequencies in CPCM model and in gas phase (Table S13). The difference for the computed vibrational modes, across all systems studied (all isomers: ^{1}**O**, ^{1}**P**, ^{3}**P**) varies from −5.4 to 5.4 cm^{-1}, with an average difference from 0.4 to 1.7 cm^{-1}. Usually frequencies obtained from CPCM model are slightly lower than from gas phase calculations. Thus, the largest errors in frequency calculations

are originating from the DFT functional whereas solvent effects are of minor importance.

Discussion and Conclusions

Model System 11

In this work, we first took a fresh look at the model **11O**↔**11P** isomerization coordinate. Unlike the older works, we refrained from using ECP's on Cu and used scalar relativistic X2C and DKH2 approximations in CCSD(T), DFT, MC-PDFT and MRCI+Q calculations. Also we used slightly refined reaction coordinate which is based on the relaxed scan of the O–O distance, instead of interpolated 'Cartesian geometries'. We tend to believe that the relativistic X2C-CCSD(T)/UKS/QZ calculations on a refined coordinate provide a new benchmark for system **11**, with the predicted **P/O** energy difference of 5–6 kcal.mol^{-1} (in favor of **P**) and a barrier of ~8 kcal.mol^{-1}.

On the other hand, we do not recommend to use small-active space MR wave function methods. It seems that the correlation treatment does not cure the insufficiency of too small active space. This can be demonstrated on the MR-CI(8,6)+Q results where the barrier between **11O** and **11P** disappears and the local minimum for **11O** is not found. At the same time MRCI+Q calculations predict large dip of ~5 kcal.mol^{-1} on the reaction coordinate around $r_{O–O} \approx 1.6$ Å). Most of this is attributed to the insufficient active space, since much smaller (shallower) dip of ~1 kcal.mol^{-1} at $r_{O–O} \approx 1.5–1.6$ Å is obtained in the UCCSD(T)/UKS, as well as in the previous DKH-CASPT2(24,28) and CR-CCSD(T)$_L$ calculations (Figure S1). Most of the DFT functionals then predict the $r_{O–O} \approx 1.40–1.45$ Å (c.f. Figures 2 and S1–S2).

The MC-PDFT, in particular the MC-trevPBE and MC-ft-revPBE, provide much better agreement with the "reference" UCCSD(T)/UKS/QZ energy profile. The same holds true for many single-reference DFT methods with the relativistic X2C approximation and a TZ-quality basis set (Figure 3.) The barrier seems to be a bit overestimated, but most of the functionals give reasonable energy difference between **11P** and **11O**, 2–10 kcal.mol^{-1} (Figure 3), whereas the best theoretical value is estimated to be 5–6 kcal.mol^{-1} (see above). The same result is

ChemPhysChem

Research Article
doi.org/10.1002/cphc.202200076

Chemistry
Europe
European Chemical
Societies Publishing

obtained with, for example BP86 and TPSSh functionals. Much 'wilder' data were observed using ECPs on Cu and Yamaguchi correction for energy in previous works, often spanning several tens of kcal.mol^{-1}.[35]

The tested MC-PDFT functionals provide qualitatively similar **11O↔11P** isomerization curves (Figure 2, Table 1) when using converged ANO-RCC-TZP basis set and relativistic DKH2 approximation, with **P/O** energy difference from 1–6 kcal.mol^{-1}, except for the MC-LSDA based approximations that (likely incorrectly) predict the **11O** isomer to be more stable.

Experimental Systems

The most important question addressed in this work was, whether we can properly describe the experimental **O↔P** equilibrium in [Cu_2O_2] systems, presumably with cost-effective DFT methods. To do so, we need to fully understand how different physical effects contribute to the computed thermodynamic data. We have shown that for systems with small **P/O** energy gap which might be, moreover, solvent dependent, all terms matter. On the other hand, systems where the energy difference between **O** and **P** is larger, the contributions other than the electronic energy will be less important.

Geometries

To assess the accuracy of the computed equilibrium geometries, only scarce experimental data were available. Most of the functionals perform very well on systems **1**, **2**, **4**, while occasionally (for **10**) hybrid functionals seem to fail. Notably, the (very) cheap NR-TPSS/def2-SVP level gives excellent agreement between theory and experiment and offers probably the most favourable price/performance ratio. Of the other functionals, we mention that the local-hybrid, LH14t-calPBE, and meta-GGA TPSS, also give quite good agreement between theory and experiment.

Thermodynamics of the O↔P Equilibrium

Using converged basis set of x2c-TZVPall quality (Figure S2) and X2C relativistic approximation, we concentrated on role of the DFT functional as well as the role of different thermodynamic and solvation corrections on the **P/O** energy difference. The short (and expected) answer is that DFT functional matters most, while ZPVE, PCM, and ΔG_{solv} corrections become only important when the **P/O** energy gap is small, which may lead to the solvent dependence (sometimes observed in the experiment). Importantly, the effects of ZPVE and solvation tend to cancel each other (Figure 5). Thus, paradoxically, the best results that include all of these corrections are similar to the gas-phase electronic energies, E_g, calculated at the PCM equilibrium geometries. Again, the cheap NR-TPSS/def2-SVP approach gives surprisingly good results.

Solvation model. For solvation purposes we examined CPCM and COSMO-RS models. The latter perform slightly better which matters when the **O/P** equilibrium is close to zero.

Vibrational Frequencies

In general, better agreement between calculated and experimental vibrational frequencies is observed for the **O** isomer rather than for **P** isomer. Pure functionals give better agreement with the experimental frequencies than the hybrid ones. Interestingly, the local-hybrid LH14t-calPBE was found to be quite good for geometries and energies but its performance was found to be poor for vibrational frequencies.

We may summarize the results of our extensive computations as follows: (1) To correctly account for all physics involved in the coupled-binuclear systems, one-component relativistic approximation, e.g. X2C, or DKH2, should be used, together with basis sets of at least triple-zeta quality. (2) To obtain good geometries of the [Cu_2O_2] core, pure DFT functionals and also local-hybrid LH14t-calPBE, are recommended. (3) For energetics, pure DFT functionals perform quite well. (4) The same holds true for vibrational frequencies, pure (computationally cheaper) DFT functionals also perform quite satisfactorily, both for the **O** and **P** isomers. Hybrid functional have tendency to overestimate the frequencies. Finally, the NR-TPSS/def2-SVP approach that gains from error cancellations (Figure S1) presents a cheap and fast alternative way for calculations of larger [Cu_2O_2] enzymatic systems. It performs reasonably well for geometries, energetics, and also vibrational frequencies.

Associated Content

All equilibrium geometries and primary energetic data. Tables S1–S13, Figures S1–S5. This material is available free of charge via the Internet at XX.

Conflict of Interest

The authors declare no conflict of interest.

Data Availability Statement

The data that support the findings of this study are available in the supplementary material of this article.

[1] E. I. Solomon, D. E. Heppner, E. M. Johnston, J. W. Ginsbach, J. Cirera, M. Qayyum, M. T. Kieber-Emmons, C. H. Kjaergaard, R. G. Hadt, L. Tian, *Chem. Rev.* **2014**, *114*, 3659–3853.

[2] C. E. Elwell, N. L. Gagnon, B. D. Neisen, D. Dhar, A. D. Spaeth, G. M. Yee, W. B. Tolman, *Chem. Rev.* **2017**, *117*, 2059–2107.

[3] H. Decker, T. Schweikardt, D. Nillius, U. Salzbrunn, E. Jaenicke, F. Tuczek, *Gene* **2007**, *398*, 183–191.

[4] Y. Matoba, T. Kumagai, A. Yamamoto, H. Yoshitsu, M. Sugiyama, *J. Biol. Chem.* **2006**, *281*, 8981–8990.

[5] K. A. Magnus, B. Hazes, H. Ton-That, C. Bonaventura, J. Bonaventura, W. G. J. Hol, *Proteins Struct. Funct. Genet.* **1994**, *19*, 302–309.

[6] J. M. Brown, L. Powers, B. Kincaid, J. A. Larrabee, T. G. Spiro, *J. Am. Chem. Soc.* **1980**, *102*, 4210–4216.

[7] G. L. Woolery, L. Powers, M. Winkler, E. I. Solomon, K. Lerch, T. G. Spiro, *Biochim. Biophys. Acta* **1984**, *788*, 155–161.

[8] E. Solem, F. Tuczek, H. Decker, *Angew. Chem. Int. Ed.* **2016**, *55*, 2884–2888; *Angew. Chem.* **2016**, *128*, 2934–2938.

[9] L. M. Mirica, M. Vance, D. J. Rudd, B. Hedman, K. O. Hodgson, E. I. Solomon, T. D. P. Stack, *Science* **2005**, *308*, 1890.

[10] M. F. Qayyum, R. Sarangi, K. Fujisawa, T. D. P. Stack, K. D. Karlin, K. O. Hodgson, B. Hedman, E. I. Solomon, *J. Am. Chem. Soc.* **2013**, *135*, 17417–17431.

[11] S. Binder, M. Salomone-Stagni, R. Haase, B. Schulz, A. Eich, G. Henkel, M. Rübhausen, S. Herres-Pawlis, W. Meyer-Klaucke, *J. Phys. Conf. Ser.* **2009**, *190*, 012201.

[12] S. Herres-Pawlis, U. Flörke, G. Henkel, *Eur. J. Inorg. Chem.* **2005**, *2005*, 3815–3824.

[13] K. D. Karlin, J. C. Hayes, Y. Gultneh, R. W. Cruse, J. W. McKown, J. P. Hutchinson, J. Zubieta, *J. Am. Chem. Soc.* **1984**, *106*, 2121–2128.

[14] N. Kitajima, K. Fujisawa, C. Fujimoto, Y. Morooka, S. Hashimoto, T. Kitagawa, K. Toriumi, K. Tatsumi, A. Nakamura, *J. Am. Chem. Soc.* **1992**, *114*, 1277–1291.

[15] N. Kitajima, K. Fujisawa, Y. Morooka, K. Toriumi, *J. Am. Chem. Soc.* **1989**, *111*, 8975–8976.

[16] J. Serrano-Plana, I. Garcia-Bosch, A. Company, M. Costas, *Acc. Chem. Res.* **2015**, *48*, 2397–2406.

[17] J. L. DuBois, P. Mukherjee, A. M. Collier, J. M. Mayer, E. I. Solomon, B. Hedman, T. D. P. Stack, K. O. Hodgson, *J. Am. Chem. Soc.* **1997**, *119*, 8578–8579.

[18] C. X. Zhang, H.-C. Liang, E.-i. Kim, Q.-F. Gan, Z. Tyeklár, K.-C. Lam, A. L. Rheingold, S. Kaderli, A. D. Zuberbühler, K. D. Karlin, *Chem. Commun.* **2001**, *137*, 631–632.

[19] H.-C. Liang, C. X. Zhang, M. J. Henson, R. D. Sommer, K. R. Hatwell, S. Kaderli, A. D. Zuberbühler, A. L. Rheingold, E. I. Solomon, K. D. Karlin, *J. Am. Chem. Soc.* **2002**, *124*, 4170–4171.

[20] T. Osako, K. Ohkubo, M. Taki, Y. Tachi, S. Fukuzumi, S. Itoh, *J. Am. Chem. Soc.* **2003**, *125*, 11027–11033.

[21] M. Taki, S. Teramae, S. Nagatomo, Y. Tachi, T. Kitagawa, S. Itoh, S. Fukuzumi, *J. Am. Chem. Soc.* **2002**, *124*, 6367–6377.

[22] A. P. Cole, V. Mahadevan, L. M. Mirica, X. Ottenwaelder, T. D. P. Stack, *Inorg. Chem.* **2005**, *44*, 7345–7364.

[23] D. Maiti, J. S. Woertink, A. A. Narducci Sarjeant, E. I. Solomon, K. D. Karlin, *Inorg. Chem.* **2008**, *47*, 3787–3800.

[24] R. Haase, T. Beschnitt, U. Flörke, S. Herres-Pawlis, *Inorg. Chim. Acta* **2011**, *374*, 546–557.

[25] M. T. Kieber-Emmons, J. W. Ginsbach, P. K. Wick, H. R. Lucas, M. E. Helton, B. Lucchese, M. Suzuki, A. D. Zuberbühler, K. D. Karlin, E. I. Solomon, *Angew. Chem. Int. Ed.* **2014**, *53*, 4935–4939; *Angew. Chem.* **2014**, *126*, 5035–5039.

[26] J. A. Halfen, S. Mahapatra, E. C. Wilkinson, S. Kaderli, V. G. Young, L. Que, A. D. Zuberbühler, W. B. Tolman, *Science* **1996**, *271*, 1397.

[27] G. J. Karahalis, A. Thangavel, B. Chica, J. Bacsa, R. B. Dyer, C. C. Scarborough, *Inorg. Chem.* **2016**, *55*, 1102–1107.

[28] L. Q. Hatcher, M. A. Vance, A. A. Narducci Sarjeant, E. I. Solomon, K. D. Karlin, *Inorg. Chem.* **2006**, *45*, 3004–3013.

[29] V. Mahadevan, Z. Hou, A. P. Cole, D. E. Root, T. K. Lal, E. I. Solomon, T. D. P. Stack, *J. Am. Chem. Soc.* **1997**, *119*, 11996–11997.

[30] H. V. Obias, Y. Lin, N. N. Murthy, E. Pidcock, E. I. Solomon, M. Ralle, N. J. Blackburn, Y.-M. Neuhold, A. D. Zuberbühler, K. D. Karlin, *J. Am. Chem. Soc.* **1998**, *120*, 12960–12961.

[31] V. Mahadevan, M. J. Henson, E. I. Solomon, T. D. P. Stack, *J. Am. Chem. Soc.* **2000**, *122*, 10249–10250.

[32] J. Cahoy, P. L. Holland, W. B. Tolman, *Inorg. Chem.* **1999**, *38*, 2161–2168.

[33] K. D. Karlin, M. S. Nasir, B. I. Cohen, R. W. Cruse, S. Kaderli, A. D. Zuberbuehler, *J. Am. Chem. Soc.* **1994**, *116*, 1324–1336.

[34] E. Pidcock, H. V. Obias, C. X. Zhang, K. D. Karlin, E. I. Solomon, *J. Am. Chem. Soc.* **1998**, *120*, 7841–7847.

[35] C. J. Cramer, M. Włoch, P. Piecuch, C. Puzzarini, L. Gagliardi, *J. Phys. Chem. A* **2006**, *110*, 1991–2004.

[36] Y. Kurashige, J. Chalupský, T. N. Lan, T. Yanai, *J. Chem. Phys.* **2014**, *141*, 174111.

[37] J. L. Lewin, D. E. Heppner, C. J. Cramer, *J. Biol. Inorg. Chem.* **2007**, *12*, 1221–1234.

[38] D. G. Liakos, F. Neese, *J. Chem. Theory Comput.* **2011**, *7*, 1511–1523.

[39] F. Neese, D. G. Liakos, S. Ye, *J. Biol. Inorg. Chem.* **2011**, *16*, 821–829.

[40] Q. M. Phung, S. Wouters, K. Pierloot, *J. Chem. Theory Comput.* **2016**, *12*, 4352–4361.

[41] M. Witte, S. Herres-Pawlis, *Phys. Chem. Chem. Phys.* **2017**, *19*, 26880–26889.

[42] M. Rohrmüller, S. Herres-Pawlis, M. Witte, W. G. Schmidt, *J. Comput. Chem.* **2013**, *34*, 1035–1045.

[43] S. Herres-Pawlis, P. Verma, R. Haase, P. Kang, C. T. Lyons, E. C. Wasinger, U. Flörke, G. Henkel, T. D. P. Stack, *J. Am. Chem. Soc.* **2009**, *131*, 1154–1169.

[44] S. Herres-Pawlis, R. Haase, P. Verma, A. Hoffmann, P. Kang, T. D. P. Stack, *Eur. J. Inorg. Chem.* **2015**, *2015*, 5426–5436.

[45] A. Hoffmann, S. Herres-Pawlis, *Phys. Chem. Chem. Phys.* **2016**, *18*, 6430–6440.

[46] A. Hoffmann, S. Herres-Pawlis, *Chem. Commun.* **2014**, *50*, 403–405.

[47] B. T. Op't Holt, M. A. Vance, L. M. Mirica, D. E. Heppner, T. D. P. Stack, E. I. Solomon, *J. Am. Chem. Soc.* **2009**, *131*, 6421–6438.

[48] M. Rohrmüller, A. Hoffmann, C. Thierfelder, S. Herres-Pawlis, W. G. Schmidt, *J. Comput. Chem.* **2015**, *36*, 1672–1685.

[49] University of Karlsruhe and Forschungszentrum Karlsruhe GmbH **1989–2007**, p. http://www.turbomole.com.

[50] D. Peng, M. Reiher, *Theor. Chem. Acc.* **2012**, *131*, 1081.

[51] P. A. M. Dirac, R. H. Fowler, *Proc. R. Soc. Lond. A Math. Phys. Sci.* **1929**, *123*, 714–733.

[52] J. P. Perdew, Y. Wang, *Phys. Rev. B* **1992**, *45*, 13244–13249.

[53] J. C. Slater, *Phys. Rev.* **1951**, *81*, 385–390.

[54] J. Tao, J. P. Perdew, V. N. Staroverov, G. E. Scuseria, *Phys. Rev. Lett.* **2003**, *91*, 146401.

[55] P. Pollak, F. Weigend, *J. Chem. Theory Comput.* **2017**, *13*, 3696–3705.

[56] S. Grimme, J. Antony, S. Ehrlich, H. Krieg, *J. Chem. Phys.* **2010**, *132*.

[57] A. Klamt, G. Schüürmann, *J. Chem. Soc. Perkin Trans. 2* **1993**, 799–805.

[58] L. Noodleman, *J. Chem. Phys.* **1981**, *74*, 5737–5743.

[59] L. Noodleman, E. R. Davidson, *Chem. Phys.* **1986**, *109*, 131–143.

[60] J. P. Perdew, K. Burke, M. Ernzerhof, *Phys. Rev. Lett.* **1996**, *77*, 3865–3868.

[61] A. D. Becke, *Phys. Rev. A* **1988**, *38*, 3098–3100.

[62] J. P. Perdew, *Phys. Rev. B* **1986**, *33*, 8822–8824.

[63] S. H. Vosko, L. Wilk, M. Nusair, *Can. J. Phys.* **1980**, *58*, 1200–1211.

[64] S. Grimme, *J. Comput. Chem.* **2006**, *27*, 1787–1799.

[65] V. N. Staroverov, G. E. Scuseria, J. Tao, J. P. Perdew, *J. Chem. Phys.* **2003**, *119*, 12129–12137.

[66] A. D. Becke, *J. Chem. Phys.* **1993**, *98*, 5648–5652.

[67] C. Lee, W. Yang, R. G. Parr, *Phys. Rev. B* **1988**, *37*, 785–789.

[68] Y. Zhao, D. G. Truhlar, *Theor. Chem. Acc.* **2008**, *120*, 215–241.

[69] T. Yanai, D. P. Tew, N. C. Handy, *Chem. Phys. Lett.* **2004**, *393*, 51–57.

[70] A. V. Arbuznikov, M. Kaupp, *J. Chem. Phys.* **2014**, *141*, 204101.

[71] D. F. Aycock, *Org. Process Res. Dev.* **2007**, *11*, 156–159.

[72] Q. M. Phung, C. Martín-Fernández, J. N. Harvey, M. Feldt, *J. Chem. Theory Comput.* **2019**, *15*, 4297–4304.

[73] A. S. Petit, R. C. R. Pennifold, J. N. Harvey, *Inorg. Chem.* **2014**, *53*, 6473–6481.

[74] J. N. Harvey, M. Aschi, *Faraday Discuss.* **2003**, *124*, 129–143.

[75] F. Weigend, R. Ahlrichs, *Phys. Chem. Chem. Phys.* **2005**, *7*, 3297–3305.

[76] G. Li Manni, R. K. Carlson, S. Luo, D. Ma, J. Olsen, D. G. Truhlar, L. Gagliardi, *J. Chem. Theory Comput.* **2014**, *10*, 3669–3680.

[77] R. K. Carlson, D. G. Truhlar, L. Gagliardi, *J. Chem. Theory Comput.* **2015**, *11*, 4077–4085.

[78] K. Ruedenberg, M. W. Schmidt, M. M. Gilbert, S. T. Elbert, *Chem. Phys.* **1982**, *71*, 41–49.

[79] B. O. Roos, in *Adv. in Chem. Phys: Vol 69* (Eds.: K. P. Lawley), John Willy & Sons, Ltd., **1987**, pp 399–445.

[80] K. R. Shamasundar, G. Knizia, H. J. Werner, *J. Chem. Phys.* **2011**, *135*, 054101.

[81] P.-O. Widmark, P.-Å. Malmqvist, B. O. Roos, *Theor. Chim. Acta* **1990**, *77*, 291–306.

[82] B. O. Roos, R. Lindh, P.-Å. Malmqvist, V. Veryazov, P.-O. Widmark, *J. Phys. Chem. A* **2004**, *108*, 2851–2858.

[83] B. O. Roos, R. Lindh, P.-Å. Malmqvist, V. Veryazov, P.-O. Widmark, *J. Phys. Chem. A* **2005**, *109*, 6575–6579.

[84] M. Douglas, N. M. Kroll, *Ann. Phys.* **1974**, *82*, 89–155.

[85] B. A. Hess, *Phys. Rev. A* **1986**, *33*, 3742–3748.

[86] G. Jansen, B. A. Hess, *Phys. Rev. A Gen. Phys.* **1989**, *39*, 6016–6017.

[87] F. Aquilante, J. Autschbach, R. K. Carlson, L. F. Chibotaru, M. G. Delcey, L. De Vico, I. Fdez Galván, N. Ferré, L. M. Frutos, L. Gagliardi, M. Garavelli, A. Giussani, C. E. Hoyer, G. Li Manni, H. Lischka, D. Ma, P. Malmqvist, T. Müller, A. Nenov, M. Olivucci, T. B. Pedersen, D. Peng, F. Plasser, B. Pritchard, M. Reiher, I. Rivalta, I. Schapiro, J. Segarra-Martí, M. Stenrup, D. G. Truhlar, L. Ungur, A. Valentini, S. Vancoillie, V. Veryazov, V. P. Vysotskiy, O. Weingart, F. Zapata, R. Lindh, *J. Comput. Chem.* **2016**, *37*, 506–541.

[88] H.-J. Werner, P. J. Knowles, G. Knizia, F. R. Manby, M. Schütz, *Wiley Interdisc. Rev.: Comput. Mol. Sci.* **2012**, *2*, 242–253.

[89] S. Grimme, *Eur. J. Chem.* **2012**, *18*, 9955–9964.

[90] F. Eckert, A. Klamt, L. Koch, S. Terzi, 19.0.0 (Revision 5239) ed., COSMOlogic GmbH & Co. KG **1999–2018**, p. http://www.cosmologic.de.

[91] J. D. Head, *Int. J. Quantum Chem.* **1997**, *65*, 827–838.

[92] P. Å. Malmqvist, K. Pierloot, A. R. M. Shahi, C. J. Cramer, L. Gagliardi, *J. Chem. Phys.* **2008**, *128*, 204109.

[93] M. F. Rode, H. J. Werner, *Theor. Chem. Acc.* **2005**, *114*, 309–317.

[94] B. F. Gherman, C. J. Cramer, *Coord. Chem. Rev.* **2009**, *253*, 723–753.

[95] M. Radoń, *Phys. Chem. Chem. Phys.* **2019**, *21*, 4854–4870.

[96] M. Radoń, in *Adv. Inorg. Chem., Vol. 73* (Eds.: R. van Eldik, R. Puchta), Academic Press **2019**, pp. 221–264.

[97] G. Drabik, J. Szklarzewicz, M. Radoń, *Phys. Chem. Chem. Phys.* **2021**, *23*, 151–172.

[98] Q. M. Phung, M. Feldt, J. N. Harvey, K. Pierloot, *J. Chem. Theory Comput.* **2018**, *14*, 2446–2455.

RESEARCH ARTICLE
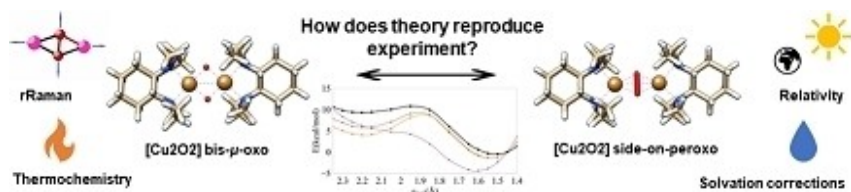
A. Stańczak, J. Chalupský*, L. Rulíšek*, M. Straka*

1 – 16

Comprehensive Theoretical View of the [Cu₂O₂] Side-on-Peroxo-/ Bis-μ-Oxo Equilibria

The "enigmatic" [Cu$_2$O$_2$] peroxo- vs. bis-μ-oxo equilibrium is explored herein. This includes analyzing various physical contributions, such as relativity and solvent effects; and calibrating the performance of wave-function and DFT methods for predicting accurate thermodynamics, vibrational spectra, and structures. Most of the computed data are benchmarked against the reference experimental values.

Paper II:
Evidence for H-bonding interactions to the
μ-η^2:η^2-peroxide of oxy-tyrosinase that activate
its coupled binuclear copper site

Check for updates

Evidence for H-bonding interactions to the μ-η²:η²-peroxide of oxy-tyrosinase that activate its coupled binuclear copper site†

Ioannis Kipouros, [ID] ‡[a] Agnieszka Stańczak, [ID] ‡[bc] Martin Culka,[b] Erik Andris, [ID] [b] Timothy R. Machonkin,[d] Lubomír Rulíšek [ID] *[b] and Edward I. Solomon [ID] *[ae]

The factors that control the diverse reactivity of the μ-η²:η²-peroxo dicopper(II) oxy-intermediates in the coupled binuclear copper proteins remain elusive. Here, spectroscopic and computational methods reveal H-bonding interactions between active-site waters and the μ-η²:η²-peroxide of oxy-tyrosinase, and define their effects on the Cu(II)₂O₂ electronic structure and O₂ activation.

The broad family of coupled binuclear copper (CBC) metalloproteins includes hemocyanins (Hc), catechol oxidases (CaOx), tyrosinases (Ty), and NspF, all of which contain two copper centers, each coordinated by three histidine residues, and held in close proximity to each other (3.5–4.0 Å).[1] In their reduced bicuprous deoxy state, these active sites bind dioxygen reversibly and with great affinity (K_d < 16–40 μM) to form a μ-η²:η²-peroxo dicopper(II) oxy-intermediate.[1,2] Crystallographic and X-ray spectroscopic investigations into the structure of these oxy-intermediates in different CBC members reveal a broadly conserved μ-η²:η²-peroxo dicopper(II) active site.[3–6] Similarly, all oxy-CBC proteins exhibit equivalent spectroscopic features, including (i) two distinct electronic absorption bands ($\varepsilon_{345nm} \sim$ 14 000–20 000 M^{-1} cm^{-1}, $\varepsilon_{600nm} \sim$ 1000 M^{-1} cm^{-1}) corresponding to two peroxide → Cu(II) charge-transfer (CT) transitions, (ii) a set of characteristic resonance Raman (rR) features corresponding to vibrational modes of the $[Cu(II)_2O_2]^{2+}$ cofactor (Fig. 1), and (iii) the absence of an electron paramagnetic resonance (EPR) signal due to the strong antiferromagnetic coupling between the two Cu(II) centers facilitated by the μ-η²:η²-peroxo superexchange pathway.[1,7,8] Despite these apparent similarities in the geometric and electronic structure of their $[Cu(II)_2O_2]^{2+}$ active sites, oxy-CBC proteins exhibit distinct reactivities that facilitate diverse physiological functions. The extracellular O₂-carrier protein Hc contains an extended terminal domain that prevents phenolic substrates from accessing its Cu(II)₂O₂ active site, thus lacking any enzymatic reactivity.[9] Unlike Hc, CaOx catalyze the oxidation of catechols to *o*-quinones, and are found predominantly as part of natural product biosynthesis pathways and defense mechanisms in plants. The ubiquitous Ty possesses both catechol oxidation and monophenol monooxygenation reactivities, and catalyzes the conversion of L-tyrosine to L-DOPAquinone, which constitutes the rate-limiting step in melanin biosynthesis in a variety of organisms from soil bacteria to humans. Finally, in addition to catechol oxidation and monophenol monooxygenation, NspF also catalyzes the monooxygenation of *o*-aminophenols to *o*-nitrosophenols in bacterial siderophore biosynthesis.[10]

Given the major implications of CBC proteins in both human diseases[11] and critical applications in agriculture (fruit browning[12]) and biotechnology (protein bioconjugation[13]), obtaining a mechanistic understanding of their diverse reactivities has been a major goal with broad scientific interest. However, putative differences in the electronic/geometric structures of their Cu(II)₂O₂ active sites as well as the molecular-level factors that control their reactivity are not fully understood despite extensive research efforts.[8,14–16] Second-sphere interactions involving active-site residues and/or solvent molecules with the Cu(II)₂O₂ core could have important mechanistic implications, but have been challenging to define experimentally, in part, due to the fact that most of the structural insights for catalytic oxy-CBC enzymes have derived from crystallographic studies on their latent pro-forms (PDB : 6JUA-D)[17] or binary complexes with their caddie proteins (PDB : 1WX2, 1WX4-5),[4] where in all cases the Ty active sites are occupied by additional residues, paralleling oxy-Hc (Fig. S4, ESI†). Here,

[a] *Department of Chemistry, Stanford University, Stanford, California 94305, USA. E-mail: edward.solomon@stanford.edu*

[b] *Institute of Organic Chemistry and Biochemistry of the Czech Academy of Sciences, Flemingovo náměstí 2, 166 10, Praha 6, Czech Republic. E-mail: lubos@uochb.cas.cz*

[c] *Faculty of Science, Charles University, Albertov 2038/6, 128 00 Praha 2, Czech Republic*

[d] *Department of Chemistry, Whitman College, Walla Walla, WA 99362, USA*

[e] *Stanford Synchrotron Radiation Lightsource, SLAC National Accelerator Laboratory, Stanford University, Menlo Park, California 94025, USA*

‡ These authors contributed equally.

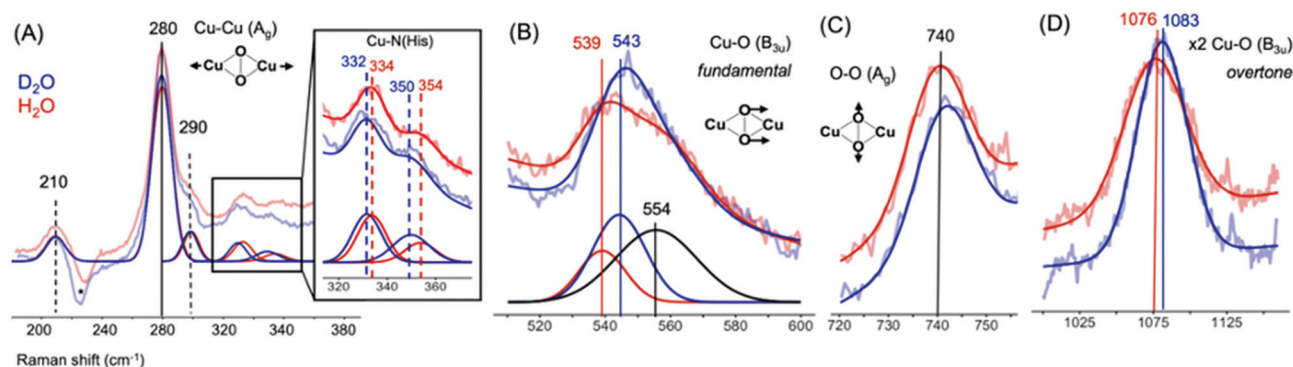**Fig. 1** Resonance Raman (351 nm laser excitation) spectral regions for the key $[Cu_{(II)2}O_2]^{2+}$ vibrational modes of oxy-Ty from *S. Glaucescens* (0.75 mM, 0.1 M CHES, pH/D 9.0) in H_2O (red) and D_2O (blue) corrected for background contributions, with Gaussian fits (in regions with multiple peaks, fits without the baseline components are also shown), and each region scaled for clarity (reference normalized peak intensity ratios are ~16 : 1 : 2 : 6 for Cu–Cu : Cu–O fundamental : O–O : Cu–O overtone), (A) the Cu–Cu (indicated with solid line) and Cu–N stretches (dashed lines), the negative feature (asterisk) at the solvent ice peak region results from background correction; the insert expands the region of the two higher-energy isotope-sensitive Cu–N stretches, (B) the Cu–O (B_{3u}) fundamental stretch (the black Gaussian indicates a non-isotope sensitive peak present in both solvents), (C) the O–O stretch, and (D) the Cu–O (B_{3u}) overtone stretch. For entire rR spectra before and after background corrections and for band-shape discussion see Fig. S5 (ESI†).

we have been able to directly probe and define previously unknown interactions between active-site water molecules and the μ-η^2:η^2-peroxide of the $[Cu_{(II)2}O_2]^{2+}$ active-site in the monomeric and fully-catalytic oxy-Ty from *Streptomyces glaucescens* by employing rR spectroscopy in tandem with solvent isotopic (H_2O/D_2O) perturbations, and correlating these experimental results to molecular dynamics (MD) simulations coupled with quantum-mechanics/molecular-mechanics (QM/MM) calculations. Comparison of the active sites of different CBC enzymes reveals variations in the key second-sphere residues that facilitate these H-bonding interactions in oxy-Ty, and correlate with the monooxygenation reactivity within this protein family.

By generating the oxy-Ty intermediate at high concentration and high purity in both H_2O and D_2O solvents (ESI,† Methods 1.1.5) we were able to obtain high-quality spectroscopic data. Upon laser excitation of the intense peroxide → Cu(II) CT transition at 351 nm, the rR spectrum of oxy-Ty in H_2O exhibits the characteristic resonance-enhanced vibrational modes of the μ-η^2:η^2-peroxo dicopper(II) core, previously defined for oxy-CBC proteins.[18,19] These include (i) the intense Cu–Cu (A_g) stretch at ~280 cm^{-1}, (ii) the O–O (A_g) stretch at ~740 cm^{-1}, (iii) the weak Cu–O (B_{3u}) stretch, which is non-totally symmetric, formally forbidden in rR, at ~540 cm^{-1} along with its intense symmetry-allowed first-overtone at ~1075 cm^{-1}, and (iv) four of the six Cu–N(His) modes in the 200–350 cm^{-1} region (Fig. 1). Upon solvent deuteration, the Cu–O (B_{3u}) overtone frequency increases by 6 ± 2 cm^{-1}, with its corresponding fundamental mode increasing by 4 ± 2 cm^{-1} (Fig. 1D and B, respectively), the two higher-energy Cu–N(His) stretches decrease by 2 ± 1 cm^{-1} and 4 ± 2 cm^{-1}, respectively (Fig. 1A inset), while the remaining modes, including the Cu–Cu and O–O stretches, are not perturbed (Fig. 1A and C). Paralleling the two higher-energy Cu–N(His) stretches in oxy-Ty, the H_2O → D_2O perturbations of the rR spectrum of oxy-Hc also exhibit a 1–2 cm^{-1} decrease in these two modes, which was attributed to the mass increase of

the deuterated imidazole rings of the histidine ligands.[20] However, unlike oxy-Ty, no solvent isotopic (H_2O/D_2O) perturbations were observed for the Cu–O (B_{3u}) fundamental or overtone modes in the rR spectrum of oxy-Hc.[20] Since solvent accessibility is among the most prominent active-site differences between oxy-Hc and the monomeric active oxy-Ty,[1,21] the presence of direct interactions between the $[Cu_{(II)2}O_2]^{2+}$ core and water molecules is likely responsible for the observed H_2O → D_2O upshift of the Cu–O (B_{3u}) frequency. Such rR H_2O → D_2O upshifts of metal–oxo stretches have been observed in binuclear iron metalloenzymes, including oxy-hemerythrin and met-ribonucleotide reductase.[22,23] In both cases, the frequency increase of the symmetric Fe–O–Fe stretch upon solvent deuteration was attributed to H-bonding interactions between the oxo-bridge and the respective metal-coordinated hydroperoxo or water-derived hydroxyl ligands. However, these correlations between the presence of H-bonding interactions and the H_2O → D_2O frequency increase of metal–oxo stretches remain empirical, lacking an analysis of their molecular origin.

To fully define these H-bonding interactions between the $[Cu_{(II)2}O_2]^{2+}$ core and water molecule(s), as well as to elucidate the origin of the Cu–O (B_{3u}) H_2O → D_2O upshift, our spectroscopic results were correlated with a combination of computational methods. First, from the crystal structure of oxy-Ty from *Streptomyces castaneoglobisporous* (PDB : 1WX2) we generated a fully solvated protein model of the monomeric oxy-Ty (Fig. 2A and ESI,† Fig. S6 and Methods 1.2.1–1.2.3) and performed 0.5 μs MD simulations (ESI,† Video S1, and Methods 1.2.4). Our MD simulations clearly demonstrate three distinct positions in the active site of oxy-Ty that are occupied by water molecules (Fig. S7B, ESI†). One of these waters (W3) has been previously observed crystallographically and was proposed to act as the acceptor of the monophenolic proton during the monooxygenation reaction.[24] The other two water molecules (W1, W2), which have not been previously observed, reside above the Cu_2O_2 plane and each of them forms an H-bond with
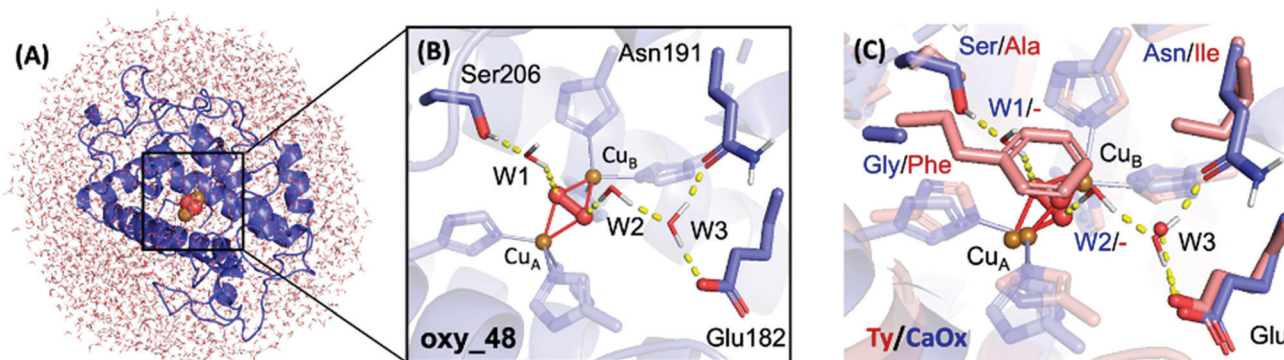
Fig. 2 (A) The full-length QM/MM-optimized structure for the experimentally-calibrated oxy-Ty active site from *Streptomyces castaneoglobisporous* (oxy_48, blue), (B) its active site, and (C) its alignment with the met-CaOx from *Ipomoea batatas* (PDB : 1BT1, red). Key second-sphere residues and the μ-η²:η²-peroxide ligand and waters (W1–3) in oxy-Ty are shown as solid sticks, the water (W3) and μ-hydroxide ligand in CaOx as red spheres, the first-sphere histidines as transparent sticks, the copper centers as brown spheres, and H-bonds as dashed yellow lines.

one of the O atoms of the μ-η²:η²-peroxide. H-bonding to the μ-η²:η²-peroxide represents a new type of interaction, not previously defined in other CBC enzymes or synthetic $[Cu(II)_2O_2]^{2+}$ model complexes.

We next generated 64 distinct QM/MM-optimized oxy-Ty structures with different numbers (2–8) and conformations of active-site waters (initial structures were obtained from MD simulations or generated manually; ESI,† Methods 1.2.5–1.2.10 and Table S2). The optimal number of active-site waters in oxy-Ty was determined by systematically evaluating the thermodynamic stability of oxy-Ty at different hydration levels (ESI,† Methods 1.2.11, 1.2.12 and Table S1). Our calculations indicate that the most thermodynamically favorable QM/MM-optimized oxy-Ty structure (oxy_48) has four water molecules occupying its active site, including W1–3, with W1 and W2 H-bonding to the μ-η²:η²-peroxide (Fig. 2B).

To evaluate the contributions of these H-bonding interactions to the $H_2O \rightarrow D_2O$ frequency changes in the vibrational modes in oxy-Ty, we calculated the vibrational frequencies for oxy_48 and correlated them to our rR data (ESI,† Methods 1.2.13–1.2.15). Our calculations show that oxy_48 closely reproduces the $H_2O \rightarrow D_2O$ frequency perturbations ($\Delta\nu$[Cu–Cu] = −1 cm^{-1}, $\Delta\nu$[Cu–O (B$_{3u}$)] = +10 cm^{-1}, $\Delta\nu$[O–O] = +1 cm^{-1}), observed by rR ($\Delta\nu$[Cu–Cu] < ±2 cm^{-1}, $\Delta\nu$[Cu–O (B$_{3u}$)] = +4 ± 2 cm^{-1}, $\Delta\nu$[O–O] < ±2 cm^{-1}; Fig. 1). As a control, a less thermodynamically stable QM/MM-optimized structure (oxy_59 in Fig. S9, ESI†) that lacks W1 and

W2, does not reproduce our rR results, as it does not exhibit any isotopic perturbation of its Cu–O (B$_{3u}$) mode (Table S1, ESI†).

Our QM frequency calculations also reveal the underlying molecular mechanism for the Cu–O (B$_{3u}$) $H_2O \rightarrow D_2O$ upshift. Both W1 and W2 have two related vibrational modes, a twisting and a higher-energy rocking mode, which are present in the 450–650 cm^{-1} region in H_2O, above the Cu–O (B$_{3u}$) mode energy calculated at 425 cm^{-1},§ while upon solvent deuteration, both of these water modes decrease in energy by ~150–200 cm^{-1} and are now below the Cu–O (B$_{3u}$) mode (ESI,† Methods 1.2.16). Consequently, in H_2O, the energy of the Cu–O (B$_{3u}$) mode is decreased due to its mixing with the nearby higher-energy water twisting mode (Fig. 3, left), while in D_2O, the Cu–O (B$_{3u}$) energy is now increased due to its mixing with the nearby lower-energy water rocking mode (Fig. 3, right). Thus, the combined effect of the Cu–O (B$_{3u}$) frequency decrease in H_2O and increase in D_2O *via* this mode-mixing mechanism results to the experimentally observed and computationally reproduced Cu–O (B$_{3u}$) $H_2O \rightarrow D_2O$ upshift.¶ This mode mixing mechanism establishes a molecular-level foundation for this solvent isotope-dependent rR ν(metal–oxygen) increase, which has been routinely employed to identify H-bonds to metal/oxygen active sites in other enzymes,[22,23] and extends it beyond empirical identification and towards obtaining insights into electronic structure changes induced by H-bonding.

Previous structure/function investigations into the CBC family indicated that unlike plant CaOx, Ty lacks a bulky gatekeeper phenylalanine and contains a conserved Asn/Glu cluster (Fig. 2C), however the functional significance of these second-sphere correlations remains a subject of debate.[14,16,21,25–27] Inspection of our experimentally-calibrated structure of the oxy-Ty active site reveals that these key second-sphere residues are critical in allowing solvent access to the active site and stabilizing W2, and thus enable the H-bonding to the μ-η²:η²-peroxide (Fig. 2B). Although further experimental studies are required to establish the catalytic significance of these second-sphere residues, our QM/MM calculations on oxy-Ty reveal that H-bonding of W1 and W2 to the μ-η²:η²-peroxide weakens its O–O bond strength (Fig. S11, ESI†). Indeed, H-bonds to the μ-η²:η²-peroxide are expected to stabilize its σ* lowest unoccupied molecular orbital, which would increase the back-bonding
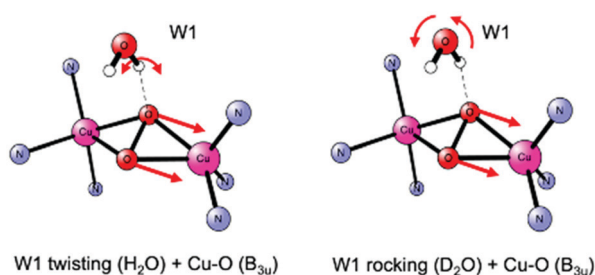

Fig. 3 Vibrational coupling of the Cu–O (B$_{3u}$) mode of the Cu(II)$_2$O$_2$ active site with two key W1 modes (twisting in H_2O and rocking in D_2O).

donation from the Cu(II) d orbitals, resulting in weakening of the O–O bond.[28] This H-bonding perturbation of the O–O bond further correlates to previous reports where introduction of H-bond donor groups into the ligand scaffold of a μ-η^2:η^2-peroxo dicopper(II) complex promotes O–O bond cleavage and conversion to its bis-μ-oxo dicopper(III) isomer.[29] While such intramolecular H-bonding has been found to enhance both the H-atom abstraction reactivity of η^1-superoxo monocupric model complexes,[30] and the ammine oxidation reactivity of the η^1-hydroperoxo monocupric active site of an artificial metalloenzyme,[31] the relevance of intra- or intermolecular H-bonding on the monophenol monooxygenation and catechol oxidation reactivities of μ-η^2:η^2-peroxo dicopper(II) complexes has not been investigated.

In conclusion, our spectroscopic and computational investigations define a previously elusive H-bonding network within the oxy-Ty active site, where water molecules (W1–3) form H-bonds with the μ-η^2:η^2-peroxide and conserved second-sphere residues (Fig. 2B). These key second-sphere residues vary within the CBC protein family, and likely affect the H-bonding interactions to the μ-η^2:η^2-peroxide in their respective oxy-intermediates. This study opens the way for further investigations into H-bonding interactions to the μ-η^2:η^2-peroxide of $[Cu(II)_2O_2]^{2+}$ biological active sites and their model complexes, as well as determination of their mechanistic implications on O_2 activation, mono/diphenol substrate binding, and their subsequent reactivity.

Conflicts of interest

There are no conflicts to declare.

Notes and references

§ The unmixed frequency of the Cu–O (B_{3u}) mode was calculated from structure oxy_59 (Fig. S9, ESI†) which lacks both W1 and W2.

¶ While the Cu–O (B_{3u}) mode is generally calculated to be functional dependent,[32] and lower in energy than experimentally observed, the above model only requires that the Cu–O (B_{3u}) mode remains between the energies of the water modes in H_2O versus D_2O. Note also, that although the extent of vibrational coupling between the twisting/rocking modes and the Cu–O (B_{3u}) stretch varies among our oxy-Ty structures due to small differences in the strength and directionality of their corresponding H-bonds between W1/W2 and the μ-η^2:η^2-peroxide, this mode mixing mechanism operates throughout to generate the $H_2O \rightarrow D_2O$ Cu–O (B_{3u}) energy upshifts (Fig. S8, ESI†).

1 E. I. Solomon, D. E. Heppner, E. M. Johnston, J. W. Ginsbach, J. Cirera, M. Qayyum, M. T. Kieber-Emmons, C. H. Kjaergaard, R. G. Hadt and L. Tian, *Chem. Rev.*, 2014, **114**, 3659–3853.
2 S. Hirota, T. Kawahara, E. Lonardi, E. de Waal, N. Funasaki and G. W. Canters, *J. Am. Chem. Soc.*, 2005, **127**, 17966–17967.
3 K. A. Magnus, B. Hazes, H. Ton-That, C. Bonaventura, J. Bonaventura and W. G. J. Hol, *Proteins*, 1994, **19**, 302–309.

4 Y. Matoba, T. Kumagai, A. Yamamoto, H. Yoshitsu and M. Sugiyama, *J. Biol. Chem.*, 2006, **281**, 8981–8990.
5 J. M. Brown, L. Powers, B. Kincaid, J. A. Larrabee and T. G. Spiro, *J. Am. Chem. Soc.*, 1980, **102**, 4210–4216.
6 G. L. Woolery, L. Powers, M. Winkler, E. I. Solomon, K. Lerch and T. G. Spiro, *Biochim. Biophys. Acta, Protein Struct. Mol. Enzymol.*, 1984, **788**, 155–161.
7 K. Lerch and L. Ettlinger, *Eur. J. Biochem.*, 1972, **31**, 427–437.
8 J. W. Ginsbach, M. T. Kieber-Emmons, R. Nomoto, A. Noguchi, Y. Ohnishi and E. I. Solomon, *Proc. Natl. Acad. Sci. U. S. A.*, 2012, **109**, 10793–10797.
9 C. Morioka, Y. Tachi, S. Suzuki and S. Itoh, *J. Am. Chem. Soc.*, 2006, **128**, 6788–6789.
10 A. Noguchi, T. Kitamura, H. Onaka, S. Horinouchi and Y. Ohnishi, *Nat. Chem. Biol.*, 2010, **6**, 641–643.
11 I. Carballo-Carbajal, A. Laguna, J. Romero-Giménez, T. Cuadros, J. Bové, M. Martinez-Vicente, A. Parent, M. Gonzalez-Sepulveda, N. Peñuelas, A. Torra, B. Rodríguez-Galván, A. Ballabio, T. Hasegawa, A. Bortolozzi, E. Gelpi and M. Vila, *Nat. Commun.*, 2019, **10**, 973.
12 F. Tinello and A. Lante, *Innovative Food Sci. Emerging Technol.*, 2018, **50**, 73–83.
13 C. S. Mogilevsky, M. J. Lobba, D. D. Brauer, A. M. Marmelstein, J. C. Maza, J. M. Gleason, J. A. Doudna and M. B. Francis, *J. Am. Chem. Soc.*, 2021, **143**, 13538–13547.
14 S. M. Prexler, M. Frassek, B. M. Moerschbacher and M. E. Dirks-Hofmeister, *Angew. Chem., Int. Ed.*, 2019, **58**, 8757–8761.
15 H. Decker, T. Schweikardt and F. Tuczek, *Angew. Chem., Int. Ed.*, 2006, **45**, 4546–4550.
16 I. Kampatsikas and A. Rompel, *ChemBioChem*, 2021, **22**, 1161–1175.
17 N. Fujieda, K. Umakoshi, Y. Ochi, Y. Nishikawa, S. Yanagisawa, M. Kubo, G. Kurisu and S. Itoh, *Angew. Chem., Int. Ed.*, 2020, **59**, 13385–13390.
18 J. A. Larrabee, T. G. Spiro, N. S. Ferris, W. H. Woodruff, W. A. Maltese and M. S. Kerr, *J. Am. Chem. Soc.*, 1977, **99**, 1979–1980.
19 N. C. Eickman, E. I. Solomon, J. A. Larrabee, T. G. Spiro and K. Lerch, *J. Am. Chem. Soc.*, 1978, **100**, 6529–6531.
20 J. Ling, L. P. Nestor, R. S. Czernuszewicz, T. G. Spiro, R. Fraczkiewicz, K. D. Sharma, T. M. Loehr and J. Sanders-Loehr, *J. Am. Chem. Soc.*, 1994, **116**, 7682–7691.
21 H. Decker, T. Schweikardt, D. Nillius, U. Salzbrunn, E. Jaenicke and F. Tuczek, *Gene*, 2007, **398**, 183–191.
22 A. K. Shiemke, T. M. Loehr and J. Sanders-Loehr, *J. Am. Chem. Soc.*, 1986, **108**, 2437–2443.
23 B. M. Sjoeberg, J. Sanders-Loehr and T. M. Loehr, *Biochemistry*, 1987, **26**, 4242–4247.
24 M. Goldfeder, M. Kanteev, S. Isaschar-Ovdat, N. Adir and A. Fishman, *Nat. Commun.*, 2014, **5**, 4505.
25 A. Bijelic, M. Pretzler, C. Molitor, F. Zekiri and A. Rompel, *Angew. Chem., Int. Ed.*, 2015, **54**, 14677–14680.
26 M. Kanteev, M. Goldfeder and A. Fishman, *Protein Sci.*, 2015, **24**, 1360–1369.
27 M. E. Dirks-Hofmeister, R. Singh, C. M. Leufken, J. K. Inlow and B. M. Moerschbacher, *PLoS One*, 2014, **9**, e99759.
28 G. Y. Park, M. F. Qayyum, J. Woertink, K. O. Hodgson, B. Hedman, A. A. Narducci Sarjeant, E. I. Solomon and K. D. Karlin, *J. Am. Chem. Soc.*, 2012, **134**, 8513–8524.
29 H.-C. Liang, C. X. Zhang, M. J. Henson, R. D. Sommer, K. R. Hatwell, S. Kaderli, A. D. Zuberbühler, A. L. Rheingold, E. I. Solomon and K. D. Karlin, *J. Am. Chem. Soc.*, 2002, **124**, 4170–4171.
30 D. E. Diaz, D. A. Quist, A. E. Herzog, A. W. Schaefer, I. Kipouros, M. Bhadra, E. I. Solomon and K. D. Karlin, *Angew. Chem.*, 2019, **131**, 17736–17740.
31 S. I. Mann, T. Heinisch, T. R. Ward and A. S. Borovik, *J. Am. Chem. Soc.*, 2017, **139**, 17289–17292.
32 M. F. Qayyum, R. Sarangi, K. Fujisawa, T. D. P. Stack, K. D. Karlin, K. O. Hodgson, B. Hedman and E. I. Solomon, *J. Am. Chem. Soc.*, 2013, **135**, 17417–17431.

Paper III:
Elucidation of the tyrosinase/O_2/monophenol ternary intermediate that dictates the monooxygenation mechanism in melanin biosynthesis

Elucidation of the tyrosinase/O₂/monophenol ternary intermediate that dictates the monooxygenation mechanism in melanin biosynthesis

Ioannis Kipouros[a] , Agnieszka Stańczak[b,c] , Jake W. Ginsbach[a], Prokopis C. Andrikopoulos[b,1] , Lubomír Rulíšek[b,2] , and Edward I. Solomon[a,d,2]

Melanins are highly conjugated biopolymer pigments that provide photoprotection in a wide array of organisms, from bacteria to humans. The rate-limiting step in melanin biosynthesis, which is the *ortho*-hydroxylation of the amino acid L-tyrosine to L-DOPA, is catalyzed by the ubiquitous enzyme tyrosinase (Ty). Ty contains a coupled binuclear copper active site that binds O_2 to form a $\mu{:}\eta^2{:}\eta^2$-peroxide dicopper(II) intermediate (oxy-Ty), capable of performing the regioselective monooxygenation of *para*-substituted monophenols to catechols. The mechanism of this critical monooxygenation reaction remains poorly understood despite extensive efforts. In this study, we have employed a combination of spectroscopic, kinetic, and computational methods to trap and characterize the elusive catalytic ternary intermediate (Ty/O₂/monophenol) under single-turnover conditions and obtain molecular-level mechanistic insights into its monooxygenation reactivity. Our experimental results, coupled with quantum-mechanics/molecular-mechanics calculations, reveal that the monophenol substrate docks in the active-site pocket of oxy-Ty fully protonated, without coordination to a copper or cleavage of the $\mu{:}\eta^2{:}\eta^2$-peroxide O-O bond. Formation of this ternary intermediate involves the displacement of active-site water molecules by the substrate and replacement of their H bonds to the $\mu{:}\eta^2{:}\eta^2$-peroxide by a single H bond from the substrate hydroxyl group. This H-bonding interaction in the ternary intermediate enables the unprecedented monooxygenation mechanism, where the $\mu{-}\eta^2{:}\eta^2$-peroxide O-O bond is cleaved to accept the phenolic proton, followed by substrate phenolate coordination to a copper site concomitant with its aromatic *ortho*-hydroxylation by the non-protonated μ-oxo. This study provides insights into O_2 activation and reactivity by coupled binuclear copper active sites with fundamental implications in biocatalysis.

tyrosinase | binuclear copper | monooxygenase | oxygen activation | melanin biosynthesis

Biological pigmentation via the biosynthesis of small molecules and polymers is a widespread evolutionary adaptation found in a range of different environments (1). Melanins, a major class of highly conjugated biopolymer pigments, are essential for a diverse group of organisms, from soil bacteria to humans, due to their photoprotective, antioxidant, and metal-sequestering properties (2). The initial and rate-limiting step (RLS) in the biosynthesis of most melanins during melanogenesis, which is the O_2-dependent *ortho*-hydroxylation of the amino acid L-tyrosine to L-3,4-dihydroxyphenylalanine (L-DOPA), as well as the subsequent two-electron oxidation of L-DOPA to L-DOPAquinone (Fig. 1*A*), are both catalyzed by the same ubiquitous enzyme tyrosinase (Ty) (3). Due to its key catalytic role in both microbial and mammalian melanogenesis, Ty has become an emerging therapeutic target for the treatment of bacterial and fungal infections (4), as well as for the early detection, prevention, and treatment of complex human diseases, including skin cancer (5, 6) and Parkinson's disease (7, 8). The direct link between melanogenesis and fruit browning has also made plant Ty, as well as the phylogenetically related catechol oxidases (CaOxs), critical agrotechnological targets toward improving food quality and extending produce shelf life (9). Beyond its role in melanin biosynthesis, the high regioselectivity and broad substrate promiscuity toward the aromatic monooxygenation of a range of *para*-substituted monophenols has made Ty a promising enzymatic tool for a number of challenging chemical transformations and biotechnological applications, including protein bioconjugation (10), bioorthogonal chemistry (11), metabolite biosensors (12, 13), and bioremediation (14). However, advancements in these key areas and a fundamental molecular-level understanding of melanogenesis are limited by the lack of detailed mechanistic insights into the enzymatic monooxygenation reaction.

Previous crystallographic and spectroscopic studies have shown that the reactivity of Ty is afforded by its coupled binuclear copper (CBC) active site, where a conserved four-alpha-helix bundle brings two Cu ions, each coordinated by three histidine

Significance

Melanins are ubiquitous photoprotective biopolymer pigments with major implications ranging from fruit browning to severe human diseases, including skin cancer. Tyrosinase, the enzyme catalyzing the rate-limiting step in melanin biosynthesis is thus an important biotechnological and therapeutic target. Tyrosinase contains a coupled binuclear copper active site that binds dioxygen to form a $\mu{-}\eta^2{:}\eta^2$-peroxide dicopper(II) intermediate (oxy-tyrosinase) which is activated toward the regioselective aromatic monooxygenation of *para*-substituted monophenols via a poorly defined mechanism. Here, we have employed spectroscopic, kinetic, and computational methods to trap and characterize the elusive catalytic ternary intermediate formed upon monophenol binding to oxy-tyrosinase and elucidate the mechanism of the subsequent monooxygenation reaction. This study provides unprecedented molecular-level insights into the rate-limiting step in melanin biosynthesis.

[1]Present address: Institute of Biotechnology, Czech Academy of Sciences, 252 50 Vestec, Czech Republic.

[2]To whom correspondence may be addressed. Email: solomone@stanford.edu or lubomir.rulisek@uochb.cas.cz.
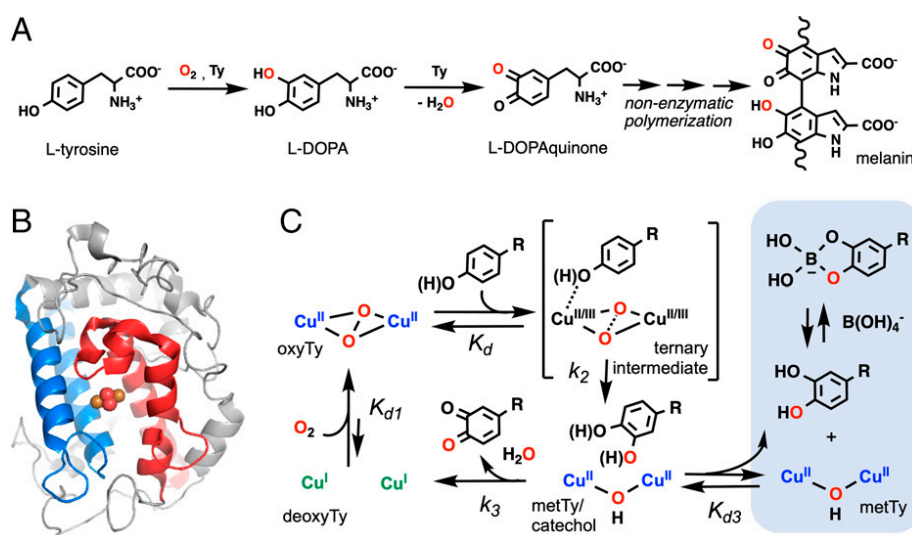
Fig. 1. (*A*) The rate-limiting monooxygenation step of L-tyrosine to L-DOPA and the subsequent oxidation of L-DOPA to L-DOPAquinone in melanin biosynthesis are both catalyzed by Ty. (*B*) Structure of oxy-Ty from *S. castaneoglobisporous* (PDB: 1WX2) (15), with the four-alpha-helix bundle shown in blue and red and each color corresponding to their respective coordination of Cu_A and Cu_B (Cu, brown spheres; μ-η^2:η^2-peroxide, red spheres). (*C*) Kinetic scheme for the catalytic cycle (monophenol monooxygenation and catechol oxidation reactions) of Ty toward *para*-substituted monophenols, with the effect of borate trapping the catechol product shown in the shaded region. The elusive ternary intermediate is shown in brackets. For the extended kinetic scheme, see *SI Appendix*, Scheme S1.

residues, in close proximity to each other (<5 Å; Fig. 1*B*) (3). During the catalytic cycle, the μ-hydroxo dicopper(II) active site of the resting enzyme (met-Ty) oxidizes catechols to *ortho*-quinones and is reduced to its dicopper(I) state (deoxy-Ty), which then reversibly binds molecular dioxygen to form a μ-η^2:η^2-peroxide dicopper(II) intermediate (oxy-Ty) that possesses both monophenol monooxygenation and catechol oxidation reactivities (Fig. 1*C*, unshaded region) (3). All catalytic forms of Ty are diamagnetic, which in the cases of met-Ty and oxy-Ty is due to the strong antiferromagnetic coupling of their two Cu(II) centers afforded by their bridging ligands (3). Similar to the oxy-intermediates of other CBC proteins, oxy-Ty exhibits distinct electronic absorption bands (ε_{345nm} ~16,000 cm^{-1} M^{-1}, ε_{650nm} ~1,000 cm^{-1} M^{-1}) and resonance Raman (rR) features (section 2.3), reflecting its unique electronic structure, where the strong donor interactions of the side-on peroxide with both Cu(II) centers result in its intense high-energy charge-transfer (CT) band (16), while the back-bonding interaction with the μ-η^2:η^2-peroxide is responsible for its relatively low O-O stretching frequency (~740 cm^{-1}) (17).

While oxy-Ty unambiguously has a μ-η^2:η^2-peroxide dicopper(II) active site (3), model complex studies have demonstrated that such species can be in an equilibrium with their bis-μ-oxo dicopper(III) electronic isomers (18), both of which are able to monooxygenate phenolates to their corresponding catechol products. In some reported cases, μ-η^2:η^2-peroxide $Cu^{II}_2O_2$ model complexes can directly monooxygenate aromatic substrates without substrate coordination (19), while in others, phenolate coordination to one of the Cu centers promotes the cleavage of the μ-η^2:η^2-peroxide O-O bond to form a bis-μ-oxo $Cu^{III}_2O_2$ core before substrate monooxygenation (20). The enzymatic monooxygenation reaction mechanism is similarly expected to be dictated by the geometric and electronic structure of the Cu_2O_2 core in the ternary (Ty/O$_2$/monophenol) intermediate, which is formed upon the binding of the monophenol or monophenolate substrate to the oxy-Ty active site. However, this ternary intermediate remains elusive, despite previous efforts (21). In addition, given that under the typical range of physiological conditions for melanin biosynthesis

(pH 4 to 7), the native substrate, L-tyrosine (pK_a = 10), is predominantly in its fully protonated monophenolic form (3), the protonation state of the substrate during its binding to oxy-Ty and the identity of the putative phenolic proton acceptor site in the ternary intermediate remain subjects of debate (22–26). Consequently, the lack of critical experimental evidence on the nature of the catalytic ternary intermediate of Ty significantly limits our mechanistic understanding of its monooxygenation reactivity toward monophenols.

In this study, we use a *para*-substituted monophenol substrate that exhibits both sufficient binding to oxy-Ty and slow subsequent monooxygenation to trap and spectroscopically (optical absorption and rR) characterize the catalytic ternary intermediate of Ty from *Streptomyces glaucescens* under single-turnover conditions and obtain key mechanistic insights into its subsequent monooxygenation reaction. Our experimental data, coupled with quantum-mechanics/molecular-mechanics (QM/MM) calculations, indicate that the monophenolic substrate binds to the active-site pocket of oxy-Ty fully protonated, without cleavage of the μ-η^2:η^2-peroxide O-O bond and without direct coordination to a Cu center. Formation of this ternary intermediate involves the displacement of the recently reported active-site water molecules (27), and replacement of their H-bonding interactions with the μ-η^2:η^2-peroxide by a single H bond from the hydroxyl group of the docked full-protonated monophenol substrate. This unprecedented substrate binding mode to a μ-η^2:η^2-peroxide dicopper(II) active site has direct mechanistic implications. Indeed, further investigations into the reactivity of this ternary intermediate reveal the key steps of the monooxygenation mechanism of Ty, where enabled by its H-bonding interaction with the substrate, the μ-η^2:η^2-peroxide O-O bond breaks to accept the phenolic $H^{+/\bullet}$. This step is followed by monophenolate substrate coordination to a Cu center concomitant with its aromatic *ortho*-hydroxylation by the nonprotonated μ-oxo. Overall, this study defines the mechanism of the critical monooxygenation reaction in melanin biosynthesis and provides a unifying mechanistic framework for the diverse Cu_2O_2 chemistry of model complexes and biological active sites.

2. Results and Analysis

2.1. Uncoupling the monophenol monooxygenation and catechol oxidation reactions.

In order to directly probe the monophenol monooxygenation reaction of oxy-Ty, we proceeded to uncouple it from its subsequent catechol oxidation reaction that completes the catalytic cycle. To this end, we employed a previously reported borate system (28), where the catechol product of the monooxygenation reaction dissociates from the met-Ty active site before its further oxidation to *ortho*-quinone and is trapped by its condensation-driven complexation with borate (Fig. 1*C*, shaded region). Under these conditions, and in the absence of any external reductants, the monooxygenation of monophenols by oxy-Ty would be converted into a single-turnover reaction. This approach was evaluated by monitoring the time course for the reaction of oxy-Ty with a series of *para*-substituted monophenols via measuring O_2 consumption (*SI Appendix, section 2.1.1*) and product formation (*SI Appendix, section 2.1.2*). The reactions of oxy-Ty with monophenols containing electron-donating *para* groups result in the consumption of multiple O_2 equivalents (*SI Appendix, Fig. S2 A–D*) and the generation of their respective quinone products (*SI Appendix, Fig. S4 A–D*), indicating that these are in fact multiple turnover reactions. However, the reactions of oxy-Ty with the two monophenols containing electron-withdrawing *para* groups, 4-hydroxybenzamide (4-CONH$_2$) and methyl 4-hydroxybenzoate (4-COOCH$_3$), result in neither the consumption of additional O_2 equivalents (*SI Appendix, Fig. S2 E and F*) nor the generation of their chromophoric quinone and further oxidation products, indicating that these are indeed single-turnover reactions (*SI Appendix, Fig. S4E* and Fig. 2*A*).

The above results indicate that the single-turnover efficiency of the borate-based kinetic scheme (Fig. 1*C*) is substrate dependent and can be rationalized in terms of distinct *para*-group effects. First, the inductive and resonance *para*-group effects dictate the two-electron reduction potential of the *para*-substituted quinone products, with more electron-withdrawing *para* groups slowing down the rate of catechol oxidation to *ortho*-quinone by met-Ty (k_3). Second, the binding affinity of the catechol product to the met-Ty active site is expected to vary with different *para* groups and thus affect the extent of catechol dissociation (K_{d3}). Finally, the competitive inhibition of the generated met-Ty by the high excess of the *para*-substituted monophenolic substrate (K$_{i1}$ in *SI Appendix, Scheme S1*) (29) is similarly expected to vary with *para* group and thus suppress multiple turnovers to different extents. Importantly, the reactions of oxy-Ty with the monophenols 4-CONH$_2$ and 4-COOCH$_3$ exhibit complete uncoupling of the timescales for their monooxygenation and catechol oxidation reactions, providing the opportunity to study the monooxygenation reaction of Ty under single-turnover conditions.

2.2. Formation and reactivity of the ternary intermediate.

To investigate the possible formation of the elusive ternary intermediate (Ty/O$_2$/monophenol), the single-turnover reaction of oxy-Ty with the 4-COOCH$_3$ substrate was monitored by stopped-flow absorption (SF-Abs) spectroscopy after mixing deoxy-Ty with increasing substrate concentrations in O$_2$-saturated borate buffer (parallel kinetic investigations for the 4-CONH$_2$ substrate yielded equivalent results; *SI Appendix, section 2.2.1*). For all 4-COOCH$_3$ concentrations, the instantaneous appearance of the two absorption bands at 345 and 650 nm, corresponding to the two characteristic peroxide→Cu(II) CT transitions of the µ-η^2:η^2-peroxide dicopper(II) active site, indicates fast and

exergonic O_2 binding in deoxy-Ty to form oxy-Ty. These absorption bands subsequently undergo first-order exponential decay at a rate accelerated with increasing substrate concentration and notably without the prior or concomitant formation of any absorption features (Fig. 2*A*). The rate constants (k_{obs}) obtained by fitting the decay of the 350-nm traces (Fig. 2*A*, insert) exhibit linear dependence at lower substrate concentrations and progressive saturation at increasing substrate concentrations (Fig. 2*B*). Under our single-turnover conditions, this nonlinear dependence of the k_{obs} values over increasing substrate concentration requires our kinetic scheme to include the ternary intermediate (Ty/O$_2$/4-COOCH$_3$) that forms via the fast and reversible binding of the monophenolic substrate to oxy-Ty (K_d = 13 mM; Fig. 1*C*) and decays via the slow and irreversible monooxygenation reaction to form the catechol product (k_2 = 0.56 s^{-1}; Fig. 1*C*). The fast and reversible binding (k_{on}) and dissociation (k_{off}) of the monophenolic substrate to oxy-Ty is supported by the substrate concentration-dependent saturation of k_{obs}, which requires $k_{on} \gg k_2$ and is confirmed by spectroscopic characterization of an early-time (100 ms) reaction mixture by rR spectroscopy (section 2.3). Note also that binding of the monophenol substrate to deoxy-Ty (29), which can slow or prevent subsequent binding of O_2, is found not to be significant for the 4-COOCH$_3$ substrate under the high postmixing O_2 concentrations (>1 mM) employed in our experiments (*SI Appendix, Fig. S8*).

Based on the obtained kinetic parameters for the formation (K_d) and decay (k_2) of the ternary intermediate, at early times (100 ms) and at the highest 4-COOCH$_3$ concentrations (10 mM postmixing, solubility limited), the ternary intermediate accumulates at ~43% of the total enzyme concentration. Using this early-time speciation, the UV-vis absorption spectrum of the ternary intermediate can be obtained from the 100-ms SF-Abs spectrum for the reaction of deoxy-Ty with an O$_2$-saturated solution of 4-COOCH$_3$ (10 mM), after correction for the spectral contributions from oxy-Ty and intensity renormalization. The resulting ultraviolet-to-visible (UV-vis) absorption spectrum for the ternary intermediate exhibits two absorption bands with energies and intensities similar to those corresponding to the two peroxide→Cu(II) CT transitions in oxy-Ty (Fig. 2*C*), indicating that the ternary intermediate also contains a similar µ-η^2:η^2-peroxide dicopper(II) active site. Note that unlike previous proposals from model complex studies (20), our results do not support the possibility of a substrate-coordinated bis-µ-oxo dicopper(III) active site in the ternary intermediate of Ty, as none of the characteristic absorption features for the oxo→Cu(III) and phenolate→Cu(III) CT transitions in the 350- to 550-nm region are observed (21, 30).

To determine the protonation state of the 4-COOCH$_3$ substrate (i.e., monophenol versus monophenolate) during the formation of the ternary intermediate, the pH dependence of its reaction with oxy-Ty was evaluated by SF-Abs kinetic experiments. Our results show that while k_2 is pH independent, the apparent K_d decreases with decreasing pH (*SI Appendix, Fig. S7A*), indicating that the monophenolic form of 4-COOCH$_3$ binds to oxy-Ty more favorably than its monophenolate form. Together, our above results clearly demonstrate that the ternary intermediate contains a µ-η^2:η^2-peroxide dicopper(II) core with the substrate bound at the active site as either 1) a monophenol or 2) a monophenolate with its phenolic proton accepted by an active-site base. Further insights into the identity of the proton acceptor site and the interactions between the bound substrate and the Cu(II)$_2$O$_2$ core in the ternary intermediate were obtained by higher-resolution spectroscopic investigations (section 2.3).
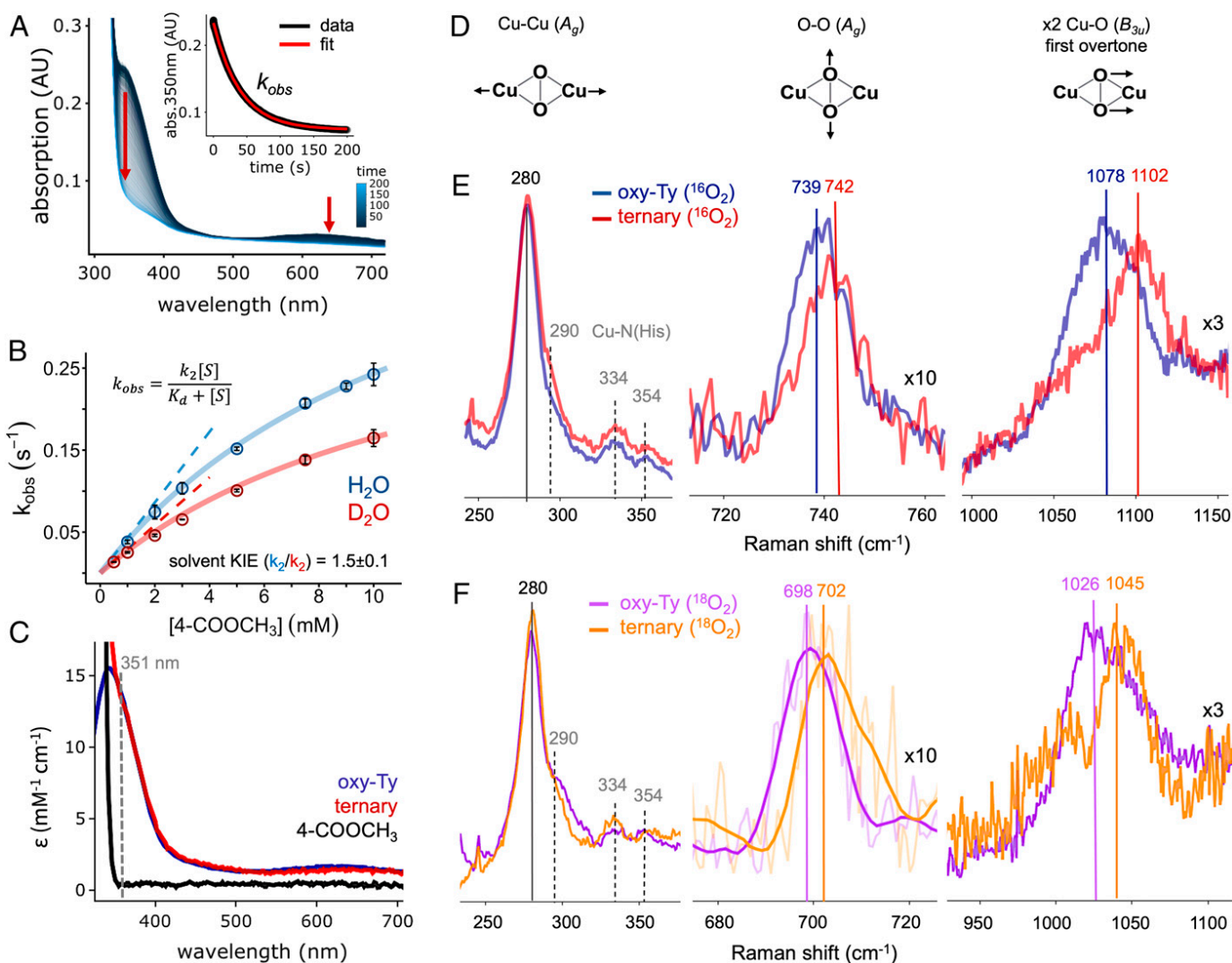
Fig. 2. Kinetic and spectroscopic definition of the ternary intermediate (Ty/O_2/4-COOCH$_3$). (*A*) SF-Abs spectra of the reaction of oxy-Ty (20 μM) with 4-COOCH$_3$ (1 mM) in O_2-saturated borate buffer (pH 9.0, 4 °C, 10% ethylene glycol). Insert: 350 nm absorption (abs) trace with first-order decay fit (AU; absorbance units). (*B*) Dependence of k_{obs} on 4-COOCH$_3$ concentration in H$_2$O (blue) and D$_2$O (red) with saturation fits for a fast equilibrium, followed by a slow irreversible step (equation shown as insert, complete model fits shown as solid lines, and linear fits for low substrate concentrations shown as dashed lines; error bars denote standard deviations for n = 3). (*C*) UV-vis absorption spectra for the ternary intermediate (red), oxy-Ty (blue), and 4-COOCH$_3$ (black), with the excitation wavelength for rR (351 nm) indicated as a dashed gray line. (*D*) The main vibrational modes of the Cu$^{II}_2$O$_2$ core (D_{2h}) that are resonance enhanced with excitation of the peroxide(π^*_σ)→Cu^{II} CT. (*E* and *F*) rR spectra (351-nm laser excitation) of oxy-Ty and the ternary intermediate (Ty/O$_2$/4-COOCH$_3$) in (*E*) ^{16}O$_2$ and (*F*) ^{18}O$_2$, with the relative intensity of each region scaled as indicated. Solid vertical lines indicate the energies of the main vibrational modes and dashed gray lines the Cu-N(His) modes. The oxy-Ty and the ternary intermediate samples were obtained by RFQ (100 ms) after 1:1 mixing of deoxy-Ty (0.8 mM) and an O$_2$-saturated solution of borate buffer (pH 9.0, 4 °C, 10% ethylene glycol) without or with 4-COOCH$_3$ (20 mM), respectively. The rR spectra were obtained after correction for background contributions, with the spectrum of the pure ternary intermediate obtained by further correcting for the oxy-Ty contributions in the RFQ reaction mixture and subsequent intensity renormalization. Due to experimental limitations resulting in lower ^{18}O$_2$ concentrations in *F* (*SI Appendix, Materials and Methods*, section 1.1.9), additional first- and second-order polynomial baseline corrections were applied for the 680- to 720- and 950- to 1,100-cm^{-1} regions, respectively, with a smoothened spectrum also included in the 680- to 720-cm^{-1} region. The $^{16/18}$O$_2$ rR spectra, without smoothening, are shown in *SI Appendix*, Fig. S11.

Our single-turnover SF-Abs experiments also allowed investigations of the reactivity of the ternary intermediate by probing the monooxygenation step (k_2) following the binding of the monophenol substrate to oxy-Ty. First, upon solvent isotopic substitution (H$_2$O/D$_2$O), the reaction of deoxy-Ty with 4-COOCH$_3$ in O$_2$-saturated borate buffer exhibits a small normal solvent kinetic isotope effect (KIE) of 1.5 ± 0.1 on k_2 (Fig. 2*B*). Since the geometric structure of the oxy-Ty active site is not perturbed upon solvent deuteration (27), the observed solvent KIE likely reflects the participation of one or more exchangeable protons in the transition state (TS) of the RLS, clearly implicating the phenolic substrate proton in the monooxygenation reaction mechanism. This is fully consistent with our pH dependence results (*SI Appendix*, Fig. S7*A*), demonstrating

that the substrate binds to oxy-Ty as a monophenol, and further suggests that the bound substrate remains fully protonated in the ternary intermediate. Second, the reaction of oxy-Ty with the dideuterated (in both *ortho* positions to the hydroxy group) 4-COOCH$_3$ substrate does not exhibit an inverse secondary KIE on k_2 (or an equilibrium isotope effect on K_d, *SI Appendix*, Fig. S7*C*) indicating that in the TS of the RLS, the *ortho*-C center (to be hydroxylated) retains a significant amount of its sp^2 character, since a small inverse KIE is expected for a fully C(sp^3) TS (30). Third, the Eyring plot for the temperature dependence of k_2 in the reaction of oxy-Ty with 4-COOCH$_3$ provides the enthalpic (ΔH‡ = +10.3 ± 0.7 kcal/mol) and entropic (ΔS‡ = −0.023 ± 0.003 kcal/mol*K) components of the RLS in the monooxygenation reaction (*SI Appendix*, Fig. S7*B*).

2.3. Spectroscopic definition of the ternary intermediate. Both oxy-Ty and the ternary intermediate (Ty/O$_2$/4-COOCH$_3$) were trapped at ∼100 ms by rapid-freeze quench (RFQ) after 1:1 mixing of deoxy-Ty (0.8 mM) with an O$_2$-saturated buffer solution (0.5 M borate, pH 9.0, 4 °C) without and with 4-COOCH$_3$ (10 mM), respectively, and their rR spectra were collected with 351-nm laser excitation into their high-energy peroxide(π^*_σ)→Cu^{II} CT band (Fig. 2*C*). The rR spectrum of oxy-Ty exhibited the characteristic resonance-enhanced peaks associated with the µ-η^2:η^2-peroxide dicopper(II) vibrational modes (Fig. 2 *D*; blue/purple spectra in Fig. 2 *E* and *F* and Figs. S9*A* and S11) (31). These modes include 1) the Cu-Cu (A$_g$) stretch at 280 cm^{-1} (Δ^{18}O$_2$ < −2 cm^{-1}), 2) the weak Cu-N(His) modes in the 290- to 360-cm^{-1} region (Δ^{18}O$_2$ < −2 cm^{-1}), 3) the peroxide O-O (A$_g$) stretch at 739 cm^{-1} (Δ^{18}O$_2$ = −40 cm^{-1}), and 4) the intense first overtone of the Cu-O (B$_{3u}$) mode at 1,078 cm^{-1} (Δ^{18}O$_2$ = −51 cm^{-1}), which is allowed and present at double the frequency of its corresponding weak fundamental mode, which is nontotally symmetric and thus rR forbidden.

The rR spectrum for the RFQ 100-ms reaction mixture of oxy-Ty (57%) and the ternary intermediate (43%) also exhibits the characteristic peaks for a µ-η^2:η^2-peroxide dicopper(II) active site (*SI Appendix*, Fig. S9*A*). Importantly, the normalized peak intensity of the O-O (A$_g$) stretch (using the nearby borate peak at 920 cm^{-1} as an internal standard) in the oxy-Ty (57%)/ ternary intermediate (43%) mixture is equivalent to that of oxy-Ty (100%), further confirming our SF-Abs results that the

ternary intermediate contains a µ-η^2:η^2-peroxide dicopper(II) active site (*SI Appendix*, Fig. S9*A*, insert). Comparison between the corrected (for baseline, buffer, and speciation) and intensity-renormalized rR spectra of oxy-Ty and the ternary intermediate reveals the spectral changes due to interactions between the µ-η^2: η^2-peroxide dicopper(II) core and the bound substrate (Fig. 2 *E* and *F* and *SI Appendix*, Fig. S9). These include 1) a 3 ± 2 cm^{-1} increase of the O-O (A$_g$) stretch; 2) a 24 ± 6 cm^{-1} increase of the first overtone of the Cu-O (B$_{3u}$) stretch, indicating a 12 ± 3 cm^{-1} increase in the corresponding fundamental mode; and 3) no significant change (<±2 cm^{-1}) in the Cu-Cu and Cu-N(His) modes. Note that upon solvent deuteration and within our signal-to-noise ratio, no significant perturbations (>±6 cm^{-1}) in the rR mode frequencies for the ternary intermediate were resolved (*SI Appendix*, Fig. S12). Together, our spectroscopic results demonstrate that the electronic/geometric structure of the µ-η^2:η^2-peroxide dicopper(II) site in oxy-Ty is only moderately perturbed upon binding of the monophenol substrate to form the ternary intermediate.

2.4. Correlation of spectroscopic data to QM/MM models: Geometric and electronic structure of the ternary intermediate. To elucidate the geometric and electronic structure of the ternary intermediate, our spectroscopic results (sections 2.2 and 2.3) were correlated to QM/MM calculations. We have recently reported the experimentally calibrated, QM/MM-optimized structure of oxy-Ty from *Streptomyces castaneoglobisporous* (Fig. 1*B*; 100% active-site homology with *S. glaucescens*), which contains H-bonding
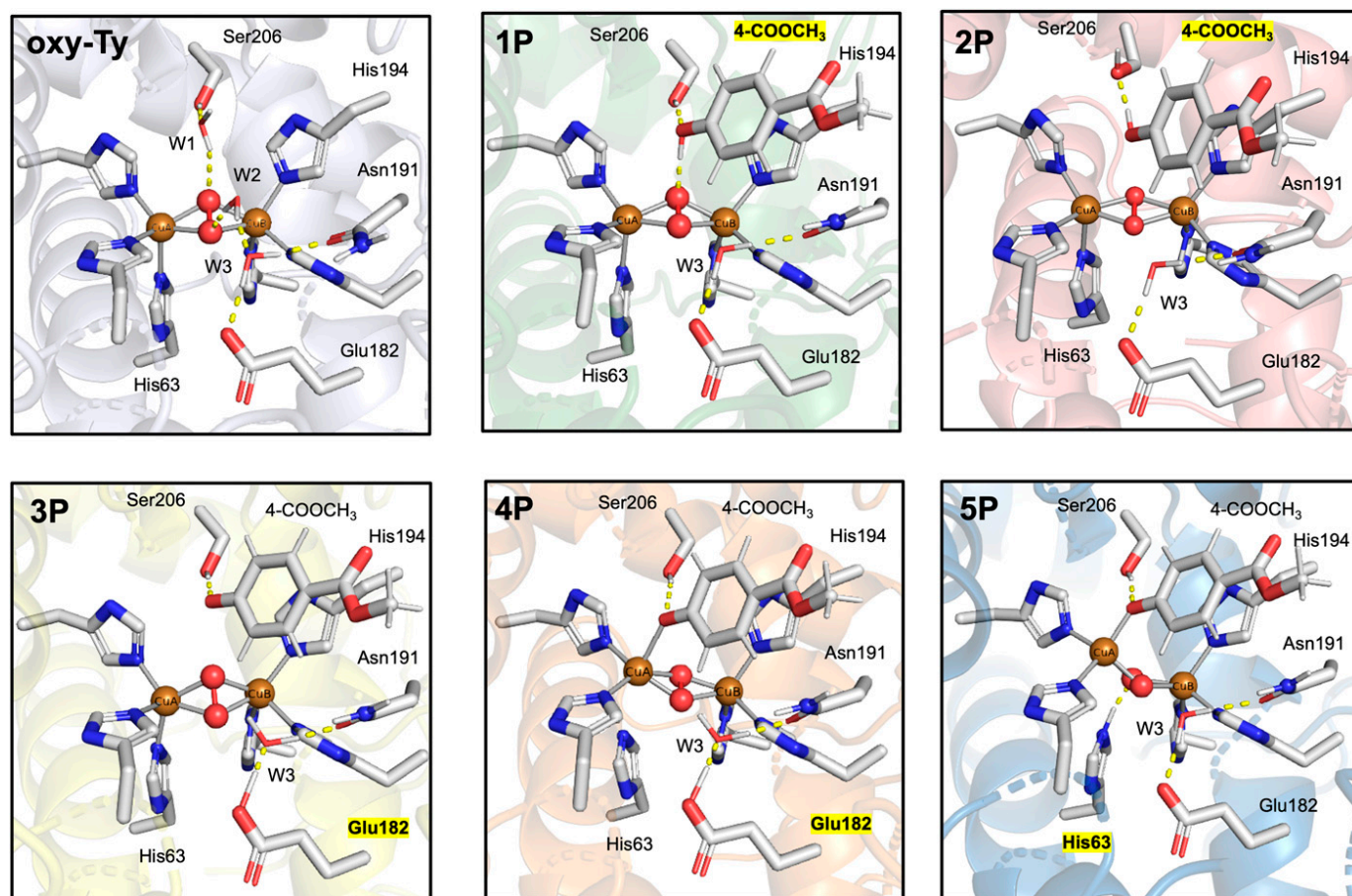

Fig. 3. The active sites of the QM/MM-optimized structures of oxy-Ty in *S. castaneoglobisporous* and its possible ternary intermediates (Ty/O$_2$/4-COOCH$_3$; 1P to 5P). Key active-site residues and the bound substrate (4-COOCH$_3$) are shown as sticks, the Cu sites and the µ-η^2:η^2-peroxide atoms are shown as spheres, the Cu coordination bonds are shown as solid gray lines, and H-bonding interactions are shown as dashed yellow lines. The label of the phenolic proton site in each ternary structure is highlighted in yellow. Equivalent structures for the possible ternary intermediates with the native substrate, L-tyrosine, are shown in *SI Appendix*, Fig. S15.

interactions between conserved active-site water molecules (W1 and W2) and the μ-η^2:η^2-peroxide (oxy-Ty in Fig. 3) (27). This oxy-Ty structure was employed as both the reference for the oxy-Ty active site and the starting point to generate a series of distinct QM/MM-optimized structures for possible ternary intermediates containing a μ-η^2:η^2-peroxide dicopper(II) active site (1P to 5P in Fig. 3). These ternary structures include, to the best of our knowledge, all those proposed in previous enzymatic and model complex studies (21, 24, 32) and were generated by systematically evaluating all reasonable possibilities involving the phenolic proton acceptor site, including the nearby Glu182/Asn191/W3 site (3P to 4P in Fig. 3) and the axial His63 ligand (5P in Fig. 3), as well as the possibility that the phenolic proton remains on the bound substrate (1P to 2P in Fig. 3 and 6P in *SI Appendix,* Fig. S17). For each of these possibilities, we also considered whether or not the substrate coordinates to Cu_A (i.e., the Cu coordinated by His residues closer to the N terminus; 3P versus 4P to 5P and 1P to 2P versus 6P in Fig. 3 and *SI Appendix,* Fig. S16; note that 6P requires fixed $O_{substrate}$-Cu_A coordination to obtain an optimized structure and relaxes to 1P when the constraint is removed). Finally, in the case where the substrate binds protonated as a monophenol, we further considered the possibility that it can H bond to the μ-η^2:η^2-peroxide via its hydroxyl group (1P versus 2P in Fig. 3). This approach allowed us to compile a comprehensive set of all reasonable structures for the ternary intermediate. Common in all of our QM/MM-optimized ternary structures is that the substrate is docked in the active-site pocket via π-π stacking interactions with His194 of Cu_B (i.e., the Cu coordinated by His residues closer to the C terminus), consistent with the previously reported Ty crystal structures with L-tyrosine bound to Zn-substituted and caddie-bound Ty crystal structures (15, 22).

The calculated changes in the electronic absorption and vibrational frequencies for the possible ternary intermediates (1P to 5P) relative to the oxy-Ty reference are summarized in Table 1. First, QM-frequency calculations for the ternary intermediate structures with the bound monophenolate substrate coordinated to Cu_A or the substrate phenolic proton transferred to either the nearby conserved Glu182 (4P in Fig. 3) or the now-dissociated axial His63 ligand of Cu_A (5P in Fig. 3), respectively, show either a large increase in the Cu-O stretch ($+81$ cm^{-1}; 4P) or a large decrease in the O-O stretch (-50 cm^{-1}; 5P), both inconsistent with our rR results. In addition, time-dependent density functional theory (TD-DFT) calculations show that the absorption spectra for both 4P and 5P would exhibit significant differences from that of oxy-Ty

(*SI Appendix,* Fig. S14). Similarly, for the ternary intermediate structure with the bound monophenolate substrate not coordinated to a metal site and with its phenolic proton transferred to Glu182 (3P in Fig. 3), QM-frequency calculations predict a large increase of the O-O frequency ($+24$ cm^{-1}) and TD-DFT calculations indicate a decrease in the energy of the intense high-energy absorption band ($+30$ nm), both inconsistent with our experimental results. However, formation of the ternary intermediate by docking of the substrate protonated, noncoordinated to Cu_A, and H-bonded to the μ-η^2:η^2-peroxide (1P) most closely reproduces both the observed UV-vis absorption (*SI Appendix,* Fig. S14) and the rR spectra (along with their $^{16/}$$^{18}O_2$ and H_2O/D_2O perturbations; Table 1) and is the most thermodynamically stable structure among the possible ternary intermediates in Table 1. Note that removal of the H-bonding interaction between the hydroxyl group of the bound substrate and the μ-η^2:η^2-peroxide in 1P (resulting in 2P in Fig. 3) results in QM-frequency changes that no longer reproduce our rR (Table 1) and UV-vis absorption results (*SI Appendix,* Fig. S14), while the thermodynamic energy increases by $+5$ kcal/mol. In addition, even when considering each of the 63 distinct structures for the oxy-Ty active site (with various active-site hydration levels, number/strength of water H bonds to the μ-η^2:η^2-peroxide, and thermodynamic stabilities) that we had previously evaluated toward defining the oxy-Ty structure shown in Fig. 3 (27), none of the 2P to 5P ternary structures can reproduce the observed O-O (A_g) and Cu-O (B_{3u}) vibrational perturbations (*SI Appendix,* Fig. S13).

Overall, our experimentally supported QM/MM model defines the electronic and geometric structure of the elusive catalytic ternary intermediate of Ty (1P in Fig. 3). Importantly, upon substrate binding to the oxy-Ty active site, the two conserved water molecules (W1 and W2 in oxy-Ty in Fig. 3) are displaced, and their direct H-bonding interactions with μ-η^2:η^2-peroxide (r[O_{W1}-O_1] = 3.1 Å, r[O_{W2}-O_2] = 2.8 Å) are replaced by a single moderate H bond from the hydroxyl group (r[$O_{substrate}$-O_1] = 2.7 Å). The mechanistic implications to the monooxygenation reaction that arise from this unprecedented substrate binding mode in 1P and its H-bonding interaction to the μ-η^2:η^2-peroxide are explored below.

2.5. Mechanistic insights into the monooxygenation reaction from experimentally supported QM/MM calculations. While the complete reaction coordinate of Ty will be the subject of a future study, here we provide mechanistic insights into the two key steps of the monooxygenation reaction. To this end, we

Table 1. Summary for the correlation of experimental with computational results for the possible ternary (Ty/O$_2$/4-COOCH$_3$) intermediates from Fig. 3.

| | Frequency changes for key Cu$_2$O$_2$ vibrational modes (cm^{-1}) | | | | | | Same UV-vis abs. spectra for ternary and oxy-Ty* | Relative energy[†] (kcal/mol) |
| | Δ(ternary-oxy-Ty) | | | Ternary Δ($^{18}O_2$-$^{16}O_2$)/Δ(D$_2$O-H$_2$O) | | | | |
	Cu-Cu (A_g)	Cu-O (B_{3u})	O-O (A_g)	Cu-Cu (A_g)	Cu-O (B_{3u})	O-O (A_g)		
Exp.	0 ± 2	+12 ± 3	+3 ± 2	0 ± 2/0 ± 2	−29 ± 6/0 ± 6	−40 ± 2/0 ± 2	yes	—
1P	+11	+18	−3	−2/0	−20/−2	−50/−1	yes	0.0
2P	+24	+69	−5	−1/0	−15/+6	−49/−1	no	+5.1
3P	+21	−2	+24	−5/0	−19/0	−50/0	no	+21.4
4P	+18	+81	−13	−4/0	−21/0	−49/0	no	+22.5
5P	+21	+25	−50	−6/0	−21/−3	−43/+1	no	+8.1

Exp, denotes experimental values and abs, UV-Vis absorption.
*For 1P to 5P, the TD-DFT spectra are shown in *SI Appendix,* Fig. S14.
[†]QM-only energy upon QM/MM-optimized geometries using the TPSS/def2-TZVPD level of theory in the homogeneous dielectric continuum with ε_r = 8.

correlated our experimental data on the monooxygenation reaction to QM/MM and QM-only (i.e., QM-cluster calculations on top of the QM/MM-optimized structures) calculations to evaluate the reaction steps following the formation of the ternary intermediate (Ty/O$_2$/4-COOCH$_3$) and toward the aromatic *ortho*-hydroxylation of the bound substrate. Starting from the newly defined structure of 1P (Fig. 3), we systematically assessed reaction steps by obtaining intermediates and their corresponding TSs along 1) O-O bond cleavage of the μ-η^2:η^2-peroxide, 2) substrate deprotonation via cleavage of its O-H bond, 3) substrate monooxygenation via C$_{ortho}$-O bond formation, and 4) substrate coordination via Cu$_A$-O$_{substrate}$ bond formation.

Direct *ortho*-hydroxylation of the protonated substrate in 1P by the μ-η^2:η^2-peroxide or bis-μ-oxo (after O-O cleavage) exhibit high-energy barriers (>25 kcal/mol, *SI Appendix,* Fig. S16), indicating that the hydroxylation step must be preceded by deprotonation of the bound substrate. While in section 2.4 (and *SI Appendix,* section 2.5.2) we determined that the previously proposed proton-acceptor active-site residues show low basicity (Glu182/Asn191/W3 for 3P and His63 for 4P in Fig. 3, Table 1, and *SI Appendix,* section 2.5.2), the Cu$_2$O$_2$ core is

a plausible H-acceptor site, particularly in its bis-μ-oxo form. Indeed, a two-dimensional (2D) scan along the cleavage of both the peroxide O-O and the substrate O-H bonds (Fig. 4*B*) shows a low TS barrier (+7.0 kcal/mol) for O-O cleavage, enabling fast H$^+$ transfer (along with 0.6 electron spin density; *SI Appendix,* Table S2) to form a μ-oxo-μ-hydroxo dicopper intermediate (2O in Fig. 4*A*) of reasonable thermodynamic stability (+1.5 kcal/mol). Comparison of the QM/MM reaction coordinates between 1P and 2P reveals that the H-bonding interaction between the substrate hydroxyl group and the μ-η^2:η^2-peroxide in 1P stabilizes not only the reactant state (by +5.1 kcal/mol) but also the resulting 2O intermediate (by +7 kcal/mol; *SI Appendix,* Fig. S18). Thus, in the ternary intermediate, the H-bonding interaction between the protonated substrate and the μ-η^2:η^2-peroxide enables the efficient cleavage of the μ-η^2:η^2-peroxide O-O bond and enhances H$^{+/•}$ transfer to the Cu$_2$O$_2$ core, making the resulting 2O intermediate thermodynamically accessible.

In 2O, the substrate *ortho*-C is oriented toward the nonprotonated μ-oxo of the Cu$_2^{II/III}$(O)(OH) intermediate, while its phenolate O-atom is oriented toward Cu$_A$ (Fig. 5*A*). From 2O, a 2D scan for the concerted formation of the C-O and Cu$_A$-O$_{phenolate}$
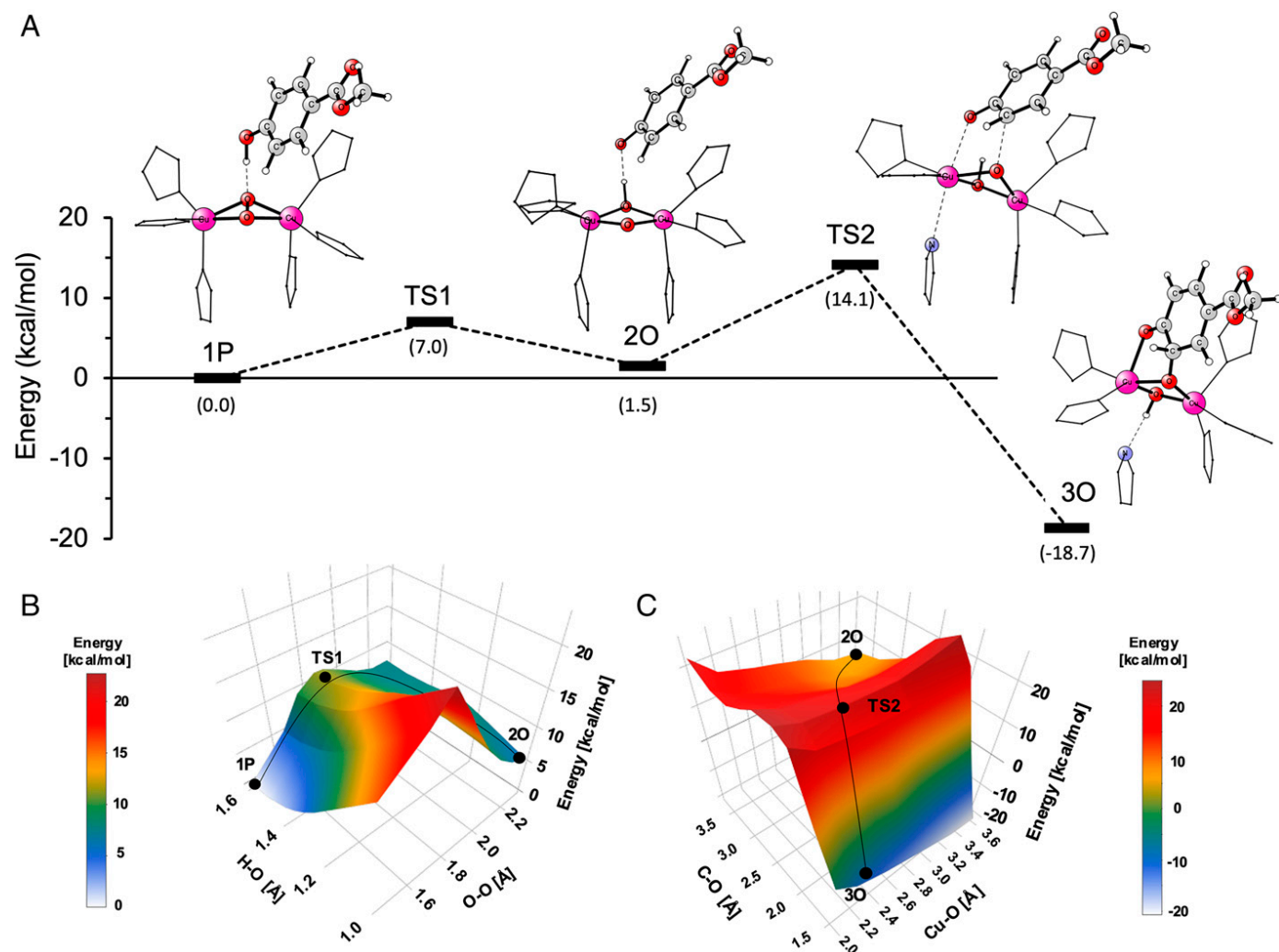

Fig. 4. Experimentally supported QM/MM mechanism of the key steps in the monooxygenase reaction of Ty. (*A*) The calculated reaction coordinate with energies and structures for the key intermediates and TSs. The Cu$_2$O$_2$ core and the bound 4-COOCH$_3$ substrate are shown as sticks, the first-coordination His residues are shown as lines, and all other atoms are omitted for clarity. Energies are calculated as single points upon the QM/MM-optimized geometries at the TPSS/def2-TZVPD level of theory in a homogeneous dielectric continuum with ε$_r$ = 8. (*B* and *C*) The 2D scans for the two steps in the monooxygenation mechanism shown in *A* (reaction coordinates in *B* are O$_{peroxide}$-H$_{phenolic}$ and O-O$_{peroxide}$ and in *C* are C$_{phenol}$-O$_{μ-oxo}$ and Cu$_A$-O$_{phenolate}$) performed at the QM/MM/TPSS/def2-SVP level of theory.
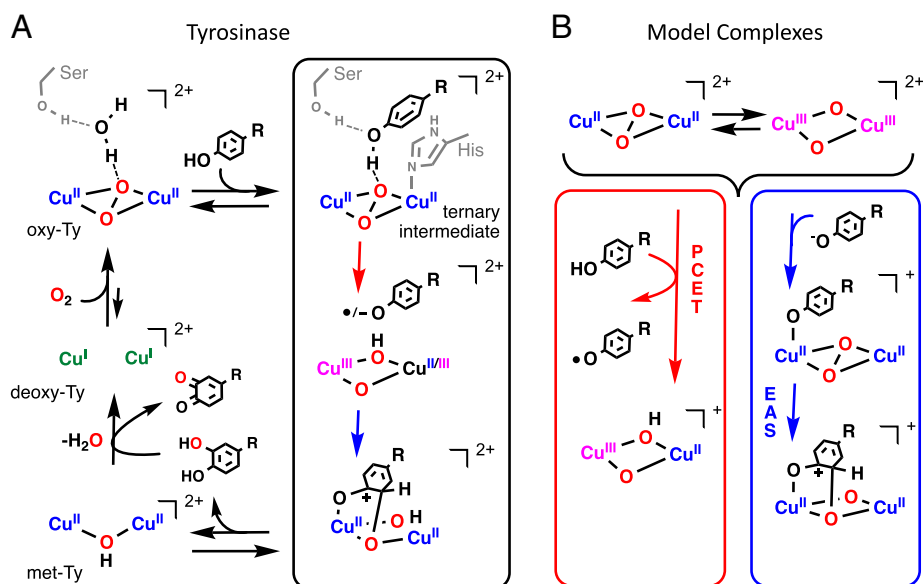
Fig. 5. Overview of the Cu_2O_2 chemistry in (*A*) Ty (from this study) and (*B*) model complexes.

bonds (Fig. 4*C*) shows a TS barrier of +14.1 kcal/mol to generate the thermodynamically favorable intermediate 3O (−18.7 kcal/mol), where the *ortho*-hydroxylated substrate is bridging the $Cu_2^{II}(OH)$ core (Fig. 4*A*). In this QM/MM-calculated mechanism, the TS (+14.1 kcal/mol) of the RLS is along the hydroxylation step, where the flexible $Cu_2^{II/III}(O)(OH)$ core moves toward the bound substrate to initiate the nonprotonated μ-oxo attack on the *ortho*-C concomitant with phenolate coordination to Cu_A. It should be noted that unlike previous proposals (24), the phenolic proton remains on the Cu_2O_2 core, as transfer to the nearby dissociated axial histidine of Cu_A is thermodynamically unfavorable along the entire monooxygenation reaction (*SI Appendix*, section 2. 5.2). Our calculations also indicate that the native substrate, L-tyrosine, follows a very similar (kinetically and thermodynamically) monooxygenation reaction coordinate (*SI Appendix*, Fig. S19) to the one for the slow 4-$COOCH_3$ substrate (Fig. 5*A*).

The reaction coordinate in Fig. 5*A* was further evaluated by correlating the QM/MM-derived TS for the RLS with the experimental kinetic parameters obtained from the single-turnover monooxygenation reaction of oxy-Ty with 4-$COOCH_3$ from section 2.2. First, the experimental TS barrier of the RLS ($\Delta H^{\ddagger}_{exp}$ = +10.3 ±0.7 kcal/mol) is in reasonable agreement with the reaction coordinate in Fig. 4 ($\Delta E^{\ddagger}_{calc}$ = +14.1 kcal/mol, $\Delta H^{\ddagger}_{calc}$ = +11.4 kcal/mol) and is significantly lower than the corresponding barriers of other possible reaction coordinates (*SI Appendix*, section 2.5.1). Second, the experimentally observed small normal solvent KIE on k_2 (1.5 ± 0.1) is closely reproduced by QM-frequency calculations (calculated solvent KIE = 1.3; *SI Appendix*, *Materials and Methods*, section 1.2.7). Third, the lack of an experimentally observed inverse secondary KIE upon *ortho*-C-H/D substitution (1.05 ± 0.05) is in agreement with QM-frequency calculations (calculated secondary KIE = 1.0; *SI Appendix*, *Materials and Methods*, section 1.2.7) and is consistent with the small amount of sp^3 character of the *ortho*-C center in the structure of the TS of the RLS (TS2 in Fig. 4*A*). Together, our experimentally supported QM/MM calculations provide critical insights into the two key steps in the monooxygenation reaction mechanism of Ty, where the μ-$η^2$:$η^2$-peroxide O-O bond cleaves to accept the phenolic proton from the substrate, followed by coordination of the substrate phenolate to Cu_A concomitant with the *ortho*-hydroxylation of its aromatic ring by the nonprotonated μ-oxo of the $Cu_2(O)(OH)$ core.

3. Discussion

In this study, we have trapped and spectroscopically characterized the elusive catalytic ternary intermediate (Ty/O_2/monophenol) in the monooxygenation reaction of Ty. Correlation of our spectroscopic results to QM/MM calculations reveals the geometric and electronic structure of this ternary intermediate (1P in Fig. 3). The preservation of the μ-$η^2$:$η^2$-peroxide $Cu^{II}_2O_2$ core in this intermediate disproves previous proposals for conversion to a bis-μ-oxo $Cu^{III}_2O_2$ isomer upon substrate binding (20, 33). Importantly, the substrate binds fully protonated (i.e., as a monophenol) and forms an H bond to the μ-$η^2$:$η^2$-peroxide of the $Cu^{II}_2O_2$ core. Note that comparison of the active-site structure of 1P with that of the caddie protein bound to oxy-Ty (Protein Data Bank [PDB]: 1WX2) (34) reveals that the caddie residue Y98 is positioned similarly to the bound monophenol in 1P, and while not previously defined, it is likely to also be protonated and H-bonded to the μ-$η^2$:$η^2$-peroxide.

The substrate binding mode in 1P revises previous mechanistic proposals (21, 24, 35), all invoking a deprotonated monophenolate substrate directly coordinated to a Cu site, and thus, our study opens a framework for understanding the monooxygenation reactivity of Ty. First, our results provide an answer to the highly debated question regarding the identity of the proton acceptor site, where the candidates previously considered include 1) a second-sphere residue cluster (H_2O/Glu182/Asn191) (22), 2) one of the first-coordination sphere His residues (24), and 3) the $Cu^{II}_2O_2$ core to form a hydroperoxide (25, 36–38). Our results indicate that H^+ transfer to any of these active-site residues is not thermodynamically favorable (Table 1 and *SI Appendix*, section 2.5.2), and it is, in fact, the μ-$η^2$:$η^2$-peroxide that cleaves its O-O bond to accept the $H^{+/\bullet}$ from the bound substrate. This $H^{+/\bullet}$ transfer is facilitated by the direct H-bonding interaction between the μ-$η^2$:$η^2$-peroxide and the substrate hydroxyl group in 1P and is enabled by the attack of the Cu_2O_2 peroxide σ* unoccupied frontier molecular orbital on the highest occupied molecular orbital of the phenolic substrate (*SI Appendix*, Fig. S20). Second, the RLS of the monooxygenation reaction involves the concerted coordination of the monophenolate substrate to Cu_A with the formation of the C-O bond via the attack of the nonprotonated μ-oxo of the $Cu_2(O)(OH)$ core on the ortho-C of the substrate (Fig. 4*A*). During this step, Cu_A moves by

1.6 Å, dissociating from its axial histidine and coordinating the monophenolate substrate that is bound in the protein pocket, consistent with the plasticity of Cu$_A$ observed in previous crystallographic studies (15, 24, 39).

The monooxygenation reaction mechanism defined in this study (Fig. 5A) accounts for the results of previous mechanistic studies of Ty and integrates the diverse reactivities of Cu$_2$O$_2$ model complexes toward monophenols or monophenolates within the biological context of the CBC enzymes. This study extends the facile interconversion between the µ-η^2:η^2-peroxide Cu$^{II}_2$O$_2$ and bis-µ-oxo Cu$^{III}_2$O$_2$ isomers (Fig. 5B, *Top*) (18) beyond model complexes to the Ty active site, where in the enzyme, this interconversion is coupled to H$^{+/\bullet}$ transfer from the bound substrate to the Cu$_2$O$_2$ core (Fig. 5A, red arrow). Note that H$^\bullet$ transfer to the µ-η^2:η^2-peroxide/bis-µ-oxo is also observed in the reaction of monophenols with [Cu$_2$O$_2$]$^{2+}$ model complexes (Fig. 5B, red box), which also exhibit small normal solvent KIE values (40). However, unlike model complexes, Ty provides protein pocket interactions that stabilize and orient the bound monophenolic substrate (Fig. 3) toward productive monooxygenation, rather than cage escape and phenoxyl radical coupling. The monophenolate coordination of the Cu center coupled to C-O bond formation in the RLS of the enzymatic monooxygenation reaction (Fig. 5A, blue arrow) is also observed in the reaction of Cu$_2$O$_2$ model complexes with monophenolate substrates (Fig. 5B, blue box) (20). However, in model complexes, this reaction step involves a Cu$_2$O$_2$ core with or without substrate coordination, while in Ty, it involves a protonated Cu$_2$(O)(OH) species (Fig. 4).

An interesting consideration in the above reaction steps is the degree of concerted versus sequential two-electron transfer (ET) from the monophenolic substrate to the Cu$_2$O$_2$ core, leading to an electrophilic aromatic substitution (EAS) versus radical-coupling description, respectively. Our QM/MM calculations describe the monooxygenation mechanism as more sequential, where proton-coupled ET is followed by partial radical coupling (Fig. 4). Previous studies have argued for an EAS mechanism (28) based on the similarity of the Hammett linear free-energy dependence of the steady-state kinetic parameters for the reaction of Ty with monophenols ($\rho = -2.4$) with those for the EAS of monophenolates by µ-η^2:η^2-peroxide Cu$^{II}_2$O$_2$ model complexes ($\rho = -1.8$). However, we find that the Hammett plot for the steady-state kinetics is different from that for the pre–steady-state/single-turnover monooxygenation (*SI Appendix*, Fig. S21), which is up to ×10^3 faster. Additional investigations are under way to determine the RLS step under steady-state conditions, as well as the concertedness of ET. Importantly, the insights from this study define the key reaction steps of the monooxygenation mechanism of Ty, where the O-O bond of the µ-η^2:η^2-peroxide Cu$_2$O$_2$ breaks to accept the phenolic H$^{+/\bullet}$, followed by attack of the nonprotonated µ-oxo on the *ortho*-C(sp^2) of the substrate, leading to formation of the Cu$_A$-O (phenolate) and C-O bonds via EAS/radical coupling (Fig. 5A).

Overall, by trapping the elusive catalytic ternary (Ty/O$_2$/monophenol) intermediate and defining its geometric and electronic structure, this study elucidates the key steps in the monooxygenation reaction of Ty. This mechanism unifies the diverse

Cu$_2$O$_2$ model complex chemistry with the CBC enzymatic reactivity in biology. The mechanistic insights from this study are of broad fundamental interest in catalysis for controlled O$_2$ activation via incorporation of CBC sites into the ligand scaffolds of small model complexes or extended solids, such as the highly reactive Cu zeolites (41) and the highly modular metal-organic frameworks (42). Furthermore, the molecular-level description of the substrate-enzyme interactions for the RLS in melanin biosynthesis presents critical information for ongoing synthetic efforts toward designing effective Ty inhibitors (43) and Ty-activated prodrugs (44). More broadly, defining the mechanistic requirements of enzymatic monooxygenation serves as the key reference for correlating the diverse reactivities among other members of the CBC protein family, including CaOxs, which can oxidize *o*-catechols to *o*-quinones but lack monooxygenase reactivity, and the recently discovered *o*-aminophenol oxidases, which are able to monooxygenate both monophenols to catechols and *o*-aminophenols to *o*-nitrosophenols (3, 45, 46). Further mechanistic and spectroscopic investigations into the CaOx and hydroxyanilase reactions are under way to elucidate how nature controls O$_2$ activation and reactivity in CBC active sites.

Materials and Methods

The protein expression, purification, and redox-sensitive anaerobic preparation of Ty from *S. glaucescens*, as well as the computational protein model setup, were performed following the methodology we previously reported (26). SF-Abs spectra were collected using a SX.19 Applied Photophysics instrument placed in an anaerobic glovebox, and rR spectra were collected using 351-nm excitation (Innova Sabre Ar+ laser, 20 mW, 77 K). In the QM/MM calculations, the QM part employed density functional theory (mostly TPSS-D3 functional, recently calibrated in CBC model complexes) (47), the MM part employed the Amber ff14SB force field, and the standard hydrogen link-atom approach (subtractive scheme) with the electrostatic embedding was employed as the QM/MM coupling. Detailed information on reagents and instrumentation, experimental setups, sample preparations, and spectroscopic and computational QM/MM methods are provided in *SI Appendix, Materials and Methods*.

Data, Materials, and Software Availability. All study data are included in the article and/or supporting information, with cartesian coordinates for all computational models provided in Dataset S1.

Author affiliations: ^{a}Department of Chemistry, Stanford University, Stanford, CA 94305; ^{b}Institute of Organic Chemistry and Biochemistry, Czech Academy of Sciences, 166 10, Prague 6, Czech Republic; ^{c}Faculty of Science, Charles University, 128 00 Prague 2, Czech Republic; and ^{d}Stanford Synchrotron Radiation Lightsource, SLAC National Accelerator Laboratory, Stanford University, Menlo Park, CA 94025

Author contributions: I.K., A.S., J.W.G., P.C.A., L.R., and E.I.S. designed research; I.K., A.S., J.W.G., and P.C.A. performed research; I.K., A.S., J.W.G., P.C.A., L.R., and E.I.S. analyzed data; and I.K., A.S., L.R., and E.I.S. wrote the paper.

1. K. Kirti, S. Amita, S. Priti, A. Mukesh Kumar, S. Jyoti, Colorful world of microbes: Carotenoids and their applications. *Adv. Biol.* **2014**, 1–13 (2014).
2. J. D. Simon, D. Peles, K. Wakamatsu, S. Ito, Current challenges in understanding melanogenesis: Bridging chemistry, biological control, morphology, and function. *Pigment Cell Melanoma Res.* **22**, 563–579 (2009).
3. E. I. Solomon *et al.*, Copper active sites in biology. *Chem. Rev.* **114**, 3659–3853 (2014).
4. J. D. Nosanchuk, A. Casadevall, The contribution of melanin to microbial pathogenesis. *Cell. Microbiol.* **5**, 203–223 (2003).
5. B. Ciui *et al.*, Wearable wireless tyrosinase bandage and microneedle sensors: Toward melanoma screening. *Adv. Healthc. Mater.* **7**, e1701264 (2018).
6. E. Buitrago *et al.*, Are human tyrosinase and related proteins suitable targets for melanoma therapy? *Curr. Top. Med. Chem.* **16**, 3033–3047 (2016).

7. I. Carballo-Carbajal *et al.*, Brain tyrosinase overexpression implicates age-dependent neuromelanin production in Parkinson's disease pathogenesis. *Nat. Commun.* **10**, 973 (2019).
8. N. Ananya, J. S. Kumar, S. H. Ram, L-DOPA, a promising pro-drug against Parkinson's disease: Present and future perspective. *Res. J. Biotechnol.* **14**, 10 (2019).
9. F. Tinello, A. Lante, Recent advances in controlling polyphenol oxidase activity of fruit and vegetable products. *Innov. Food Sci. Emerg. Technol.* **50**, 73–83 (2018).
10. M. J. Lobba *et al.*, Site-specific bioconjugation through enzyme-catalyzed tyrosine-cysteine bond formation. *ACS Cent. Sci.* **6**, 1564–1571 (2020).
11. A.-W. Struck *et al.*, An enzyme cascade for selective modification of tyrosine residues in structurally diverse peptides and proteins. *J. Am. Chem. Soc.* **138**, 3038–3045 (2016).
12. A. Frangu, K. Pravcová, P. Šilarová, T. Arbneshi, M. Sýs, Flow injection tyrosinase biosensor for direct determination of acetaminophen in human urine. *Anal. Bioanal. Chem.* **411**, 2415–2424 (2019).
13. M. Florescu, M. David, Tyrosinase-based biosensors for selective dopamine detection. *Sensors (Basel)* **17**, 1314 (2017).
14. K. Min, G. W. Park, Y. J. Yoo, J.-S. Lee, A perspective on the biotechnological applications of the versatile tyrosinase. *Bioresour. Technol.* **289**, 121730 (2019).
15. Y. Matoba, T. Kumagai, A. Yamamoto, H. Yoshitsu, M. Sugiyama, Crystallographic evidence that the dinuclear copper center of tyrosinase is flexible during catalysis. *J. Biol. Chem.* **281**, 8981–8990 (2006).
16. M. J. Baldwin *et al.*, Spectroscopic studies of side-on peroxide-bridged binuclear copper(II) model complexes of relevance to oxyhemocyanin and oxytyrosinase. *J. Am. Chem. Soc.* **114**, 10421–10431 (1992).
17. M. J. Baldwin *et al.*, Spectroscopic and theoretical studies of an end-on peroxide-bridged coupled binuclear copper(II) model complex of relevance to the active sites in hemocyanin and tyrosinase. *J. Am. Chem. Soc.* **113**, 8671–8679 (1991).
18. J. A. Halfen *et al.*, Reversible cleavage and formation of the dioxygen O-O bond within a dicopper complex. *Science* **271**, 1397–1400 (1996).
19. E. Pidcock, H. V. Obias, C. X. Zhang, K. D. Karlin, E. I. Solomon, Investigation of the reactive oxygen intermediate in an arene hydroxylation reaction performed by Xylyl-bridged binuclear copper complexes. *J. Am. Chem. Soc.* **120**, 7841–7847 (1998).
20. L. M. Mirica *et al.*, Tyrosinase reactivity in a model complex: An alternative hydroxylation mechanism. *Science* **308**, 1890–1892 (2005).
21. A. Spada, S. Palavicini, E. Monzani, L. Bubacco, L. Casella, Trapping tyrosinase key active intermediate under turnover. *Dalton Trans.* (33):6468–6471 (2009).
22. M. Goldfeder, M. Kanteev, S. Isaschar-Ovdat, N. Adir, A. Fishman, Determination of tyrosinase substrate-binding modes reveals mechanistic differences between type-3 copper proteins. *Nat. Commun.* **5**, 4505 (2014).
23. H. Decker, E. Solem, F. Tuczek, Are glutamate and asparagine necessary for tyrosinase activity of type-3 copper proteins? *Inorg. Chim. Acta* **481**, 32–37 (2018).
24. N. Fujieda *et al.*, Copper-oxygen dynamics in the tyrosinase mechanism. *Angew. Chem. Int. Ed. Engl.* **59**, 13385–13390 (2020).
25. J. S. Conrad, S. R. Dawso, E. R. Hubbard, T. E. Meyers, K. G. Strothkamp, Inhibitor binding to the binuclear active site of tyrosinase: Temperature, pH, and solvent deuterium isotope effects. *Biochemistry* **33**, 5739–5744 (1994).
26. Y. Matoba, K. Oda, Y. Muraki, T. Masuda, The basicity of an active-site water molecule discriminates between tyrosinase and catechol oxidase activity. *Int. J. Biol. Macromol.* **183**, 1861–1870 (2021).
27. I. Kipouros *et al.*, Evidence for H-bonding interactions to the μ-η^2:η^2-peroxide of oxy-tyrosinase that activate its coupled binuclear copper site. *Chem. Commun. (Camb.)* **58**, 3913–3916 (2022).
28. S. Yamazaki, S. Itoh, Kinetic evaluation of phenolase activity of tyrosinase using simplified catalytic reaction system. *J. Am. Chem. Soc.* **125**, 13034–13035 (2003).
29. J. N. Rodríguez-López, J. Tudela, R. Varón, F. García-Carmona, F. García-Cánovas, Analysis of a kinetic model for melanin biosynthesis pathway. *J. Biol. Chem.* **267**, 3801–3810 (1992).
30. B. T. Op't Holt *et al.*, Reaction coordinate of a functional model of tyrosinase: Spectroscopic and computational characterization. *J. Am. Chem. Soc.* **131**, 6421–6438 (2009).
31. N. C. Eickman, E. I. Solomon, J. A. Larrabee, T. G. Spiro, K. Lerch, Ultraviolet Resonance Raman Study of Oxytyrosinase. Comparison with Oxyhemocyanins. *J. Am. Chem. Soc.* **100**, 6429–6431 (1978).
32. E. Solem, F. Tuczek, H. Decker, Tyrosinase versus catechol oxidase: One asparagine makes the difference. *Angew. Chem. Int. Ed. Engl.* **55**, 2884–2888 (2016).
33. H. Decker, R. Dillinger, F. Tuczek, How Does Tyrosinase Work? Recent Insights from Model Chemistry and Structural Biology. *Angew. Chem. Int. Ed. Engl.* **39**, 1591–1595 (2000).
34. Y. Matoba *et al.*, Activation mechanism of the *Streptomyces* tyrosinase assisted by the caddie protein. *Biochemistry* **56**, 5593–5603 (2017).
35. D. E. Wilcox *et al.*, Substrate analog binding to the coupled binuclear copper active site in tyrosinase. *J. Am. Chem. Soc.* **107**, 4015–4027 (1985).
36. H. Jiang, W. Lai, Monophenolase and catecholase activity of *Aspergillus oryzae* catechol oxidase: Insights from hybrid QM/MM calculations. *Org. Biomol. Chem.* **18**, 5192–5202 (2020).
37. T. Lind, P. E. M. Siegbahn, R. H. Crabtree, A quantum chemical study of the mechanism of tyrosinase. *J. Phys. Chem. B* **103**, 1193–1202 (1999).
38. T. Inoue, Y. Shiota, K. Yoshizawa, Quantum chemical approach to the mechanism for the biological conversion of tyrosine to dopaquinone. *J. Am. Chem. Soc.* **130**, 16890–16897 (2008).
39. Y. Matoba *et al.*, Catalytic mechanism of the tyrosinase reaction toward the Tyr98 residue in the caddie protein. *PLoS Biol.* **16**, e3000077 (2018).
40. T. Osako *et al.*, Oxidation Mechanism of Phenols by Dicopper-Dioxygen (Cu_2/O_2) Complexes. *J. Am. Chem. Soc.* **125**, 11027–11033 (2003).
41. B. E. R. Snyder, M. L. Bols, R. A. Schoonheydt, B. F. Sels, E. I. Solomon, Iron and copper active sites in zeolites and their correlation to metalloenzymes. *Chem. Rev.* **118**, 2718–2768 (2018).
42. X. Feng *et al.*, Rational construction of an artificial binuclear copper monooxygenase in a metal-organic framework. *J. Am. Chem. Soc.* **143**, 1107–1118 (2021).
43. T.-S. Chang, An updated review of tyrosinase inhibitors. *Int. J. Mol. Sci.* **10**, 2440–2475 (2009).
44. M. Gabrielle *et al.*, Targeted prodrug design for the treatment of malignant melanoma. *J. Dermatol. Res. Ther.* **2**, 1–8 (2016).
45. J. W. Ginsbach *et al.*, Structure/function correlations among coupled binuclear copper proteins through spectroscopic and reactivity studies of NspF. *Proc. Natl. Acad. Sci. U.S.A.* **109**, 10793–10797 (2012).
46. A. Noguchi, T. Kitamura, H. Onaka, Y. Ohnishi, A copper-containing oxidase catalyzes C-nitrosation in nitrosobenzamide biosynthesis. *Nat. Chem. Biol.* **6**, 641–643 (2010).
47. A. Stańczak, J. Chalupský, L. Rulíšek, M. Straka, Comprehensive theoretical view of the [$Cu_2 O_2$] side-on-peroxo-/bis-μ-oxo equilibria. *ChemPhysChem*, e202200076 (2022).

Paper IV:
Experimental Evidence and Mechanistic
Description of the Phenolic H-Transfer to the
Cu_2O_2 Active Site of oxy-Tyrosinase

Experimental Evidence and Mechanistic Description of the Phenolic H-Transfer to the Cu₂O₂ Active Site of oxy-Tyrosinase

Ioannis Kipouros,[#] Agnieszka Stańczak,[#] Eleanor M. Dunietz, Jake W. Ginsbach, Martin Srnec, Lubomír Rulíšek,* and Edward I. Solomon*

ACCESS | 📊 Metrics & More | 📖 Article Recommendations | 🗎 Supporting Information

ABSTRACT: Tyrosinase is a ubiquitous coupled binuclear copper enzyme that activates O₂ toward the regioselective monooxygenation of monophenols to catechols via a mechanism that remains only partially defined. Here, we present new mechanistic insights into the initial steps of this monooxygenation reaction by employing a pre-steady-state, stopped-flow kinetics approach that allows for the direct measurement of the monooxygenation rates for a series of *para*-substituted monophenols by oxy-tyrosinase. The obtained biphasic Hammett plot and the associated solvent kinetic isotope effect values provide direct evidence for an initial H-transfer from the protonated phenolic substrate to the Cu₂O₂ core of oxy-tyrosinase. The correlation of these experimental results to quantum mechanics/molecular mechanics calculations provides a detailed mechanistic description of this H-transfer step. These new mechanistic insights revise and expand our fundamental understanding of Cu₂O₂ active sites in biology.

Coupled binuclear copper (CBC) active sites are found in a diverse set of catalysts, ranging from native and artificial metalloenzymes to heterogeneous materials, including zeolites and metal−organic frameworks.[1−4] These CBC sites have attracted significant interest, as they activate O₂ to catalyze a wide array of challenging oxidative transformations. In biology, the prototypical O₂-activating CBC enzyme tyrosinase (Ty) catalyzes the regioselective hydroxylation of *para*-substituted monophenols to catechols, including the conversion of L-tyrosine to L-3,4-dihydroxyphenylalanine (L-DOPA), which constitutes the initial step in melanin biosynthesis across a wide range of organisms from soil bacteria to humans.[1,5] In its fully reduced form (deoxy-Ty; center panel in Figure 1), its

dicopper(I) active site binds and activates O₂ to form a well-characterized μ-η²:η²-peroxide dicopper(II) intermediate (oxy-Ty; Figure 1)[6−10] that regioselective hydroxylates *para*-substituted monophenols to catechols. Then, it returns to its resting bicupric form (met-Ty), which can further oxidize catechols to quinone, thus completing the catalytic cycle (Figure 1).[1,5] Despite extensive investigations,[11−15] key aspects of this monooxygenation mechanism remain a subject of debate.[5,16−21]

The most commonly invoked mechanism for Ty involves Cu coordination of the monophenolate substrate, followed by electrophilic aromatic substitution (EAS) by the μ-η²:η²-peroxide dicopper(II) or its bis-μ-oxo dicopper(III) isomer (Figure 1, left). This was based on the similar Hammett plot parameters (ρ ∼ −2.0) between the steady-state monophenol monooxygenation rates of Ty[11,22] and the observed rates for monophenolate monooxygenation by synthetic μ-η²:η²-peroxide dicopper(II) model complexes.[23,24] Under physiological conditions (pH ∼ 7), the enzymatic monooxygenation mechanism requires an initial deprotonation step for the monophenol substrate (pKₐ ∼ 10); however, the identity of such a proton acceptor site (labeled as "B" in Figure 1, left) has remained elusive and a subject of debate.[25−29] We recently cryo-trapped and spectroscopically characterized the catalytic ternary intermediate (enzyme/O₂/monophenol; 1P in Figure 1, right) of Ty from *Streptomyces glaucescens*, where the substrate bound to oxy-Ty protonated as a monophenol H-
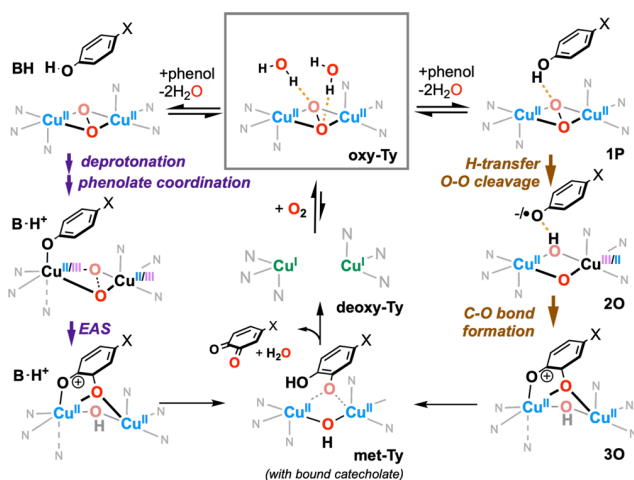

Figure 1. Catalytic cycle of Ty with the proposed mechanisms for monophenol monooxygenation by oxy-Ty (outlined with a gray box) from previous studies (left side) and our recent work (right side).[12]
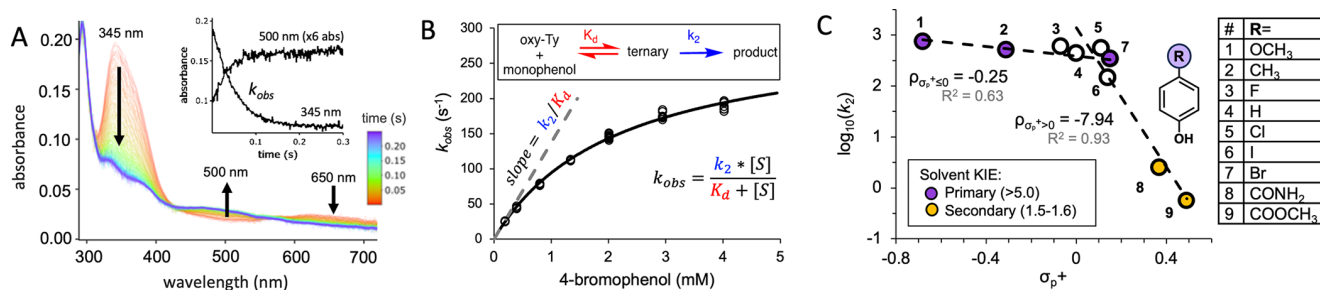
Figure 2. (A) Time-dependent stopped-flow absorption spectra for the reaction of deoxy-Ty (15 μM) with an O_2-containing solution of 4-bromophenol (0.4 mM) in a borate buffer (0.5 M, pH = 9.0, 4 °C); inset shows the 345 and 500 nm traces associated with oxy-Ty/ternary decay and the quinone product formation, respectively. (B) Dependence of k_{obs} from the decay of the 345 nm feature shown in (A) with increasing 4-bromophenol concentration and fit (solid line; fit is based on the kinetic model shown on top). (C) Hammett plot for the monooxygenation reaction. The linear fits for the two regions ($\sigma_p^+ < 0$ and $\sigma_p^+ > 0$)[30] are shown as dashed lines, with the primary (purple circles) vs secondary (yellow circles) SKIE values for five substrates included (rates and SKIE values are given in Table S1; an extended Hammett analysis is shown in Figure S2).

bonded to the μ-η^2:η^2-peroxide[12] by displacing active-site waters and replacing their H-bonds to the μ-η^2:η^2-peroxide (Figure 1).[8] The structure of this catalytic ternary intermediate opens a new mechanistic possibility, where the O–O bond of the μ-η^2:η^2-peroxide cleaves to accept the phenolic H$^+$ (with some electron transfer), followed by phenolate coordination to Cu concomitant with C–O bond formation (Figure 1, right).[12] A key experimental finding from our previous study[12] was that the monophenol monooxygenation rate of Ty measured in pre-steady-state conditions was ~2−3 orders of magnitude faster than its steady-state turnover rate; this result indicates that previous studies based on steady-state rate Hammett plots likely reflect a different rate-limiting step and are thus not relevant to the monooxygenation mechanism of Ty.[11,19,22]

As we previously demonstrated, the stopped-flow mixing of deoxy-Ty with an O_2-containing solution of monophenol results in the fast formation of an intense 345 nm absorption feature corresponding to the μ-η^2:η^2-peroxide dicopper(II) active site that is present in both oxy-Ty and the ternary intermediate, which are in a rapid equilibrium.[12] This 345 nm feature subsequently decays at a first-order rate (k_{obs}, Figure 2A inset) with the concomitant and near stoichiometric formation of the monooxygenation product(s) (i.e., catechol and/or quinone, with their ratio determined by the difference between the rates for catechol dissociation versus oxidation by met-Ty for a given substrate; see Scheme S1). In this study, the k_{obs} values were obtained for a series of monophenol substrates with different para-groups at increasing substrate concentrations. The k_{obs} values for all monophenols exhibit saturation with increasing substrate concentration (Figure 2B), which allows for the determination of their respective substrate dissociation constant (K_d) and the monooxygenation rate constant (k_2). The dependence of the k_2 values on the electron-donating ability of the monophenol para-groups (reflected in their σ_p^+ values)[30] is presented in the Hammett plot (Figure 2C). For monophenols with electron-withdrawing groups (EWGs), their $\log_{10}(k_2)$ values increase linearly with increasing electron density on the aromatic ring ($\rho_{\sigma_p^+ > 0} = -7.94$). However, for monophenols with electron-donating groups (EDGs), their $\log_{10}(k_2)$ values are only weakly dependent on the para-group ($\rho_{\sigma_p^+ \leq 0} = -0.25$). This biphasic substrate dependence of $\log_{10}(k_2)$ is further reflected in their strikingly different solvent kinetic isotope effect (SKIE) values for k_2. We previously reported that the monooxygenation rates for monophenols with EWGs (4-hydroxybenzamide, 4-

$CONH_2$; methyl 4-hydroxybenzoate, 4-$COOCH_3$) exhibit small secondary SKIE values (1.5−1.6; Figure 2C, yellow circles) that are associated with the C–O bond formation step (2O → 3O in Figure 1, right).[12] In this study, we report that, unlike monophenols with EWGs, the monooxygenation rates for monophenols with EDGs (4-bromophenol, 4-methyl, 4-methoxyphenol) exhibit large primary SKIE values (>5.0; Figure 2C, purple circles; Table S1). Note that, (i) as found in our previous study for 4-$COOCH_3$,[12] monophenols with EDGs (4-H and 4-OCH_3) did not exhibit a C–H/D KIE on k_2 (Table S1), and (ii) the Eyring plots for 4-Br and 4-$COOCH_3$ show that $\Delta G^{\ddagger}$ and $\Delta H^{\ddagger}$ decrease with increasing electron donation, consistent with their measured k_2 values, while a similar decrease in $\Delta S^{\ddagger}$ is observed for both substrates (Figure S4).

Taken together, this biphasic substrate para-group dependence of both the rate constants (Hammett plot) and the SKIE values of the monooxygenation reaction suggests a significant change in the nature of the rate-limiting transition state (TS) of the monooxygenation reaction upon tuning the electron-donating ability of the substrate para-group. In the monooxygenation of monophenols with EWGs, the secondary SKIE values suggest that their rate-limiting TS is after the H-transfer and O–O cleavage step, while their strong k_2 dependence on σ_p^+ suggests that this involves the aromatic hydroxylation step (since a positive charge builds up on the substrate). Conversely, in the monooxygenation of monophenols with EDGs, the large primary SKIE values combined with the weak dependence of their k_2 values on σ_p^+ indicate that their rate-limiting TS involves the transfer of the phenolic H atom. The detailed mechanistic description of this H-transfer with respect to whether this is a fully concerted H atom transfer (HAT; the electron (e$^-$) and H$^+$ transfer together as a H atom in a single elementary step) or a more sequential proton-coupled electron transfer (PCET; the e$^-$ and H$^+$ transfer, at least in part, at separate steps) process is investigated below by correlating our experimental results to electronic structure calculations.

Quantum mechanics/molecular mechanics (QM/MM) reaction coordinate calculations for the monooxygenation of a series of monophenols with different para-groups (from EWG to EDG) by oxy-Ty were performed to generate the two-dimensional (2D) potential energy surfaces (PESs) for the two steps in our proposed monooxygenation mechanism (the 1P → 2O and 2O → 3O steps shown on the right side of Figure 1,
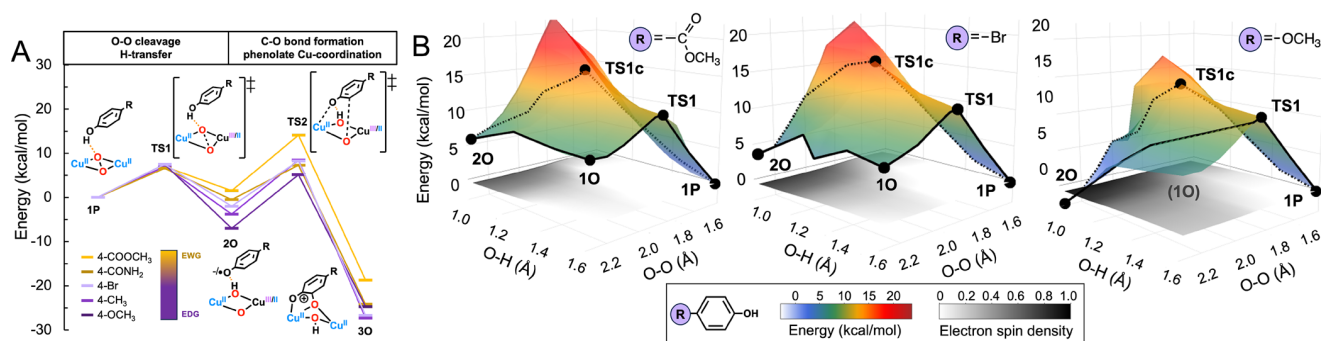
Figure 3. (A) Monooxygenation reaction coordinates for monophenols with different *para*-groups calculated from 2D PESs and performed at the QM(TPSS-D3BJ/def2-SVP)/MM level of theory. Energies of the intermediates and transition states were calculated using single-point calculations (TPSS-D3BJ/def2-TZVPD, $\varepsilon_r = 8$) of their QM/MM-optimized geometries (see Figure S8 and Table S2 for additional functionals and free energy corrections). (B) The 2D PESs for H-transfer and O−O cleavage for methyl 4-hydroxybenzoate (4-COOCH$_3$), 4-bromophenol (4-Br), and 4-methoxyphenol (4-OCH$_3$). The lowest-energy (more sequential) 1P → 2O path via TS1 is shown as a solid black line, and the fully concerted path via TS1c (defined as the midpoint of the 1P → 2O path at O−O = 1.85 Å and O−H = 1.25 Å) is shown as a dashed black line. The electron spin density on the monophenol substrate is reflected on the greyscale shading in the projection of the 2D scans.

with their 2D PESs shown in Figures 3B and S5). From these 2D PESs, we obtained the calculated energies for the key reaction intermediates and TS barriers along the monooxygenation reaction coordinates of different monophenols (Figure 3A). These computational reaction coordinates show that 2O, TS2, and 3O become increasingly stabilized with more EDGs, while TS1 remains mostly unaffected. The different dependencies of TS1 and TS2 on the substrate *para*-group predict a change in the rate-limiting step as the monophenol substrate changes from having more EWGs (TS2 is rate-limiting) to having more EDGs (TS1 is rate-limiting). This computationally predicted trend is consistent with our experimental results for the biphasic Hammett plot (Figure 2C).

An inspection of the calculated 2D PES plots shows that, even though the TS1 energies are similar for different substrates (Figure 3A), the H-transfer and O−O cleavage reaction paths become increasingly more concerted for monophenols with EDGs (see the trend for 1P → 2O (solid black lines) from 4-COOCH$_3$ to 4-OCH$_3$ in Figure 3B). In fact, for the monophenol with the most EDG, 4-methoxyphenol (4-OCH$_3$, Figure 3B), attempts to optimize its bis-μ-oxo dicopper(III) intermediate (1O) upon peroxide O−O cleavage from the ternary intermediate (1P), result in spontaneous H-transfer from the substrate to form 2O (*i.e.*, no stable 1O intermediate in Figure 3B). To evaluate whether a more concerted reaction path would reproduce our experimental results (and, in particular, the large primary SKIE values for EDGs in Figure 2C), structures from the PES corresponding to the TS for the fully concerted O−O cleavage and H-transfer reaction were examined (labeled TS1c in Figure 3B). These structures were subjected to a constrained search to obtain approximations of the TS for the fully concerted path with respect to H-transfer and O−O cleavage (dashed lines in Figure 3B). These concerted TS1c exhibited the following: (i) weak energy stabilization with more EDGs (by 1.1 kcal/mol over the EDG range), (ii) predominant proton transfer with only 20−40% concomitant electron transfer (Table S4), (iii) large predicted SKIE values (>5.0, Table S3), and (iv) free energies in reasonable agreement with their respective experimental barriers from k_2 (see Table S2 and Figure S8 for ΔE and ΔG for different functionals). This concerted description of the O−O cleavage and H-transfer step is fully consistent with our experimental results for EDGs (see the

Hammett plot and substrate dependence of SKIE in Figure 2C), and in fact, their large SKIE values are consistent with a more synchronous PCET process.[31] This analysis reveals that, although our computational approach reproduces the general trend of energy barriers with increasing EDGs, it appears to underestimate the concertedness at TS1, which more broadly underscores the importance for the experimental evaluation of computational reaction coordinate predictions.

The results of this study provide direct evidence of a H-transfer step from the monophenol to the μ-η^2:η^2-peroxide of oxy-Ty. In fact, the monooxygenation rates of monophenols with EDGs are strongly dependent on the phenolic proton isotope (SKIE values >5) but are only weakly dependent on the electron-donating ability of the *para*-group (σ_p^+). Consistently, their TS1c barriers correlate linearly with their corresponding O−H bond dissociation free energies ($R^2 = 1.0$, Figure S3).[32] Importantly, this newly established H-transfer step initiates a monooxygenation mechanism (Figure 1, right) that is fundamentally different from previous proposals, which invoke coordination of a deprotonated monophenolate substrate to a Cu(II) or Cu(III) site (Figure 1, left).[5,24]

Unlike Ty, the reactions of the μ-η^2:η^2-peroxide dicopper(II) and bis-μ-oxo dicopper(III) model complexes with monophenols do not lead to productive monooxygenation; instead, they lead to the generation of phenoxyl radicals that C−C couple due to the absence of the protein pocket substrate cage effect on the phenoxyl radical.[5] Despite the difference in the reaction outcome, phenolic H-transfer to the Cu$_2$O$_2$ site is observed in both Ty (from this study) and these model complexes.[33] However, the former is described as varying from PCET to HAT with increasing EDGs (Figure 3B), while the latter is described as a sequential electron-transfer/proton-transfer (ETPT) process. In addition to the differences in the solvation and [Cu$_2$O$_2$]$^{2+}$ one-electron reduction potentials between Ty and these model complexes,[33] their mechanistic difference in H-transfer likely reflects the different interactions between the monophenol substrate and their Cu$_2$O$_2$ sites. Indeed, in Ty the monophenol substrate forms a well-defined ternary intermediate with a specific H-bond between the monophenol and the μ-η^2:η^2-peroxide (Figure 1, right), offering a favorable path for H-transfer,[12] while the model complexes follow a bimolecular reaction with monophenols that lacks any preorganized interaction for facile H-transfer.

In summary, this study (i) shows that the rate-limiting TS of monophenol monooxygenation in Ty is tuned by the substrate *para*-group (TS1 for EDGs versus TS2 for EWGs; see Figure 3A) and (ii) provides direct experimental evidence and a detailed mechanistic description of the phenolic H-transfer to the peroxide of the μ-η^2:η^2-Cu(II)$_2$(O$_2^{2-}$) site of oxy-Ty. Together with our previous study on the subsequent aromatic hydroxylation step,[12] our results define a complete mechanistic framework for the monophenol monooxygenation reactivity of oxy-Ty, which is fundamentally different from previous proposals and revises our understanding of O$_2$ activation and reactivity in biological CBC sites.[1,5,19] These new mechanistic insights into the monooxygenation reaction of oxy-Ty provide the basis for understanding the elusive structure−function correlations between the different families of CBC enzymes,[16,17,26] as well as for engineering CBC active sites in *de novo* enzymes[2] and homogeneous and heterogeneous catalysts.[3,4,33,34]

ASSOCIATED CONTENT

Supporting Information

The Supporting Information is available free of charge at https://pubs.acs.org/doi/10.1021/jacs.3c07450.

Experimental and computational methods, supporting data and figures, and a description of Data set 1 (PDF)

Data set 1: contains all QM/MM-optimized structures (ZIP)

AUTHOR INFORMATION

Corresponding Authors

Lubomír Rulíšek − *Institute of Organic Chemistry and Biochemistry of the Czech Academy of Sciences, 166 10 Praha 6, Czech Republic*; Email: lubomir.rulisek@uochb.cas.cz

Edward I. Solomon − *Department of Chemistry, Stanford University, Stanford, California 94305, United States; Stanford Synchrotron Radiation Lightsource, SLAC National Accelerator Laboratory, Stanford University, Menlo Park, California 94025, United States;* orcid.org/0000-0003-0291-3199; Email: Edward.Solomon@stanford.edu

Authors

Ioannis Kipouros − *Department of Chemistry, Stanford University, Stanford, California 94305, United States*

Agnieszka Stańczak − *Institute of Organic Chemistry and Biochemistry of the Czech Academy of Sciences, 166 10 Praha 6, Czech Republic; Faculty of Science, Charles University, 128 00 Praha 2, Czech Republic*

Eleanor M. Dunietz − *Department of Chemistry, Stanford University, Stanford, California 94305, United States*

Jake W. Ginsbach − *Department of Chemistry, Stanford University, Stanford, California 94305, United States*

Martin Srnec − *J. Heyrovský Institute of Physical Chemistry, Czech Academy of Sciences, 182 23 Prague, Czech Republic*

Complete contact information is available at:
https://pubs.acs.org/10.1021/jacs.3c07450

Author Contributions

[#]I.K. and A.S. contributed equally.

Notes

The authors declare no competing financial interest.

ABBREVIATIONS

CBC, coupled binuclear copper; Ty, tyrosinase; EAS, electrophilic aromatic substitution; ET, electron transfer; SKIE, solvent kinetic isotope effect; QM/MM, quantum mechanics/molecular mechanics; EWG, electron-withdrawing group; EDG, electron-donating group; HAT, H atom transfer; PCET, proton-coupled electron transfer; PES, potential energy surface; TS, transition state; ETPT, electron-transfer/proton-transfer

REFERENCES

(1) Solomon, E. I.; Heppner, D. E.; Johnston, E. M.; Ginsbach, J. W.; Cirera, J.; Qayyum, M.; Kieber-Emmons, M. T.; Kjaergaard, C. H.; Hadt, R. G.; Tian, L. Copper Active Sites in Biology. *Chem. Rev.* **2014**, *114* (7), 3659−3853.

(2) Pirro, F.; La Gatta, S.; Arrigoni, F.; Famulari, A.; Maglio, O.; Del Vecchio, P.; Chiesa, M.; De Gioia, L.; Bertini, L.; Chino, M.; Nastri, F.; Lombardi, A. A De Novo-Designed Type 3 Copper Protein Tunes Catechol Substrate Recognition and Reactivity. *Angew. Chem. Int. Ed* **2023**, *62* (1), No. e202211552.

(3) Snyder, B. E. R.; Bols, M. L.; Schoonheydt, R. A.; Sels, B. F.; Solomon, E. I. Iron and Copper Active Sites in Zeolites and Their Correlation to Metalloenzymes. *Chem. Rev.* **2018**, *118* (5), 2718−2768.

(4) Feng, X.; Song, Y.; Chen, J. S.; Xu, Z.; Dunn, S. J.; Lin, W. Rational Construction of an Artificial Binuclear Copper Monooxygenase in a Metal−Organic Framework. *J. Am. Chem. Soc.* **2021**, *143* (2), 1107−1118.

(5) Itoh, S.; Fukuzumi, S. Monooxygenase Activity of Type 3 Copper Proteins. *Acc. Chem. Res.* **2007**, *40* (7), 592−600.

(6) Matoba, Y.; Kumagai, T.; Yamamoto, A.; Yoshitsu, H.; Sugiyama, M. Crystallographic Evidence That the Dinuclear Copper Center of Tyrosinase Is Flexible during Catalysis. *J. Biol. Chem.* **2006**, *281* (13), 8981−8990.

(7) Eickman, N. C.; Solomon, E. I.; Larrabee, J. A.; Spiro, T. G.; Lerch, K. Ultraviolet Resonance Raman Study of Oxytyrosinase. *Comparison with Oxyhemocyanins* **1978**, *100* (20), 6529−6531.

(8) Kipouros, I.; Stańczak, A.; Culka, M.; Andris, E.; Machonkin, T. R.; Rulíšek, L.; Solomon, E. I. Evidence for H-Bonding Interactions to the μ-η^2:η^2-Peroxide of Oxy-Tyrosinase That Activate Its Coupled Binuclear Copper Site. *Chem. Commun.* **2022**, *58* (24), 3913−3916.

(9) Himmelwright, R. S.; Eickman, N. C.; LuBien, C. D.; Solomon, E. I.; Lerch, K. Chemical and Spectroscopic Studies of the Binuclear Copper Active Site of Neurospora Tyrosinase: Comparison to Hemocyanins. *J. Am. Chem. Soc.* **1980**, *102* (24), 7339−7344.

(10) Ross, P. K.; Solomon, E. I. An Electronic Structural Comparison of Copper-Peroxide Complexes of Relevance to Hemocyanin and Tyrosinase Active Sites. *J. Am. Chem. Soc.* **1991**, *113* (9), 3246−3259.

(11) Yamazaki, S.; Itoh, S. Kinetic Evaluation of Phenolase Activity of Tyrosinase Using Simplified Catalytic Reaction System. *J. Am. Chem. Soc.* **2003**, *125* (43), 13034−13035.

(12) Kipouros, I.; Stańczak, A.; Ginsbach, J. W.; Andrikopoulos, P. C.; Rulíšek, L.; Solomon, E. I. Elucidation of the Tyrosinase/O$_2$/Monophenol Ternary Intermediate That Dictates the Monooxygenation Mechanism in Melanin Biosynthesis. *Proc. Natl. Acad. Sci. U.S.A.* **2022**, *119* (33), No. e2205619119.

(13) Matoba, Y.; Kihara, S.; Bando, N.; Yoshitsu, H.; Sakaguchi, M.; Kayama, K.; Yanagisawa, S.; Ogura, T.; Sugiyama, M. Catalytic

Mechanism of the Tyrosinase Reaction toward the Tyr98 Residue in the Caddie Protein. *PLoS Biol.* **2018**, *16* (12), No. e3000077.

(14) Siegbahn, P. E. M. The Catalytic Cycle of Tyrosinase: Peroxide Attack on the Phenolate Ring Followed by O-O Bond Cleavage. *J. Biol. Inorg. Chem.* **2003**, *8* (5), 567−576.

(15) Inoue, T.; Shiota, Y.; Yoshizawa, K. Quantum Chemical Approach to the Mechanism for the Biological Conversion of Tyrosine to Dopaquinone. *J. Am. Chem. Soc.* **2008**, *130* (50), 16890−16897.

(16) Kampatsikas, I.; Rompel, A. Similar but Still Different: Which Amino Acid Residues Are Responsible for Varying Activities in Type-III Copper Enzymes? *ChemBioChem.* **2021**, *22* (7), 1161−1175.

(17) Decker, H.; Solem, E.; Tuczek, F. Are Glutamate and Asparagine Necessary for Tyrosinase Activity of Type-3 Copper Proteins? *Inorg. Chim. Acta* **2018**, *481*, 32−37.

(18) Siegbahn, P. E. M.; Borowski, T. Comparison of QM-Only and QM/MM Models for the Mechanism of Tyrosinase. *Faraday Discuss.* **2011**, *148*, 109−117.

(19) Kipouros, I.; Solomon, E. I. New Mechanistic Insights into Coupled Binuclear Copper Monooxygenases from the Recent Elucidation of the Ternary Intermediate of Tyrosinase. *FEBS Lett.* **2023**, *597* (1), 65−78.

(20) Siegbahn, P. E. M.; Wirstam, M. Is the Bis-μ-Oxo Cu$_2$ (III,III) State an Intermediate in Tyrosinase? *J. Am. Chem. Soc.* **2001**, *123* (47), 11819−11820.

(21) Keown, W.; Gary, J. B.; Stack, T. D. P. High-Valent Copper in Biomimetic and Biological Oxidations. *J. Biol. Inorg. Chem.* **2017**, *22* (2−3), 289−305.

(22) Muñoz-Muñoz, J. L.; Berna, J.; García-Molina, M. d. M.; Garcia-Molina, F.; Garcia-Ruiz, P. A.; Varon, R.; Rodriguez-Lopez, J. N.; Garcia-Canovas, F. Hydroxylation of P-Substituted Phenols by Tyrosinase: Further Insight into the Mechanism of Tyrosinase Activity. *Biochem. Biophys. Res. Commun.* **2012**, *424* (2), 228−233.

(23) Company, A.; Palavicini, S.; Garcia-Bosch, I.; Mas-Ballesté, R.; Que, L.; Rybak-Akimova, E. V.; Casella, L.; Ribas, X.; Costas, M. Tyrosinase-Like Reactivity in a CuIII2(μ-O)2 Species. *Chem. Eur. J.* **2008**, *14* (12), 3535−3538.

(24) Mirica, L. M.; Vance, M.; Rudd, D. J.; Hedman, B.; Hodgson, K. O.; Solomon, E. I.; Stack, T. D. P. Tyrosinase Reactivity in a Model Complex: An Alternative Hydroxylation Mechanism. *Science* **2005**, *308* (5730), 1890−1892.

(25) Solem, E.; Tuczek, F.; Decker, H. Tyrosinase versus Catechol Oxidase: One Asparagine Makes the Difference. *Angew. Chem., Int. Ed.* **2016**, *55* (8), 2884−2888.

(26) Prexler, S. M.; Frassek, M.; Moerschbacher, B. M.; Dirks-Hofmeister, M. E. Catechol Oxidase versus Tyrosinase Classification Revisited by Site-Directed Mutagenesis Studies. *Angew. Chem., Int. Ed.* **2019**, *58* (26), 8757−8761.

(27) Fujieda, N.; Umakoshi, K.; Ochi, Y.; Nishikawa, Y.; Yanagisawa, S.; Kubo, M.; Kurisu, G.; Itoh, S. Copper−Oxygen Dynamics in the Tyrosinase Mechanism. *Angew. Chem., Int. Ed.* **2020**, *59* (32), 13385−13390.

(28) Goldfeder, M.; Kanteev, M.; Isaschar-Ovdat, S.; Adir, N.; Fishman, A. Determination of Tyrosinase Substrate-Binding Modes Reveals Mechanistic Differences between Type-3 Copper Proteins. *Nat. Commun.* **2014**, *5* (1), 4505.

(29) Kampatsikas, I.; Pretzler, M.; Rompel, A. Identification of Amino Acid Residues Responsible for C−H Activation in Type-III Copper Enzymes by Generating Tyrosinase Activity in a Catechol Oxidase. *Angew. Chem., Int. Ed.* **2020**, *59* (47), 20940−20945.

(30) Hansch, C.; Leo, A.; Taft, R. W. A Survey of Hammett Substituent Constants and Resonance and Field Parameters. *Chem. Rev.* **1991**, *91* (2), 165−195.

(31) Maldonado-Domínguez, M.; Bím, D.; Fučík, R.; Čurík, R.; Srnec, M. Reactive Mode Composition Factor Analysis of Transition States: The Case of Coupled Electron−Proton Transfers. *Phys. Chem. Chem. Phys.* **2019**, *21* (45), 24912−24918.

(32) Warren, J. J.; Tronic, T. A.; Mayer, J. M. Thermochemistry of Proton-Coupled Electron Transfer Reagents and Its Implications. *Chem. Rev.* **2010**, *110* (12), 6961−7001.

(33) Osako, T.; Ohkubo, K.; Taki, M.; Tachi, Y.; Fukuzumi, S.; Itoh, S. Oxidation Mechanism of Phenols by Dicopper-Dioxygen (Cu2/O2) Complexes. *J. Am. Chem. Soc.* **2003**, *125*, 11027−11033.

(34) Hoffmann, A.; Citek, C.; Binder, S.; Goos, A.; Rübhausen, M.; Troeppner, O.; Ivanović-Burmazović, I.; Wasinger, E. C.; Stack, T. D. P.; Herres-Pawlis, S. Catalytic Phenol Hydroxylation with Dioxygen: Extension of the Tyrosinase Mechanism beyond the Protein Matrix. *Angew. Chem., Int. Ed.* **2013**, *52* (20), 5398−5401.